Dissertation

submitted to the

Combined Faculty of Mathematics, Engineering and Natural Sciences

of Heidelberg University, Germany

for the degree of

Doctor of Natural Sciences

Put forward by

M.Sc. Hannes Lindenblatt

born in Kassel

Oral examination: November 8th, 2023

Energy and Charge Transfer in Dimers and Trimers of Xenon

Abstract

The goal of this thesis is the investigation of decay processes in innershell ionised xenon dimers and trimers. To this end, the small clusters were ionised using $100\,\text{eV}$ photons from a Free-Electron Laser and the momenta of the created ion fragments and electrons were measured using the Reaction Microscope at FLASH2. Employing an XUV/XUV pump-probe scheme, the timescale to distribute energy or charge throughout the cluster following local excitation was determined to below $(186\pm6)\,\text{fs}$ for dimers decaying into Xe^{1+} / Xe^{2+} and $(84\pm13)\,\text{fs}$ for trimers decaying into Xe^{1+} / Xe^{1+} / Xe^{1+}. The kinetic energy distributions yield clear evidence that Xe_2^{2+} decays by a slow CT process after bond contraction and Xe_3^{2+*} decays by ETMD(3) before the nuclei can move. Furthermore, we see signatures of frustrated ionisation in Xe_2 dimers.

Zusammenfassung

Das Ziel dieser Dissertation ist die Untersuchung von Zerfallsprozessen von Xenon Dimeren und Trimeren, die in der 4d Schale ionisiert wurden. Dazu wurden kleine Cluster mit Hilfe von $100\,\text{eV}$ Photonen eines Freie-Elektronen-Lasers ionisiert und die Impulse der entstehenden Ionen und Elektronen mit dem Reaktionsmikroskop an FLASH2 gemessen. Durch die Anwendung eines Pump-Probe Messverfahrens konnte die Zeitkonstante für die Verteilung von Ladung beziehungsweise Energie im Cluster nach der anfänglichen lokalen Anregung bestimmt werden. Die Rate wurde mit einer oberen Grenzen von $(186\pm6)\,\text{fs}$ für Dimere, welche in Xe^{1+} / Xe^{2+} zerfallen, und $(84\pm13)\,\text{fs}$ für Trimere, welche in Xe^{1+} / Xe^{1+} / Xe^{1+} zerfallen, bestimmt. Die Verteilung der kinetischen Energie der Ionen weist eindeutige Kennzeichen dafür auf, dass Xe_2^{2+}-Dimere über einen langsamen Ladungstransfer zerfallen, nachdem sich ihre Bindung zusammengezogen hat. Für Trimere deutet die Verteilung der kinetischen Energie darauf hin, dass ein durch Elektronentransfer induzierter korrelierter Zerfall (ETMD(3)) stattfindet, bevor sich die Atomkerne bewegen können. Des Weiteren ist die Signatur von frustrierter Ionisation in der Energieverteilung der zerfallenen Xe_2 Dimeren zu sehen.
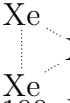
Contents

Chapter 1

Introduction

The transfer of energy by electromagnetic radiation and charge transfer by electrons between atoms or molecules are fundamental processes in the dynamics of light and matter. When either of them carry kinetic energy of more than roughly $10\,\mathrm{eV}$, they enter the region of ionising radiation, where most elements or molecules can be ionised. Chemical reactions on this energy scale start to happen rapidly on the timescale of few hundreds of femtoseconds. Especially once several positive charge centres are formed within molecules, the Coulomb repulsion leads to dissociation of the molecules. Radiation of even higher energy has become a standard tool to investigate molecular structures by X-ray or electron diffraction. This has been done for a long time with photons from synchrotron radiation [1, 2] or electrons in cryo-electron microscopy [3, 4]. Both methods rely on sophisticated averaging over a large ensemble in order to come close to atomic resolution on the angstrom level. With the advent of Free Electron Lasers (FELs), light sources of such high brilliance became available that enough photons can be in a short pulse on the order of $10\,\mathrm{fs}$ to $100\,\mathrm{fs}$ to produce a diffraction image of single nano-structures [5–7]. With that possibility, it becomes feasible to observe dynamics of those particles in a pump-probe scheme. First some reaction is triggered, e.g. by non-ionising ultraviolet radiation, and after a given time delay, the evolved state is imaged by the FEL pulse. However this relies on the assumption that the induced destruction of the particles by the high intensity of ionising radiation is slower than the pulse duration. Otherwise one would obtain an averaged image over the fragmentation process. This is known as the diffraction before destruction method. In order to judge whether the fragmentation processes are slow compared

to the imaging pulse duration in a large complex molecule, it is necessary to perform Molecular Dynamics simulations (MDs) [8]. Those simulations in turn require detailed knowledge of the fundamental interaction processes between atoms in the molecules. Although many studies have investigated the resulting reaction products of these processes, such as electrons emitted from Auger-Meitner Decay (AMD)[9, 10], Interatomic Coulombic Decay (ICD)[11, 12] or photons from Radiative Charge Transfer (RCT)[13, 14], it is often not clear what the reaction rate is as a function of real time and the spatial coordinates in a molecule.

To investigate these dynamics, we performed an experiment on small clusters of xenon at the FLASH2 reaction microscope (FlashRemi). As the atoms in a xenon cluster are heavy and only loosely bound by the weak Van der Waals interaction, we gain access to a regime where movement of the nuclei is comparably slow. Also, the clusters are at a large internuclear distance of approximately $4.4\,\text{Å}$, so the transfer processes are more easily accessible than in tightly bound molecules. The rate of these relaxation processes increases linearly with the number of neighbouring atoms and can eventually become more important than the direct interaction with the closest neighbour in large molecules or molecules in solution.

The experiment is done on a Xe Supersonic Gas Jet (SGJ) target that contains mainly Xe monomers, but also roughly $0.25\,\%$ of Xe⸱⸱⸱Xe dimers and $6.5\,\text{ppm}$ of Xe⸱⸱⸱Xe⸱⸱⸱Xe trimers. The Xe was ionized by FEL radiation at a photon energy of $100\,\text{eV}$. In this region, Xe is dominantly ionised by removal of a 4d inner-valence electron. This vacancy is localized at one of the Xe atoms and we can observe the desired transfer processes in the dimers and trimers. Using the REeaction MIcroscope (REMI), we measure fragments from the same original system in coincidence. This is done by obtaining the particles' momenta and applying momentum sum conditions[15].

That allows to attribute measured particles to a reaction from a common starting point by coincidence spectroscopy. Employing the technique of pump-probe Coulomb Explosion Imaging (CEI) [16], we can infer information on the inter nuclear distances in a time-resolved way. For the system of Xe⸱⸱⸱Xe dimers, a recent theoretical study from Liu, Kolorenč and Gokhberg [17] predicted that the 4d vacancy decays almost exclusively by AMD to different states of Xe⸱⸱⸱Xe^{2+*} that are initially still bound. However, it was not calculated how the system further relaxes from there. This gives us the starting point of our research question: What

2

is happening now afterwards? The experimental data shows that reaction channels of total charge state +3 are significantly enhanced in dimers. The ratio of events with a charge of +2 relative to events with a charge of +3 changes from $1:2$ in monomers to $2:1$ in dimers. This suggests that we should expect efficient non-local auto-ionising processes in the Xe dimers.

During this thesis project, several experimental and analysis methods were further developed. This begins with improved calibration of the spatial focus overlap that were crucial for the feasibility of XUV-XUV pump-probe measurements. Further, the analysis of REMI data was improved in order to cope with the large set of combinations between Xe isotopes and charge states. Additionally, several Monte Carlo simulations were performed in order to validate the analysis and interpretation of the measured data at hand.

From the Xe experiment we found signatures of slow Charge Transfer (CT) from $Xe^{...}Xe^{2+}$ dimers to the Xe^{1+} / Xe^{1+} channel. The Xe^{1+} / Xe^{2+} channel was observed after a time of less than $(186 \pm 6)\,\text{fs}$ and in trimers, the relaxation to Xe^{1+} / Xe^{1+} / Xe^{1+} was found to appear even faster, on a time scale of $(84 \pm 13)\,\text{fs}$. Additionally, we find that the trimers share the kinetic energy between Xe^{1+} / Xe^{1+} / Xe^{1+} equally. This a decay by means of a correlated three particle Electron Transfer Mediated Decay (ETMD(3)) process. In Xe_2 dimers we observed the phenomenon of frustrated ionisation. Its signature is that the nuclei are measured with kinetic energies that one would expect only from higher charge states than they were detected.

Structure of the Thesis   This thesis begins with an overview of the variety of electronic decay phenomena and what to expect to happen after the 4d photoionisation of Xe in Chapter 2. Chapter 3 describes experimental methods in Section 3.1, methods of data analysis in Section 3.2 and simulation methods in Section 3.3. Chapter 4 shows the experimental setup of the FlashRemi together with estimates on the experimental parameters such as target density and peak intensity on the target. Chapter 5 presents the results that were obtained by the measurements for the fragmentation of Xe dimers and trimers. Chapter 6 concludes this work with a summary.

Chapter 2

Electronic Decay and Transfer Processes in small Clusters

This Chapter provides an overview over the processes that we expect after local electronic excitation in small clusters. Jahnke et al. [18] review the large variety of these processes together with different theoretical and experimental approaches of studying them. Figure 2.0.1 provides us with an overview of the mechanisms in a Venn diagram. We find as two top level categories the local and the non-local processes and each of the two splits again into processes that lead to electron emission or not.

    The following sections will briefly illustrate these processes, as they are described by Jahnke et al., but in the frame of Xe, Xe dimers and trimers and the 4d inner-valence ionisation. Section 2.1 shows the localized AMD and Radiative Decay (RD). Section 2.2 compares the non-ionising transfer processes CT, RCT, and Förster Resonant Energy Transfer (FRET). Section 2.3 deals with the non-local auto-ionising processes ICD, double Interatomic Coulombic Decay (dICD), collective Interatomic Coulombic Decay (cICD) (listed in Figure 2.0.1 as 3e-ICD), two particle Electron Transfer Mediated Decay (ETMD(2)), and ETMD(3) as well as the non-local double ionisation through the Knock Off ionisation (KO).

    Depending on the electronic state of the excited ion, not all of the processes are energetically allowed. In a dimer or larger clusters there is additionally the phenomenon of a Coulomb blockade. Section 2.4 gives an overview over the states in Xe—Xe dimers and consider which of the introduced processes are possible.
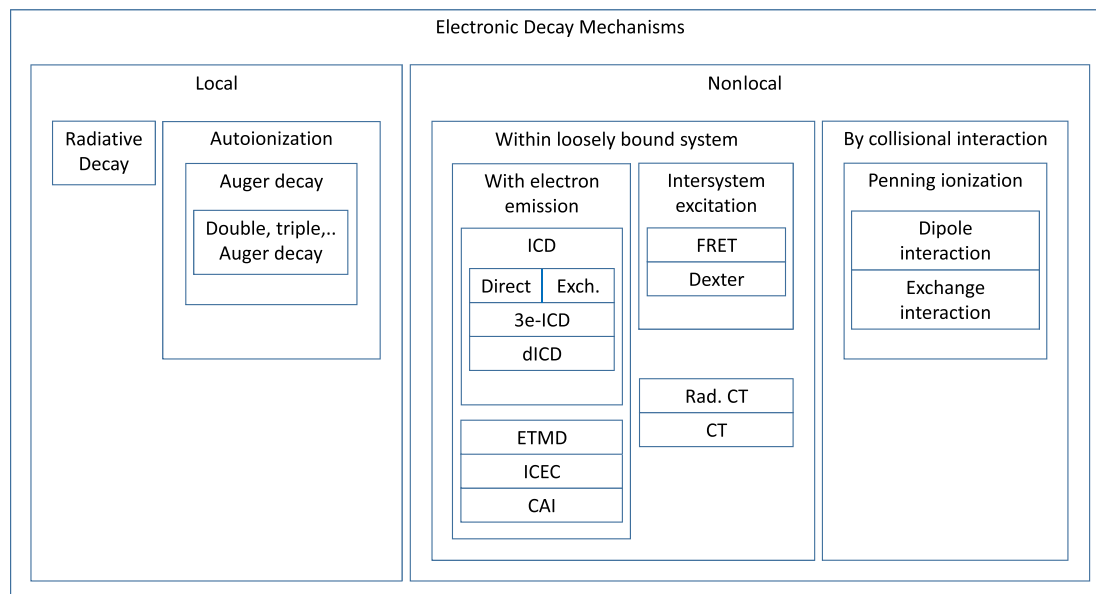
Figure 2.0.1: Figure 3 from Jahnke et al. [18] without change, licensed under ACS AuthorChoice license.

2.1 Local Decay Processes

Independent of the environment of an atom, there are two processes for the relaxation from an electronically excited state, RD and AMD. Figure 2.1.1 shows the RD process after ionization of the 4d electron. One of the 5p electrons fills the 4d hole and emits a photon by spontaneous emission. The photon therefore has a characteristic energy and the process can be observed by fluorescence spectroscopy. The photon energies are determined by the specific states involved in the transition and can serve as a fingerprint. The other mechanism is AMD, see Figure 2.1.2. Here, the photon is not emitted as a real photon, but transfers energy directly to another electron in the ion. This leads to further ionization and we end up with doubly ionized Xe^{2+}. In Xe^{1+} with a 4d hole, there is also the possibility of double AMD, where the virtual photon ionizes two further electrons and the ion turns into Xe^{3+}. In systems with larger excitation, e.g. Xe^{1+} with a 1s core-level hole, the AMD process can repeat several times in a cascade of auto-ionising decays. Similar to RD, the emitted electrons from single AMD have well-defined kinetic energies. Their energy is given by the difference of the energy gain through relaxation and the ionization potential. The energy gain is again specific to the inner-valence hole state and the final electron configuration of the ion. When
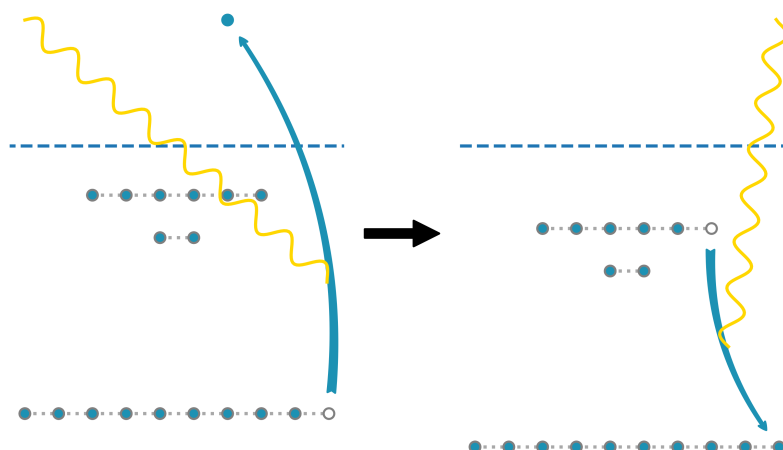
Figure 2.1.1: Sketch of the Radiative Decay (RD) process after 4d inner-valence ionisation.

The vertical dimension corresponds to the potential energy of the electrons, where the blue dashed line denotes the ionisation threshold. Filled blue circles denote electrons, empty grey circles show holes in an orbital. The grey dotted lines mark the principal energy levels, from bottom to top: 4d, 5s and 5p. In ionic systems, the energy levels are shifted to lower potentials. The thick blue arrows illustrate the transition of electrons, and yellow, wiggly lines indicate photons. Photons above the blue dashes lines are coming from the top left into the system and leaving the system to the top right. Photons between electron transition arrows are virtual photons, that are exchanged between those electrons.

Figure 2.1.2: Sketch of single Auger-Meitner Decay (AMD) after 4d inner-valence ionization. For explanation of the illustration see Figure 2.1.1.

double AMD happens the sum of the two kinetic energies is well-defined instead. The two electrons share a constant amount of energy. That usually means, they will both have much lower energies than the electrons from single AMD.
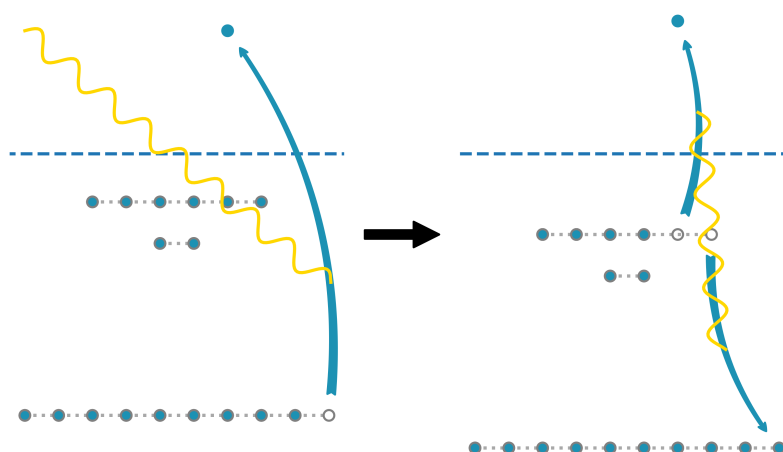
When both of these decay mechanisms are energetically allowed, both are in principle active. However, AMD is often much faster, in the order of femtoseconds, while RD takes nanoseconds to occur. Therefore AMD will happen in most cases whenever possible.

2.2 Transfer Processes

This Section shows transfer processs, where either electrons or photons are exchanged between two ions or atoms, but no electron leaves the system. In analogy to the RD process, a dimer can relax by RCT, see Figure 2.1.1. An electron from
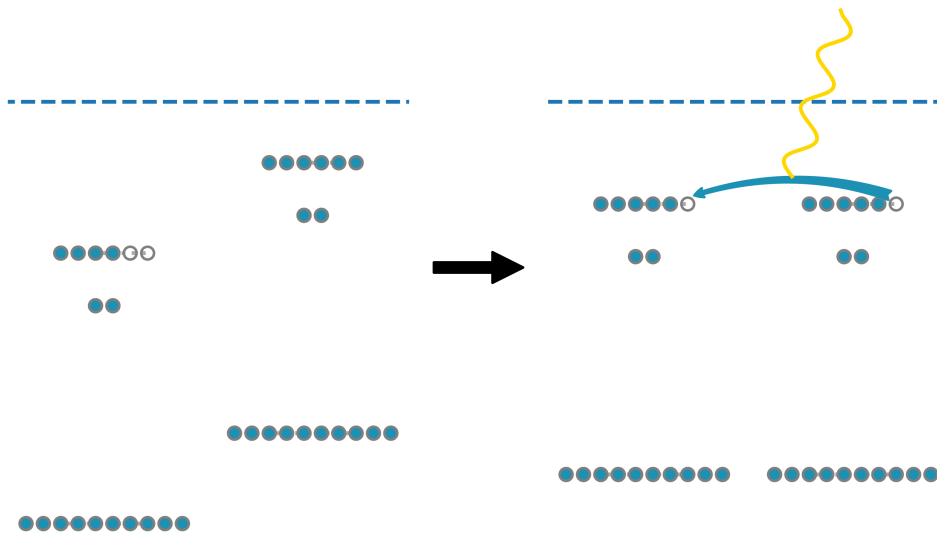
Figure 2.2.1: Sketch of Radiative Charge Transfer (RCT) between a Xe^{2+} ion and neutral Xe. For explanation of the illustration see Figure 2.1.1.

a neutral atom fills the hole in the neighbouring ion and emits the excess energy in form of a real photon. As with RD, this is a very slow process. Therefore it will only occur when all other processes are suppressed. After the transfer, both parts are charged and the dimer dissociates rapidly in a Coulomb Explosion (CE). Figure 2.2.2 shows the CT process without emission of a photon. This can be
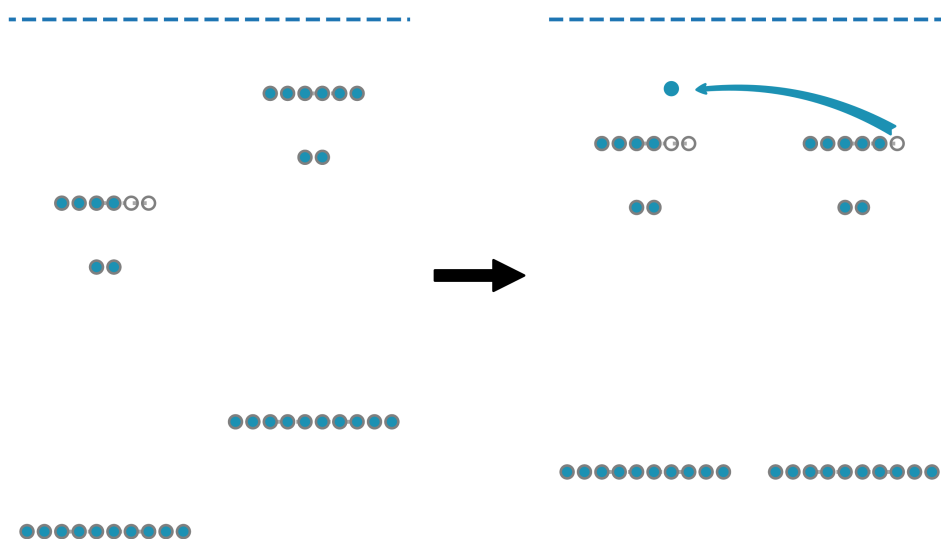
Figure 2.2.2: Sketch of Charge Transfer (CT) between a Xe^{2+} ion and neutral Xe. No photon is emitted, instead the system is still in an excited state. For explanation of the illustration see Figure 2.1.1.

much faster than RCT, but it requires, that there is an another excited state available, that matches in the overall potential energy of the previous state at the current inter nuclear distance. Finally the dimer dissociates since both atom sites carry now a positive charge. However one of the ions will be in an excited state until it relaxes by RD. In both of the CT and RCT process, the transfer rate will be proportional to the orbital overlap between the states before and after transfer of the electron. This means, it will be only possible as long as the dimer stays bound or the inter-nuclear distance did not yet increase too much during a fragmentation.

The FRET process exchanges instead a virtual photon between two atoms or ions, see Figure 2.2.3. The photon transfers the energy in an local excitation to the other ion and excites it. This only happens when there is an matching resonance in the other atom or ion. In the case of Xe^{1+} / Xe^{1+}, this does not seem important. However in larger systems, this resonant transfer will increase the rate of radiation transport to beyond the first neighbour.

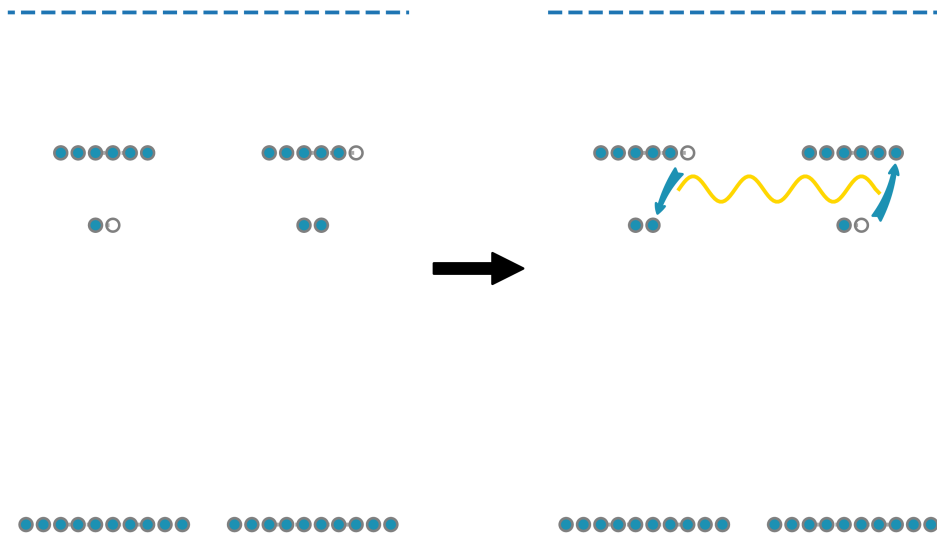Figure 2.2.3: Sketch of Förster Resonant Energy Transfer (FRET) between two Xe^{1+} ions. The local excitation is transferred to the other ion through a virtual photon. For explanation of the illustration see Figure 2.1.1.

2.3 Nonlocal Autoionisation Processes

After the initial photoionisation and the following AMD, the ion can still remain in an excited state and has the potential to ionise atoms in the environment. Figure 2.3.1 shows the prototypical process of ICD. An electron fills the hole in an lower orbital and the emitted virtual photon ionizes a close by neutral Xe. The decay rate is slower than local AMD, but still much faster than RD. All of the following process are more specific variants of ICD. Figure 2.3.2 shows the dICD process. This requires a transition with high energy, such as a 5p to 4d transition. The resulting virtual photon has more energy than is needed for double ionisation of the Xe and turns it into Xe^{2+}. In the other direction, the cICD uses two excitations that contribute simultaneously to a two-photon ionisation, see Figure 2.3.3. The process of exchange Interatomic Coulombic Decay (exICD) is different in that way that now it is not a photon that is transmitted between atoms, but an electron. In a way, this is like a combination of RCT and ICD, see Figure 2.3.4. It is noteworthy that the final charge state of the ions and the kinetic energy of the emitted electron will be exactly the same as after the usual ICD, but the decay rate is now determined by the orbital overlap of the initial
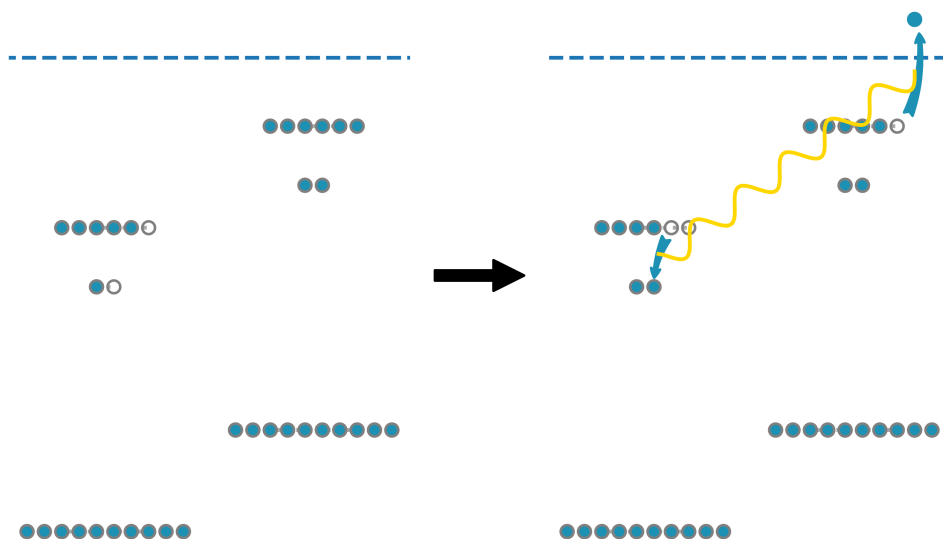
Figure 2.3.1: Sketch of Interatomic Coulombic Decay (ICD) in a $\mathrm{Xe}\cdots\mathrm{Xe}^{2+*}$ dimer ion. The excited ion emits a virtual photon, which ionises the neutral. For explanation of the illustration see Figure 2.1.1.
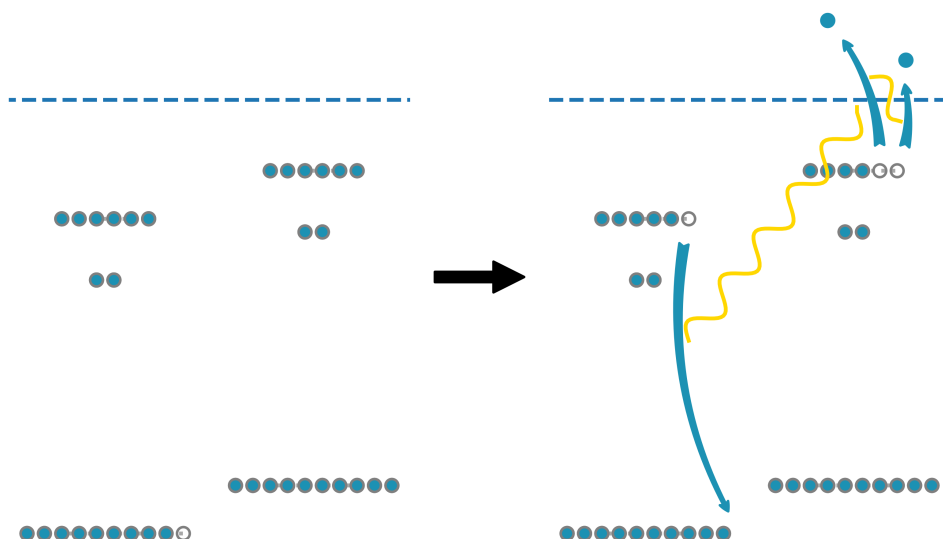
Figure 2.3.2: Sketch of double Interatomic Coulombic Decay (dICD) in a $\mathrm{Xe}\cdots\mathrm{Xe}^{2+*}$ dimer ion. The excited ion emits a high energetic virtual photon, which doubly ionises the neutral. For explanation of the illustration see Figure 2.1.1.
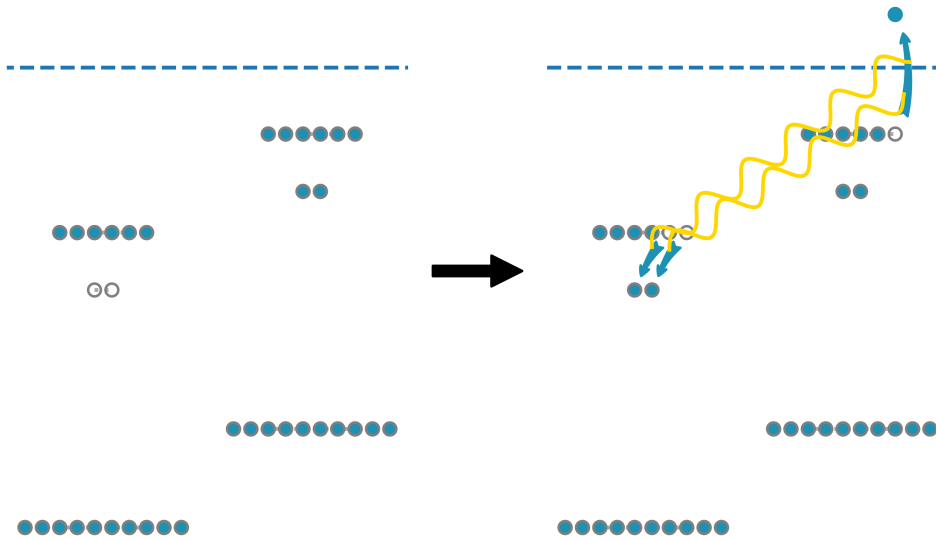
Figure 2.3.3: Sketch of collective Interatomic Coulombic Decay (cICD) in a doubly excited Xe⋯Xe^{2+*} dimer ion. Both electrons fill the two holes and emit virtual photons. The photons ionize the neutral Xe together. For explanation of the illustration see Figure 2.1.1.
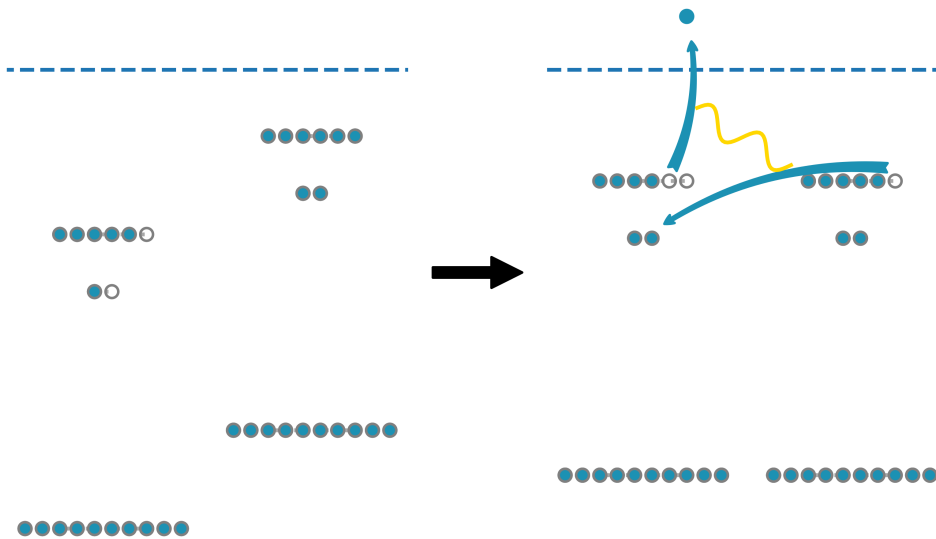
Figure 2.3.4: Sketch of exchange Interatomic Coulombic Decay (exICD) in a Xe⋯Xe^{2+*} dimer ion. An electron from the neutral Xe fills the hole and emits a virtual photon. The photon ionizes the ion again to Xe^{2+}. For explanation of the illustration see Figure 2.1.1.

and final state of the transferred electron. Very similar to exICD is the ETMD(2) process, see Figure 2.3.5. The difference is only that not the electron accepting
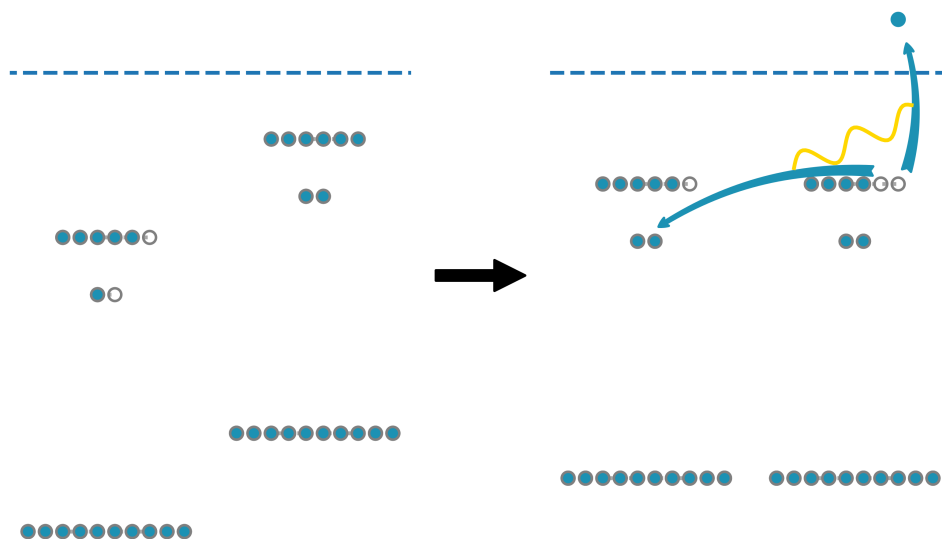
Figure 2.3.5: Sketch of two particle Electron Transfer Mediated Decay (ETMD(2)) in a $Xe \cdots Xe^{2+*}$ dimer ion. An electron from the neutral Xe fills the hole and emits a virtual photon. The photon further ionises the originally neutral Xe to Xe^{2+}. For explanation of the illustration see Figure 2.1.1.

Xe^{n+} is ionized, but the donating Xe. In trimers, this concept is followed one step further, see Figure 2.3.6. Now, it is neither the accepting, nor the donating Xe, that is ionized, but a third, observing Xe. In this constellation the rate of decay will not only depend on the orbital overlap as for exICD and ETMD(2), but also on the distance of the third particle to the other two.

As the 4d photoelectron has an energy above the ionisation threshold of Xe, it can directly ionise the other Xe atom if it is emitted in the right direction. Figure 2.3.7 shows the process, which is known as Knock Off ionisation (KO)[19]. This first ion is still excited with a 4d hole and will later decay, most likely by AMD. The sequence of KO and AMD brings the dimer very fast to the Xe^{1+} / Xe^{2+} state, as the energy transfer is immediately done by the photoelectron. Some of the possible electron energies from AMD can also have enough kinetic energy to ionize the neighbouring atom. This will be again a KO process, Figure 2.3.8 shows the sequence. This sequence is somewhat similar to the ETMD(2) process, but happens faster, as the photoelectron transfers with high kinetic energy in
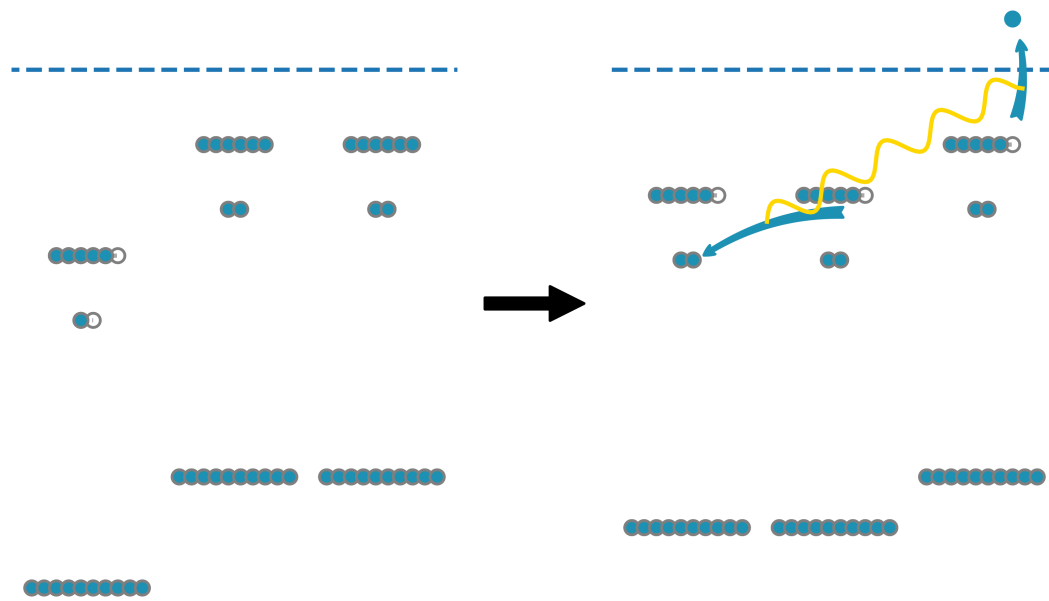
Figure 2.3.6: Sketch of three particle Electron Transfer Mediated Decay (ETMD(3)) in a Xe_3^{2+} trimer ion. An electron from one of the neutral Xe fills the 5s hole in the Xe^{2+} and emits a virtual photon. The photon ionises the other neutral Xe. For explanation of the illustration see Figure 2.1.1.
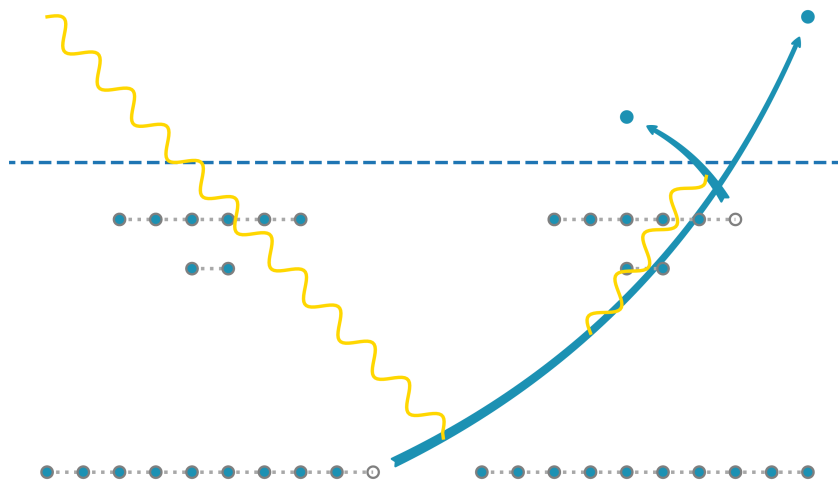
Figure 2.3.7: Sketch of Knock Off ionisation (KO) ionisation of a Xe_2 dimer. The photoelectron is emitted in the direction of the other Xe atom and ionises it by electron impact ionisation. For explanation of the illustration see Figure 2.1.1.

contrast to a slow CT electron from the neutral Xe to the ion. It is, however, only possible, when the AMD electron is emitted in the direction towards the neutral. These KO processes are minor contributions due to this restriction of
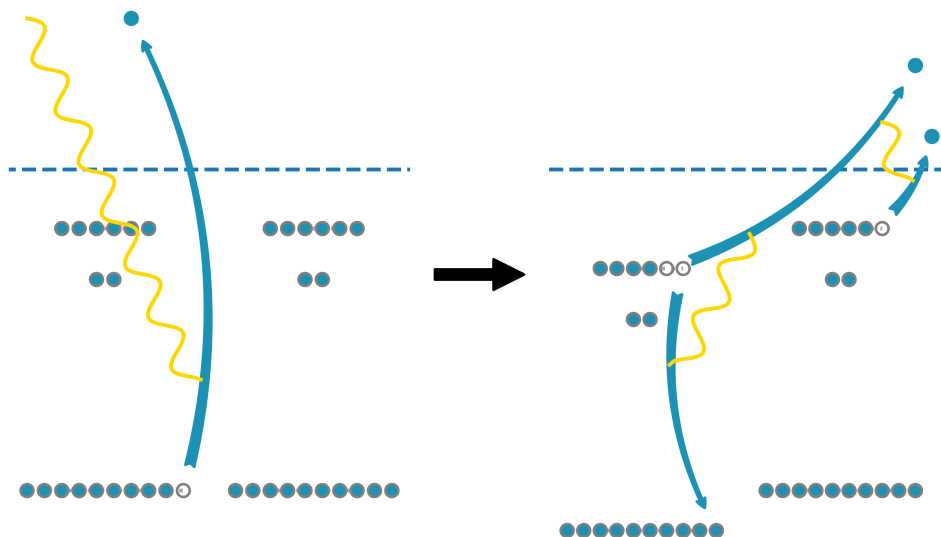
Figure 2.3.8: Sketch of KO ionisation after AMD of a Xe_2 dimer. The AMD electron is emitted in direction of the other Xe atom and ionises it by electron impact ionisation. For explanation of the illustration see Figure 2.1.1.

their electron emission angle, however it is not necessarily negligible. In dimers of D_2O and pyridine Mootheril Thomas estimated for the Sequential Ionisation (SI) from a single electron projectile that 16.6% of the double ionisation events are due to SI, the rest is attributed to ICD[20]. The SI process is very familiar with the KO process. In the former, the projectile electron does to impact ionisation, in the latter, the photoelectron essentially becomes the projectile electron for the next ionisation.

2.4 Potential Energy Curves and Coulomb Blocking

When there is an ion close to a neutral atom, the ionisation potential and the energy of excited states increase drastically as removing or exciting an electron in the neutral atom reduces the screening of the nuclear charges. That reduced screening increases the Coulomb potential and imposes an additional hill to climb. Interestingly, the lowest ionization threshold in Xe_2 is actually reduced, as the $Xe^{...}Xe^+$ ion is bound stronger than the neutral dimer. Only then, the ionisation of the neutral atom requires more energy than in the isolated atom case. Figure 2.4.1 shows in the left panel theoretically calculated potential energy curves from Liu, Kolorenč and Gokhberg [17] for $Xe^{...}Xe$, $Xe^{...}Xe^+$ with a 4d hole and the first excited states of $Xe^{...}Xe^{2+}$ with local charge or distributed charge in the dissociating Xe^{1+} / Xe^{1+} states. Liu, Kolorenč and Gokhberg estimated in their calculation, that at the inter nuclear distance, marked by the vertical dashed line, the rate of ICD is only about 0.2% of the single AMD rate. Additionally, the AMD rate is estimated on the order of a few femtoseconds. That means, AMD will happen before nuclear motion could bring the Xe closer together, where the ICD rate increases due to the shorter distance. The right panel of Figure 2.4.1 shows approximated potentials of the $Xe^{...}Xe$ ion using Lenard-Jones and Coulomb potentials. The displayed potentials use the Lennard-Jones parameters as shown later in Table 3.2. The excited states are then approximated by adding the excitation energy levels of atoms to the potential. This matches at long internuclear distance, but will underestimate the potential energy at low distances as we do not take into account that higher excited states have reduced screening of the nuclei charges. The $Xe^{...}Xe^{2+}$ $5p^{-2}$, $5s^{-1}5p^{-1}$ and $5s^{-2}$ states are shown in dark green, the $Xe^{...}Xe^+$ ground and 4d-hole states are shown in pink. The dissociating potentials of the Xe^{1+} / Xe^{1+} channels are shown in purple, here the ground state is shown as opaque line, all excited states of Xe^{1+} available in the NIST atomic spectra database [21] are shown as 90% transparent lines. Through the increased color intensity, we can identify areas, where many lines cluster together. Those level clusters are nearly degenerate in terms of their energy, but differ in the configuration of orbital momentum and spin. Additionally, we included potential curves for the triply ionised, dissociating states of Xe^{1+} / Xe^{2+}
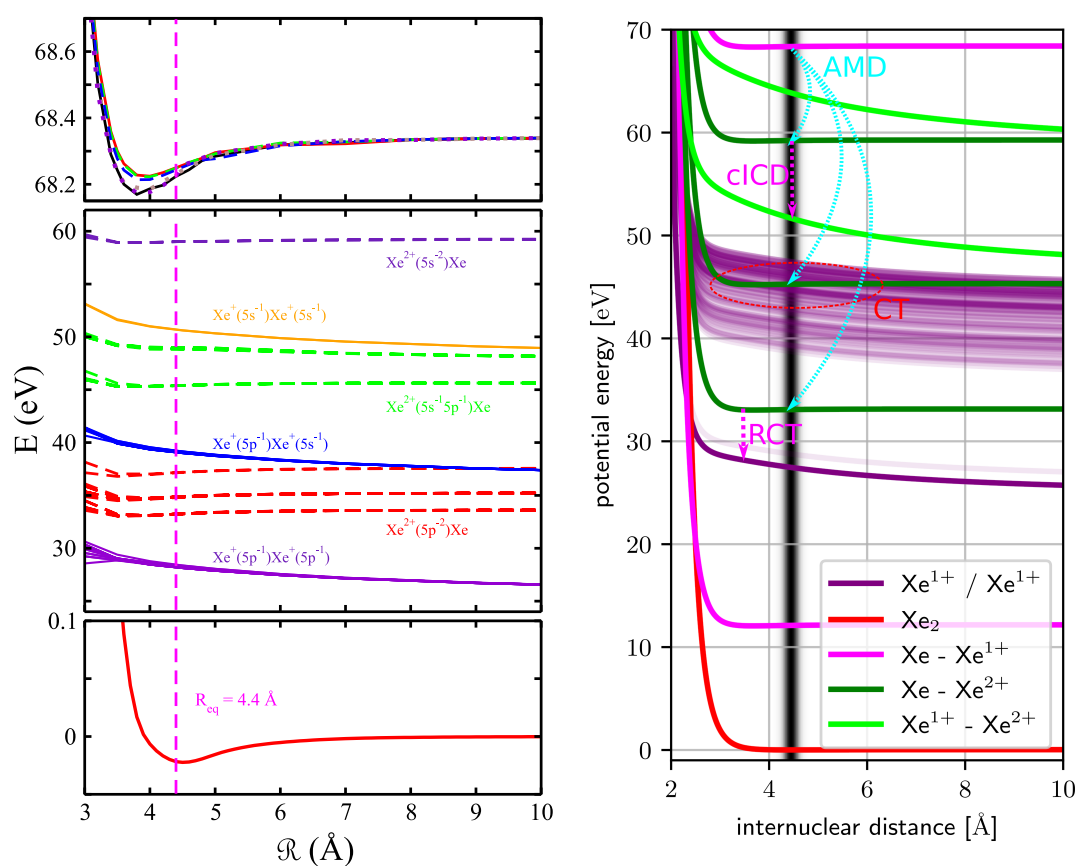
Figure 2.4.1: Left Panel: Theoretical calculation of Xe⋯Xe ion potential energy curves. Reprinted figure with permission from [[17] Liu, Kolorenč and Gokhberg, Physical Review A, 101(3), 033402, 2020] Copyright (2020) by the American Physical Society. Right Panel: Approximated potential energy curves by Lennard-Jones and Coulomb potentials. Further explanations in the main text.

as lime green curves. Between the Xe^{1+} / Xe^{2+} ground state and the highest Xe^{1+} / Xe^{1+} state in the figure there is an energy gap, which increases towards low distances. In reality, the excited Xe^{1+} / Xe^{1+} states converge towards the Xe^{1+} / Xe^{2+} ground state. However, as mentioned above, our approximation is over-simplified and can not show the convergence of the excited Xe^{1+} / Xe^{1+} states towards the Xe^{1+} / Xe^{2+} ground state as it always assumes the same Coulomb screening. The Frank-Condon region is marked by the density of the ground state as a grey-scaled area around $4.4\,\text{Å}$. Due to their positioning in between other potentials, the three different $Xe \cdots Xe^{2+}$ states can be expected to each do different follow-up decays. The lowest lying state $5p^{-2}$ is below the first electronically excited state of Xe^{1+} / Xe^{1+} and the electrons are locally at the Xe^{2+} already in the ground state. Therefore, it can only decay by RCT and we expect a lifetime of up to nanoseconds due to the radiative nature of the process. The second $5s^{-1}5p^{-1}$ state lies right in the middle of the band of excited states of Xe^{1+} / Xe^{1+}. From this we can expect the faster CT process, where the electron is transferred into one of the excited states and long after the dissociation will emit a photon. The doubly excited $5s^{-2}$ states are above the triply ionized Xe^{1+} / Xe^{2+} ground state. This offers the possibility of cICD to happen. Furthermore, as the ground state and the first excited state of Xe^{1+} / Xe^{2+} both lie below the 4d-hole state of $Xe \cdots Xe^{+*}$, it could possibly also decay by dICD or ETMD(2) into the triply ionised states. This possibility was not covered in Liu, Kolorenč and Gokhberg's work and we do not have an estimate on the likelihood for it compared to the AMD process.

Chapter 3

Methods

This Chapter presents some of the methods that enabled this work. It covers experimental techniques in Section 3.1, data analysis methods in Section 3.2. In Section 3.3, we look at Monte Carlo techniques that help us to develop a qualitative understanding of what part of the measured distributions are actually explained by our interpretation.

Definition of the Remi Coordinate System   Throught this work we will use in real space a Cartesian coordinate system, that is aligned with the REMI setup, see also Figure 3.1.2. We define the origin of the coordinate system as the crossing point between the FEL projectile and the SGJ target. The x-coordinate is aligned with the horizontal flow vector of the SGJ and the z-coordinate with the electric field, which points vertically towards the ion detector. To get right-handed coordinates, the y-axis is now required to point towards the FEL source point, perpendicular to both of the other axis. In momentum space, we use the same orientation as before, but in contrast, we choose a co-moving frame with the SGJ. As this brings the average velocity of the target molecules to zero, their average momentum will also be zero. This simplifies testing momentum conservation.

3.1 Experimental Methods

In this Section we want to gain an overview over the essential experimental techniques, that are necessary for our studies of fragmentation processes with momentum coincidence spectroscopy. First, the measurement of momenta with REMIs is described in Section 3.1.1. Second, the CEI method with a pump-probe scheme is described in Section 3.1.2. And third, the split-and-delay method to generate the pair of pump and probe pulse is described in Section 3.1.3.

3.1.1 Measurement of Momenta with Reaction Microscopes

The REMI is an apparatus to measure momentum vectors of charged particles. A REMI is usually implemented as a combination of a time-of-flight spectrometer, a homogeneous magnetic field to confine fast electrons inside the spectrometer and a position sensitive-detector, here consisting of a Micro Channel Plate (MCP) and a Delay Line Anode (DLA) [15, 23]. With this setup, we can describe the motion of charged particles as constantly accelerated along the Time Of Flight (TOF) direction, which we defined as the z-dimension. The Newton's equation of motion is

$$d = \frac{a}{2}t^2 + v_0 t = \frac{-qU}{2dm}t^2 + \frac{p_z}{m}t, \tag{3.1.1}$$

where d is the distance between the reaction volume and the detector, t is the particle's TOF, a is the acceleration due to the electric potential U at the distance d, q is the particle charge, v_0 is the initial velocity, which we can translate to the ratio of momentum p_0 and mass m of the particle. Note, that U has to be negative to attract the positive ions and positive to attract the negatively charged electrons. We can solve the equation of motion for the TOF

$$t = -\frac{d}{qU}\left(p_z + \sqrt{p_z{}^2 - 2qUm}\right), \tag{3.1.2}$$

or for the initial momentum

$$p_z = \frac{md}{t} + \frac{qU}{2d}t. \tag{3.1.3}$$
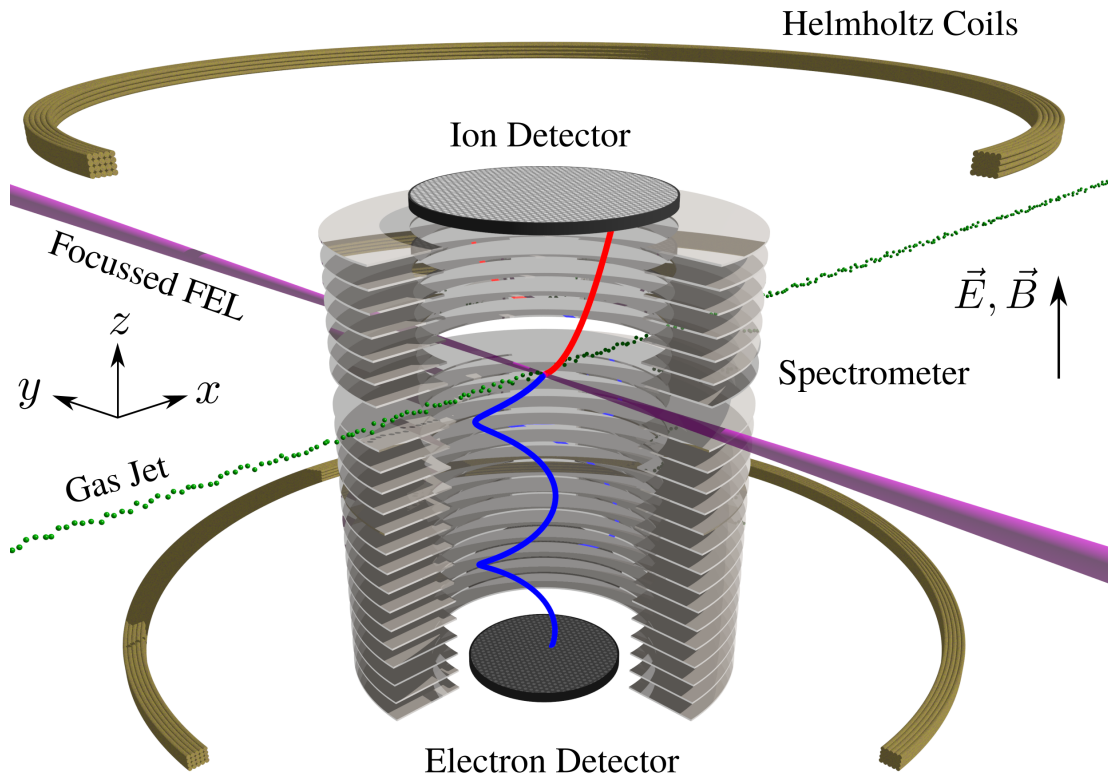
Figure 3.1.1: Illustration of the REMI. The target SGJ enters from the left and meets the focused FEL beam inside the REMI. The electric field accelerates ions towards the top detector and electrons towards the bottom detector. The magnetic field prevents the electrons from leaving the inner cylinder by forcing it on a spiral motion. The ring plates are connected by resistors, such that they create a homogeneous electric field between the two detectors. The Helmholtz coils around the setup produce a homogeneous magnetic field close to the central axis. Image taken from Schmid [22] with permission.

In the limit of low initial momenta, we get

$$\lim_{p_z \to 0} t = d\sqrt{-\frac{2m}{qU}}. \tag{3.1.4}$$

This means, all particles without momentum in z-direction will have their TOF determined purely by their mass-to-charge ratio and the electric potential and length of the spectrometer.

In transverse direction, the charged particles experience only the Lorentz force due to the magnetic field. As this force is always perpendicular to the velocity, it does not change the speed of the particle. It only rotates the velocity vector. This forces the particle on a circular trajectory in the transverse plane. The effective 3D trajectory is shown in Figure 3.1.2 for an electron. The initial momentum
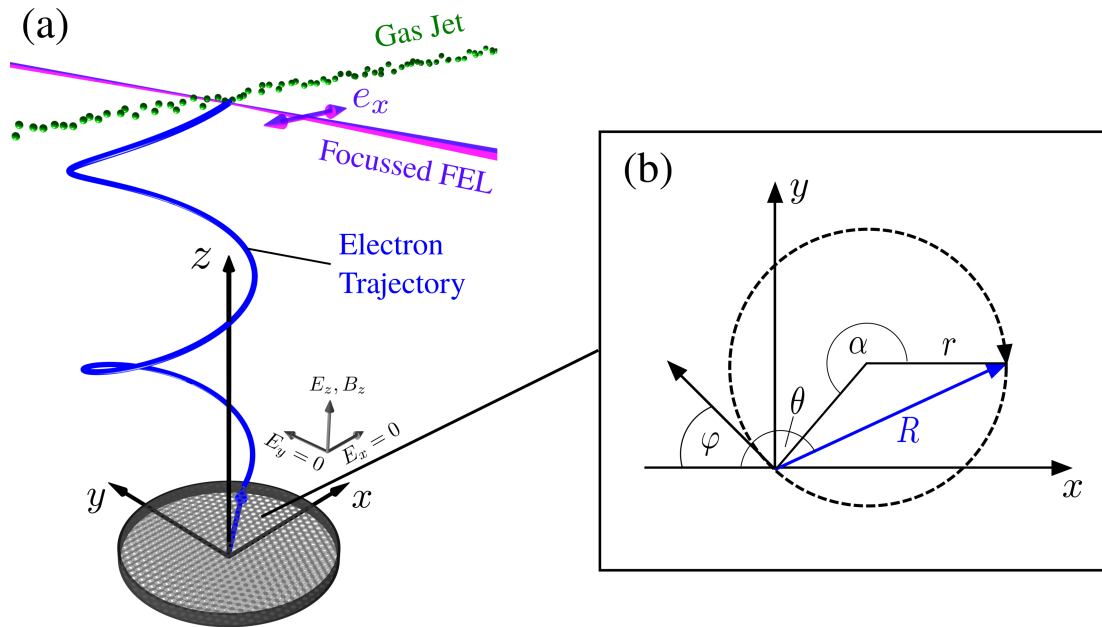
Figure 3.1.2: Left panel (a): Trajectory of an electron from the reaction volume onto the position sensitive detector. The coordinate system is defined by the crossing of SGJ and FEL, where positive x directs in the SGJ flow direction and positive y points towards the FEL source point. Positive z points towards the ion detector. Right panel (b): Circular motion of the electrons in the projection on to the transverse plane, see main text. Image taken from Schmid [22] with permission.

encloses the angle φ to the x-coordinate. The particle hits the detector at radius $R = \sqrt{X^2 + Y^2}$ and angle θ. It moves on a spiral trajectory with radius r and it

follows the circle until a specific phase. This phase is determined by

$$\alpha = \omega_c t = \frac{qB}{m} t, \qquad (3.1.5)$$

where t is the TOF and ω_c the cyclotron frequency, which is proportional to the magnetic flux density B. We can derive by some trigonometry, that

$$\varphi = \theta - \frac{\alpha}{2} \Leftrightarrow \alpha = 2\left(\theta - \varphi\right), \qquad (3.1.6)$$

where θ is the angle between the x-axis and the vector to the detector hit. Furthermore the cyclotron radius is also connected to the momentum and the magnetic flux density by

$$r = \frac{p_\perp}{qB}, \qquad (3.1.7)$$

where $p_\perp$ is the momentum magnitude in the plane transverse to the magnetic field. Combining Equations (3.1.5) to (3.1.7) and, from further trigonometry, $r = R/\left(2\sin\frac{\alpha}{2}\right)$, we can solve for $p_\perp$ and φ, arriving at

$$\varphi = \theta - \frac{\alpha}{2} = \theta - \frac{qB}{2m} t \qquad (3.1.8)$$

$$p_\perp = rqB = R\frac{qB}{2\sin\frac{\alpha}{2}} = R\frac{qB}{2\sin\left(\frac{qB}{2m}t\right)} \qquad (3.1.9)$$

$$p_x = p_\perp \cos\varphi \qquad (3.1.10)$$

$$p_y = p_\perp \sin\varphi. \qquad (3.1.11)$$

Note that in the limit of small α we have to consider the $x/\sin x$ limit and get

$$\lim_{\alpha \to 0} p_\perp = R\frac{qB}{2\frac{qB}{2m}t} = \frac{Rm}{t} = v_\perp m. \qquad (3.1.12)$$

With this we have recovered the simple velocity measurement of a uniform linear motion in a force-free system with $v_\perp = R/t$. The cyclotron phase is proportional to the magnetic flux density and the charge-to-mass ratio

$$\alpha = \frac{qB}{m} t \propto B\sqrt{\frac{q}{m}}, \qquad (3.1.13)$$

since $t \propto \sqrt{m/q}$, see Equation (3.1.4). We can safely apply the limit for heavy

ions or very low magnetic fields. For electron measurements we will always have to consider magnetic fields due to the low mass of the electron. In the limit of $\alpha \to 0$ we can calculate the impact position from the initial momentum and the SGJ velocity by

$$
\begin{aligned}
x = (v_x + v_{\text{jet}})t & = \left(\frac{p_x}{m} + v_{\text{jet}}\right)t && \text{and} \\
y = v_y t & = \frac{p_y}{m}t && . \quad (3.1.14)
\end{aligned}
$$

The jet velocity only goes into the x coordinate, as we defined the coordinate system along the average velocity vector of the SGJ.

In practice, several complications arise in the measurement procedure. The timing and positioning of the intersection of target molecules and projectile pulse is not precisely known as well as the rotation relative to the detector. We therefore have to substitute in the previously idealized formulas the variables

$$
t \to t - t_0, \quad (3.1.15)
$$

$$
x \to x - x_0, \quad (3.1.16)
$$

$$
y \to y - y_0 \text{ and} \quad (3.1.17)
$$

$$
\theta \to \theta - \theta_0. \quad (3.1.18)
$$

Additionally, on the last few mm before the MCP, we have to significantly increase the electric field in order to reach sufficient kinetic energy to trigger the MCP. This section therefore has an in-homogeneous acceleration and we can not simply use the above formula. However, in the usual settings, all ions gather significantly more momentum from the acceleration due to the electric field compared to their initial momentum. This means, that the variation of the TOF in this specific section due to the initial momentum can be safely neglected. Therefore we can subtract a time offset δ from the measured TOF, that only depends on $\sqrt{m/q}$, see Equation (3.1.4). After doing that, we can safely apply Equation (3.1.3), see Reference [24].

3.1.2 Pump-Probe Coulomb Explosion Imaging

To explore the structure and dynamics of small clusters, we use the CEI technique. This method was developed already in the 70s with ion beam experiments [25]. In those experiments, a fast beam of molecular ions, typically several MeV of kinetic energy, hits a thin fixed target foil. The foil strips electrons from each of the atoms in the molecule and the remaining ions repel each other. Behind the foil target one places imaging detectors to record the ion pattern. As the collision happens suddenly, with a contact time below femtoseconds, the derived structure is accurate. To study neutral molecules, a target molecule can be ionized with a beam of highly charged ions that strip away electrons from the neutral [26]. The method was extended in the 90s to a pump-probe scheme using the then available fs lasers [16] and since then is still in development and discussion, see e.g. Reference [27]. In Figure 3.1.3 we can see, how the CEI method gives us insight
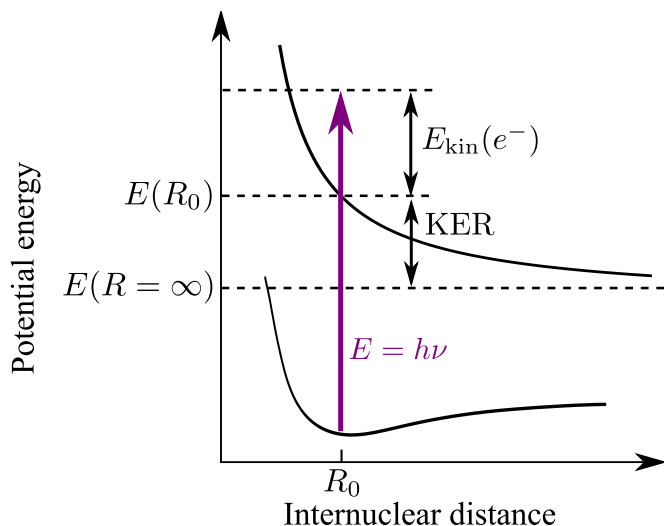
Figure 3.1.3: Coulomb Explosion Imaging in the static case. The molecule is in the ground state and then transfered by a single photon to the excited repulsive potential. The measured Kinetic Energy Release (KER) is directly connected to the initial distance R_0. Image taken from Schnorr [28] with permission.

on the structure of a molecule in the simplest case of a diatomic molecule. The molecule is in its ground state potential at internuclear distance R_0. The photon pulse ionizes the molecule, which brings it to the repelling potential curve. The excess energy between the photon energy and that potential curve is transfered to

the electron as kinetic energy

$$E_{\mathrm{kin}}\left(e^-\right) = h\nu - E\left(R_0\right). \qquad (3.1.19)$$

The difference between the new potential at R_0 and at infinity will be the kinetic energy release of the ionic fragments

$$KER = E\left(R_0\right) - E\left(\infty\right). \qquad (3.1.20)$$

This measurement allows to reconstruct the absolute square of the initial state spatial distribution by the so-called reflection approximation [29], as it is mapped directly to the final state potential. In the extension to a pump-probe scheme, we have to consider, that the molecule undergoes a certain time evolution on the intermediate state, see Figure 3.1.4. When the intermediate state is bound, we
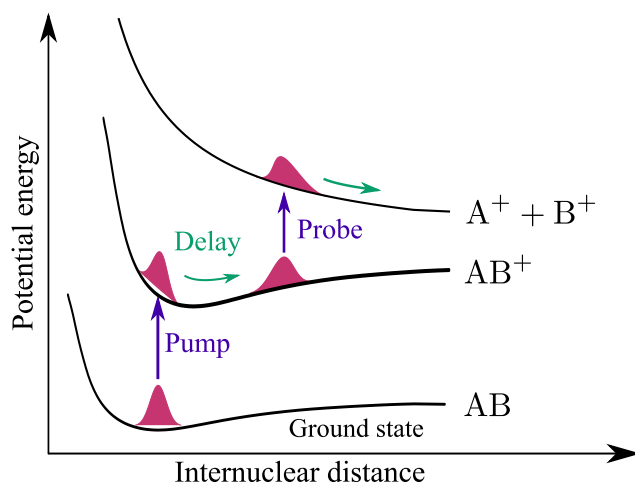
Figure 3.1.4: Time resolved variant of CEI. The pump pulse transfers the molecule from the ground state AB to the bound molecule ion state AB^+. The molecular ion evovels on the potential curve until the probe pulse transfers it to the fragmenting A^+ / B^+ state. Image taken from Schnorr [28] with permission.

now map the intermediate state at the time delay of the probe pulse instead of the initial state. However, this only holds, when the molecule gathers negligible kinetic energy in the intermediate state in comparison to the final state. The situation is more complicated, when we consider, that one of the intermediate states might already be a Coulomb-like potential, as shown in Figure 3.1.5. Then, the final KER depends both on the distribution of the initial state through $V(t_0)$
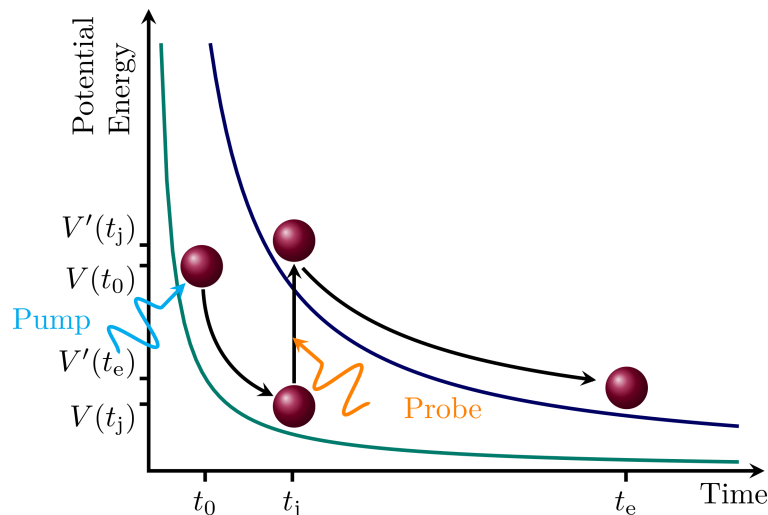
Figure 3.1.5: Another variant of time resolved CEI. In contras to Figure 3.1.4, here the molecule goes through an intermediate state, that is already strongly repulsive. The molecule accumulates significant kinetic energy before the probe pulse transfers it to the final state. Image taken from Schnorr [28] with permission.

and the position at the time we probe the system t_j. The KER is then

$$\text{KER} = V(t_0, R_0) - V(t_j, R_j) + V'(t_j). \tag{3.1.21}$$

However, as R_j depends on R_0, the analysis of the KER is now not as trivial as before. We will therefore rely on a simulation of the process to help our understanding of this. The simulation is described in Section 3.3.6.

3.1.3 Split Beam Focus Overlap in Grazing Incidence

In order to produce the pair of a pump and a probe pulse from the FEL we use a pair of plane mirrors. The mirrors are positioned as a lower half and an upper half with a small horizontal gap in between (see also Figure 4.2.3). The upper half can be translated in the normal direction and rotated around the two other dimensions. The FEL beam is aligned on the centre, such that equally sized parts of it illuminate the two mirrors. The translation of the upper mirror creates a path difference between those two parts, as sketched in Figure 3.1.6. However, we use an ellipsoidal mirror after the beam splitting mirror for focusing of the beams. As an ellipsoidal mirror creates a point-to-point image of one focus into the other focus of the ellipse, we have to slightly rotate the translated mirror half.
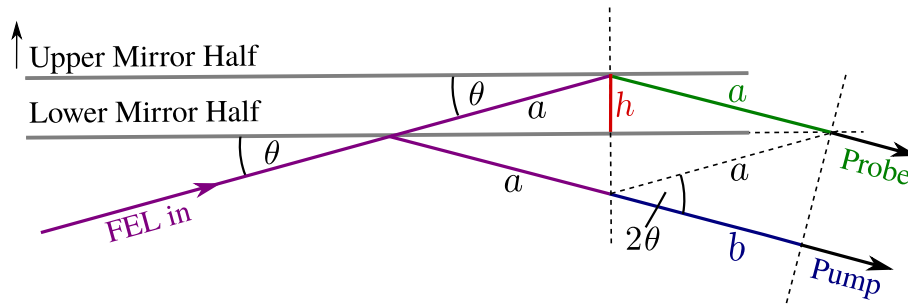
Figure 3.1.6: Construction of the path difference between reflections on the upper or lower half mirrors. The upper mirror is displaced by a distance h and the FEL beam comes in under the angle $\theta \approx 8°$. The path difference is $a - b = 2h \sin \theta$. Image taken from Schmid [22] with permission.

Otherwise the virtual source point behind the two plane mirrors would not overlap and therefore also the focus spots would not overlap. In Figure 3.1.7 we see, how a small rotation brings the beams back together. For the experiment it is crucial to
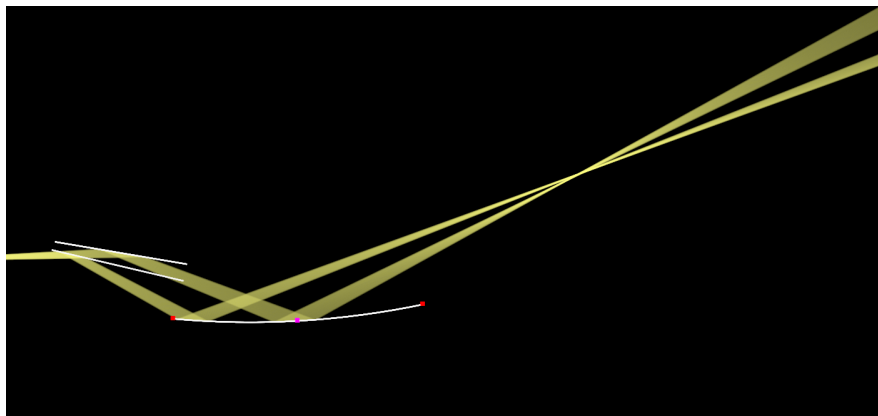
Figure 3.1.7: Illustration of the beam path (Not to scale). The divergent beam comes from the left, is split and delayed by the split plane mirror and then both beams are focused into the same spot. In order to focus into the same spot, the movable part of the split mirror has to be slightly rotated.

validate the overlap between the beams in the focus both temporally and spatially. To do this, we use a fluorescence screen, placed directly in the focus. The required analysis will be discussed in Section 3.2.4.

3.2 Data Analysis

For the analysis of the REMI data, we use the Grand unifiEd reactioN microscopE souRce Code (GENERiC), originally developed in the thesis project [30]. It is implemented as a shared library in the GSI Object Oriented On-line Off-line system (Go4) framework [31]. Go4 itself is based on CERNs ROOT data analysis framework (ROOT) [32] and adds, for example, a versatile user interface, modular analysis steps with storage of intermediate results or transfer of histogram data to the user interface from remote analysis servers. The analysis was later adapted to the specific situation at the Free electron LASer in Hamburg (FLASH), such as the burst mode or inclusion of online streams of facility properties. The development continued since the initial implementation in several thesis projects and the general procedures were described within those [22, 28].

In this section we will not discuss the procedures in GENERiC, but rather the results that we get from it. The results were further processed and visualized in Python, with the help of several Python packages, especially those in the References [33–42]. Section 3.2.1 will discuss, what observables are available from the output of the analysis code. Section 3.2.2 will describe a visualisation method for the energy sharing in a three particle fragmentation, the so-called Dalitz plot. In Section 3.2.3 we show, how we can use the covariance spectrum to subtract background signals. Finally, in Section 3.2.4 we will discuss the image analysis, that is necessary to validate the overlap of pump and probe pulse.

3.2.1 Observables in a Reaction Microscope Measurement

From the measured momenta of ions, we can derive several observables. The first important one is the momentum vector sum for a given fragmentation channel. For example, if we want to identify reactions into the ^{129}Xe^{1+} / ^{129}Xe^{2+} fragmentation channel, we will calculate the sum of the momentum vectors for each combination of a ^{129}Xe^{1+} and a ^{129}Xe^{2+} that were detected in the same pulse. We will find, that a peak of events arises, where the momentum sum is zero because of momentum conservation. See also Section 3.3.4 for more details. We will consider all events in this peak as coincident events, that originate from the same target ^{129}Xe$_2$ dimer. In CE processes, almost all of the absolute momentum arises from the repulsion between ions, we can neglect the electron momenta when identifying reaction
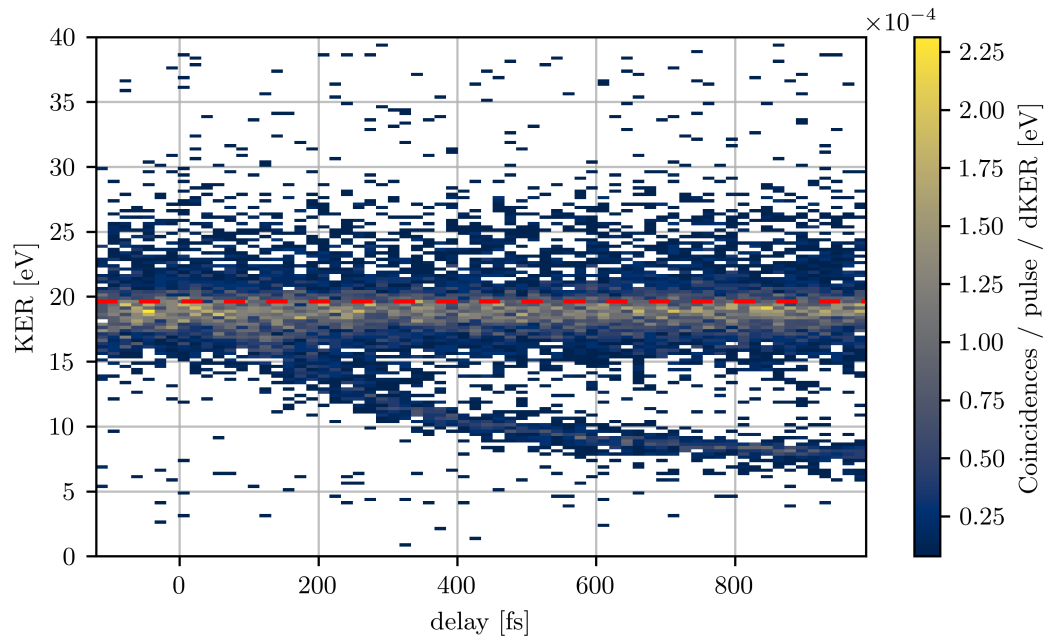
Figure 3.2.1: Example of a KER versus delay histogram. We see how the distribution of the KER changes when we vary the time delay between the FEL pulses.

channels. Now we can further calculate the kinetic energy of each ion in the coincidence from their momenta and get the KER as the sum over those energies. In coincidences we can also calculate the relative angles between the particle momenta. In two ion coincidences, this mainly serves as another plausibility check, as we have to get a relative angle of $\approx 180°$. In coincidences of three or more particles, this can give further insight on how the dissociation proceeds, see e.g. [24]. Often we are interested in the event rate of coincidences as a function of experimental parameters such as the pump-probe delay or the FEL intensity. Or even depending on both of the above observables and another external parameter, such as the histogram of KER versus delay in Figure 3.2.1.

3.2.2   Dalitz Plot

The Dalitz plot is fundamentally a ternary plot, a visualisation of the sharing of a common pool of a positive quantity between multiple entities. When we do this for three particles, there are only two degrees of freedom: The share of the first two, and the third particle receiving the remaining. Conveniently, equilateral

29

triangles have just the property that helps us with this visualisation. For any given point, the sum of the distances to each of the sides is equal to the height of the triangle. This is known as Viviani's Theorem and can be generalized to higher dimensions [43] and therefore also Dalitz plots can be generalized to higher dimensions [44]. To calculate the values going into the plot, we first normalize the energy of each particle to the sum of all three energies.

$$E_{\text{sum}} = \sum_i E_i \text{ and} \tag{3.2.1}$$

$$\epsilon_i = \frac{E_i}{E_{\text{sum}}}. \tag{3.2.2}$$

Now we want to place the triangle such, that the top corner corresponds to $\epsilon_1 = 1$, the lower left to $\epsilon_2 = 1$ and the lower right to $\epsilon_3 = 1$. Further, we want to center the representation, such that equal sharing of all three energies is at $(0, 0)$. With those conditions, the Cartesian coordinates can be expressed trough

$$X = \frac{\epsilon_2 - \epsilon_3}{\sqrt{3}} \text{ and} \tag{3.2.3}$$

$$Y = \epsilon_1 - \frac{1}{3}. \tag{3.2.4}$$

Due to momentum conservation, we can not get results in the whole triangle, but only inside the incircle of the triangle. Figure 3.2.2 shows, how the momentum constellation shifts from equilateral to linear from the center of the plot to the outer circle. There are two variants of linear constellations. One variant has two larger momenta and one close to zero, the other variant has one large momentum, corresponding to nearly half the kinetic energy, and two smaller ones, each with roughly one quarter of the kinetic energy. One should keep in mind, that this visualisation shows "just" the sharing of energy between the particles. The relation between the molecular structure and a given spot on the Dalitz plot is not necessarily symmetric, meaning that multiple structures or, more precisely , multiple pathways of fragmentation could lead to the same sharing of the final kinetic energy. We can however use the plot to exclude possible structures, that would end up in an area of the Dalitz plot, where no events are observed or possibly the rate of detection is suppressed at certain experimental parameters.
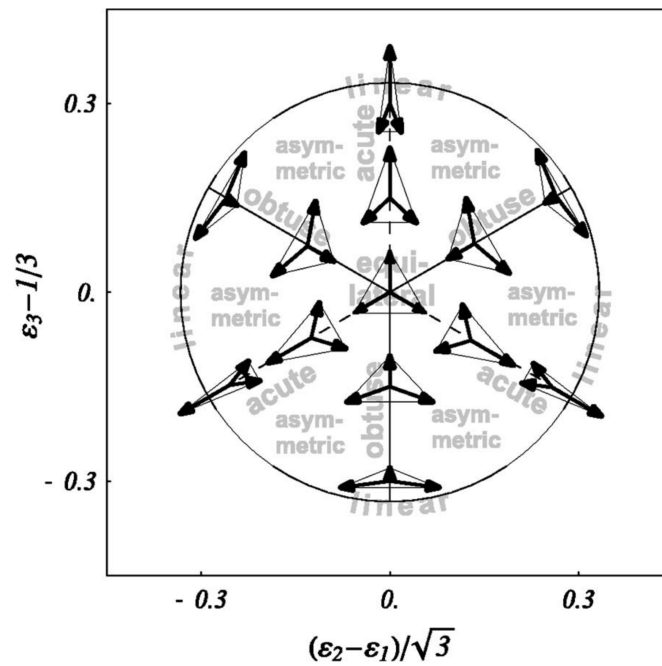
Figure 3.2.2: Different constellations of momentum vectors shown at the respective coordinates of the Dalitz plot. Reprinted figure with permission from [[45] Galster et al., Physical Review A, 72, 062506, 2005] Copyright (2005) by the American Physical Society.

3.2.3 Background Subtraction with Covariance

In the Xe experiment presented in Chapter 5, we want to analyse the electrons energies although the experimental conditions are not ideal for a REMI measurement with electrons. The limitation n the sensitivity to all electrons is due to the fact that we can only detect few electrons in the relevant energy range from the same pulse due to the detector dead time. However, many electrons, even from a single cluster, are expected. Given that we measure sometimes monomer ion charge states above 11 charges and that the cluster density is lower than the monomer density, we expect to have many electrons with each coincidence in the desired ion channel. Unfortunately, the momentum sum also does not help, as we do not have sufficient resolution in the ion momenta to match them with the electrons. Therefore we use another method to remove background data, the so-called covariance spectrum. The idea behind the covariance spectrum is, that we calculate an expected background spectrum and subtract it from the measured correlated spectrum. The calculation is based on the usual formula for calculating the covariance from expectation values

$$\mathrm{cov}\left(E_e, C_\mathrm{i}\right) = \mathrm{E}\left[E_e|C_i\right] - \mathrm{E}\left[E_e\right]\mathrm{E}\left[C_i\right], \tag{3.2.5}$$

where E_e is the electron energy and C_i is the occurrence of a coincidence in the channel i. The covariance method has been in use in similar high rate scenarios, e.g. in [46]. The term of $\mathrm{E}\left[E_e\right]\mathrm{E}\left[C_i\right]$ is the product of the average electron spectrum and the average rate of events for the coincidence C_i. That product corresponds to the expected average background spectrum for any pulse. The term $\mathrm{E}\left[E_e|C_i\right]$ is the average spectrum of electrons, that are detected in a pulse, where also the coincidence C_i was detected. As an example, we can see the procedure for Xe^{2+} and Xe^{3+} in Figure 3.2.3. The $\mathrm{E}\left[E_e\right]$ term is shown in the top panels, the middle pannels show $\mathrm{E}\left[E_e|C_i\right]$ and $\mathrm{E}\left[E_e\right]\mathrm{E}\left[C_i\right]$ and the bottom panels show the $\mathrm{cov}\left(E_e, C_\mathrm{i}\right)$ spectra.

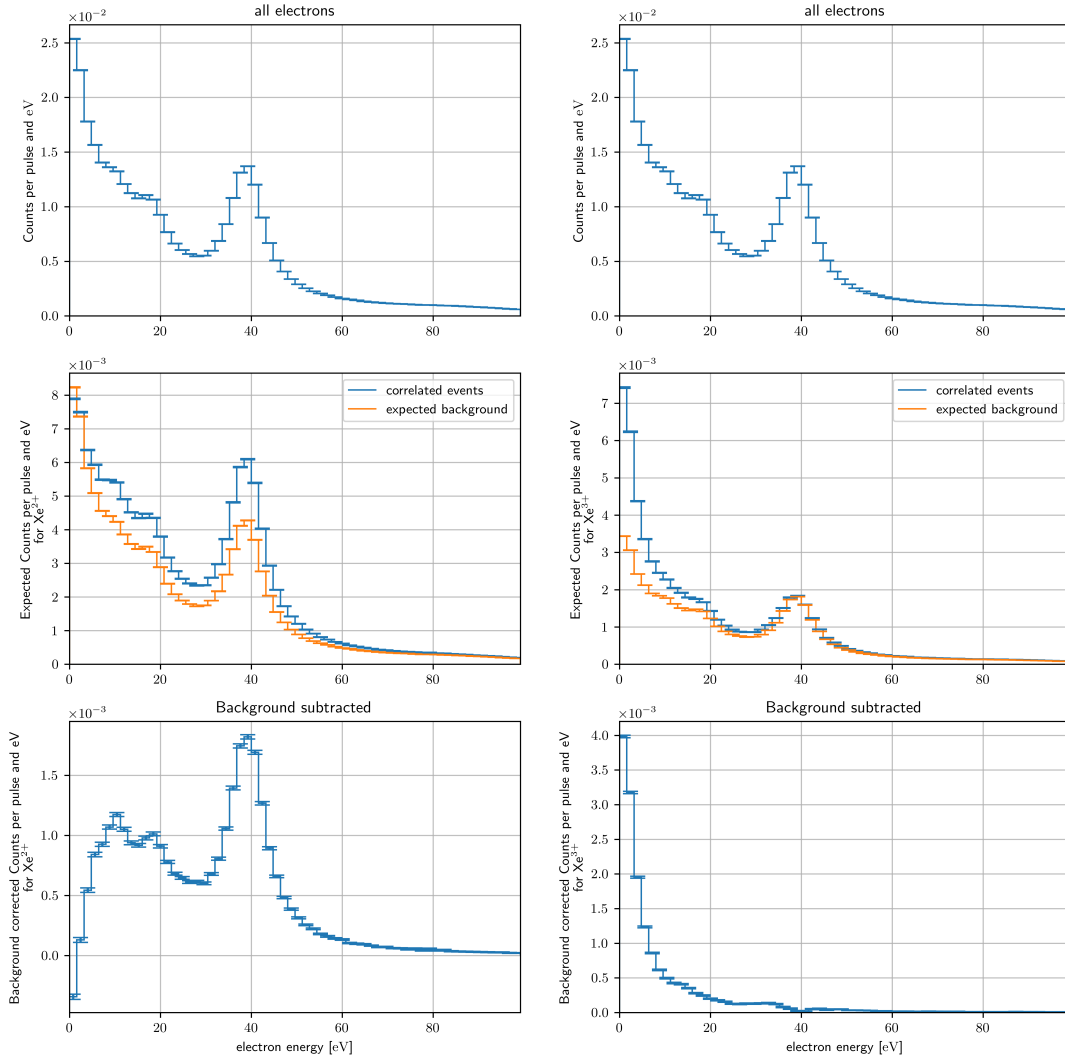Figure 3.2.3: Background subtraction for electron energy spectra. Left: Electrons correlated with Xe^{2+}. Right: Electrons correlated with Xe^{3+}. The top panels show the average rate of electrons within each energy bin. The middle panels show the expected background and the correlated spectrum of electrons, that were measured in the same pulse as the corresponding ion. The bottom panels show the difference of the two.

3.2.4 Focus Image Analysis — How to find the Overlap

The two parts of the FEL beam must be overlapped both temporally and spatially. The spatial overlap is defined such, that both beams pass the focal plane through the same spot. The temporal overlap is defined by the setting of the delay stage, where both beams pass the focal spot at the same time. In order to check the temporal overlap, we use a red alignment laser with short coherence time and a wavelength of $\lambda = 658\,\text{nm}$. When we illuminate both mirrors, as we would do with the FEL, we see an interference pattern on the screen positioned in the focus. With the delay mirror we can shift the phase of the delayed pulse and therefore shift the phase of the interference pattern. In Figure 3.2.4 we can see
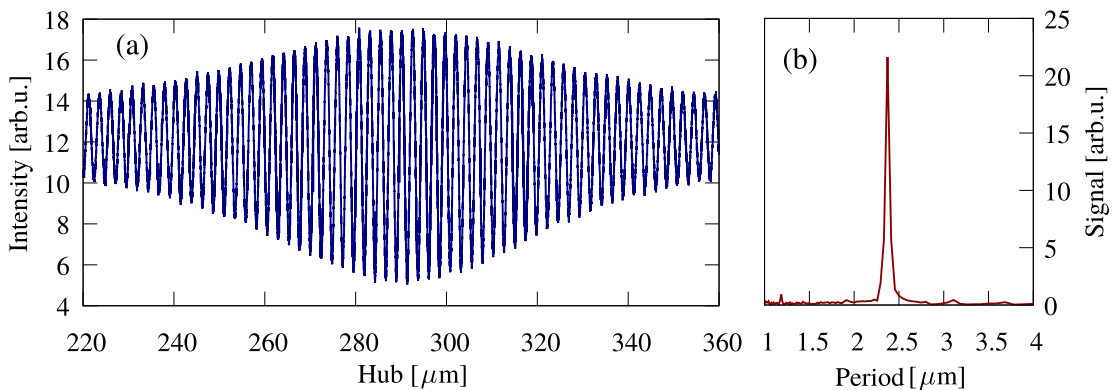
Figure 3.2.4: (a) Temporal overlap scan with a 658 nm alignment laser. The intensity is measured by integrating over a thin slice along the interference line. The intensity in the slice varies with varying translation of the delay stage. (b) Fourier transform of the intensity signal in (a). Taken from [22] with permission.

the interference of the alignment laser on the focus screen. The envelope of the oscillation is due to the short coherence time and the maximum of the envelope directly marks the temporal overlap. From the Fourier transform of the signal we can retrieve a period of $p = 2.375\,\mu\text{m}$. Together with the laser wavelength, we get the calibration factor for the conversion between mirror translation Δ and time delay

$$\tau_{\text{fs}} = \frac{\lambda}{pc_0} \cdot \Delta = 0.924\,\frac{\text{fs}}{\mu\text{m}} \cdot \Delta, \tag{3.2.6}$$

see Reference [22].

Maintaining the spatial overlap while scanning the delay turned out to be more complex than expected. To keep the spatial overlap position the same, normally

one needs to rotate the delay mirror around the vertical axis additional to the translation adjusting the time delay. The relation between the translation and the necessary angle is further expected to be linear, as the focus is $1.3\,\mathrm{m}$ behind the mirror and we only move the mirror up to $3\,\mathrm{mm}$. That is clearly a small angle, however the relation turns out to be erratic. In Figure 3.2.5, we see different measurements of the FEL spot centroid during delay scans of $\pm 2\,\mathrm{ps}$. Although it is

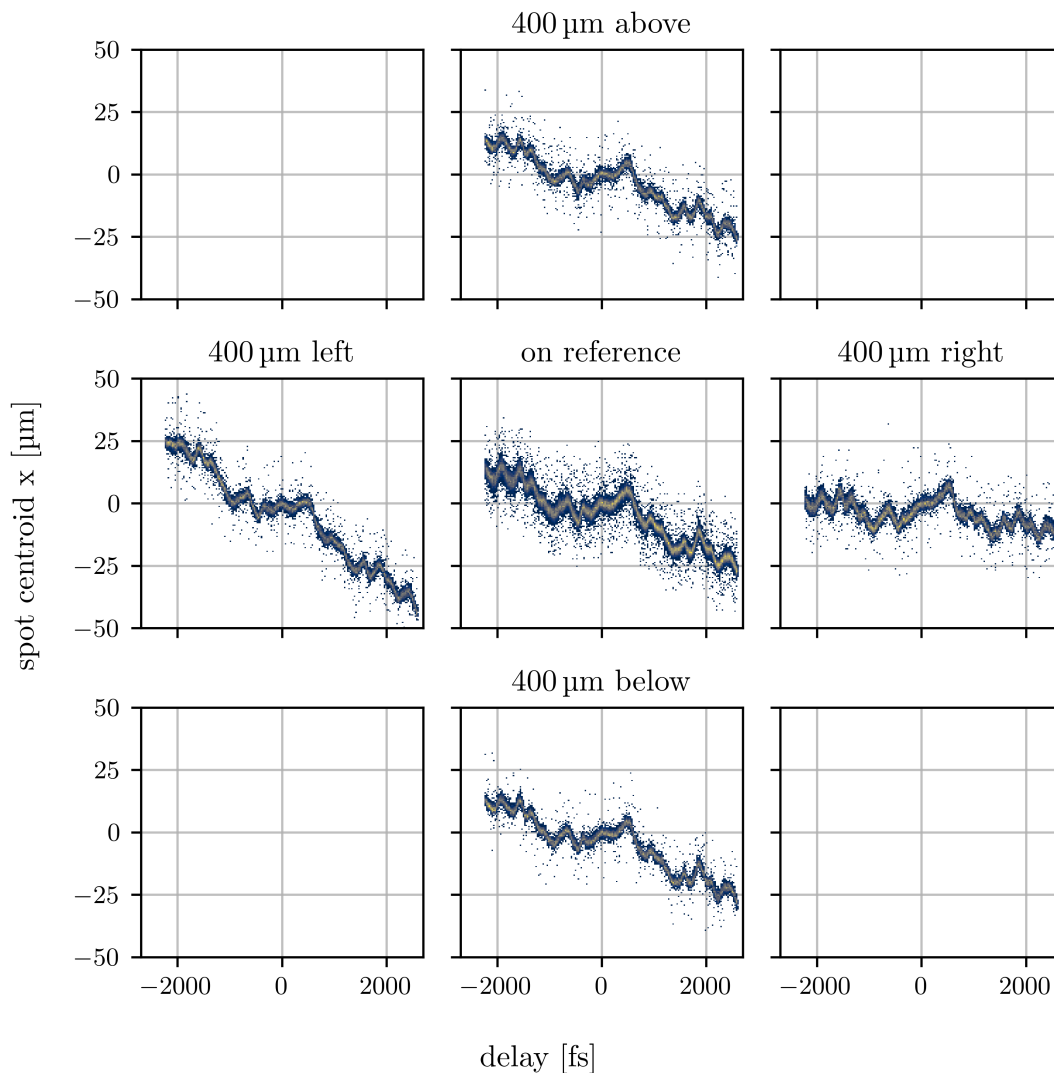Figure 3.2.5: Horizontal deviation of the FEL spot centroid from the reference position with varying delay. The measurement in the centre panel was referenced to the static beam, the other measurements were referenced to $400\,\mathrm{\mu m}$ from the static beam in horizontal or vertical direction.

not optimal in this example, linear compensation is already applied to correct for a displacement on the order of $-2\,\mathrm{mm}$ to $2\,\mathrm{mm}$. The remaining erratic curve varies with a maximal amplitude of roughly $10\,\mu\mathrm{m}$ to $30\,\mu\mathrm{m}$. This would be too much for a focus size of below $10\,\mu\mathrm{m}$, and we achieved in the commissioning around $3\,\mu\mathrm{m}$ to $4\,\mu\mathrm{m}$(FWHM) in the focus diameter. In first measurements, this lead to drastic suppression of multi-photon signals, especially the pump-probe signals at more or less random regions of delay. Additionally, data taking for the focus position can not be done simply on the position of the static beam, as it is hard to differentiate two spots, that should be on the same position with the same size. One possibility would be to block the static beam, but for an unstable beam position at the same time, there is no way to know where now the static beam would be.

To overcome this issue, we established a routine, where we displace the delay focus and monitor the position of both beams. This way, we always have a reference on the screen and can calculate the difference of the two positions. Figure 3.2.6 shows results for this type of scans with a displacement of $400\,\mu\mathrm{m}$ in horizontal or vertical direction. With the displacement of the spot, also the shape of the erratic curve changes with an additional linear trend. To use the gathered data as a correction lookup table, we interpolate the histograms by a spline. The spline is damped in order to prevent resonant overfit behaviour and the dampening parameter is optimized by Leave One Out Cross Validation (LOOCV). Exemplary data and the corresponding splines can be seen in Figure 3.2.6. To get the required mirror rotation at the desired spot position the splines from the four measurements are averaged, see Figure 3.2.7.

Once we obtain a correction curve, we perform another scan at the reference position to validate the result. In Figure 3.2.8 we can compare the horizontal displacement between the rough linear correction and the new lookup table correction. With the new correction we managed to keep the centroid within a $\pm2.5\,\mu\mathrm{m}$ band around the reference position.

This method to find the pump-probe overlap was developed in preparation and during the Xe experiment. In later beamtimes better stability of the focal spot was achieved. That allowed to simplify the procedure through blocking the static beam and directly measuring at only one point instead of four. Additionally we, extended the motor controls and imaging LabView software in a way, that an automated creation of the lookup table is done. For this, we declare a list of
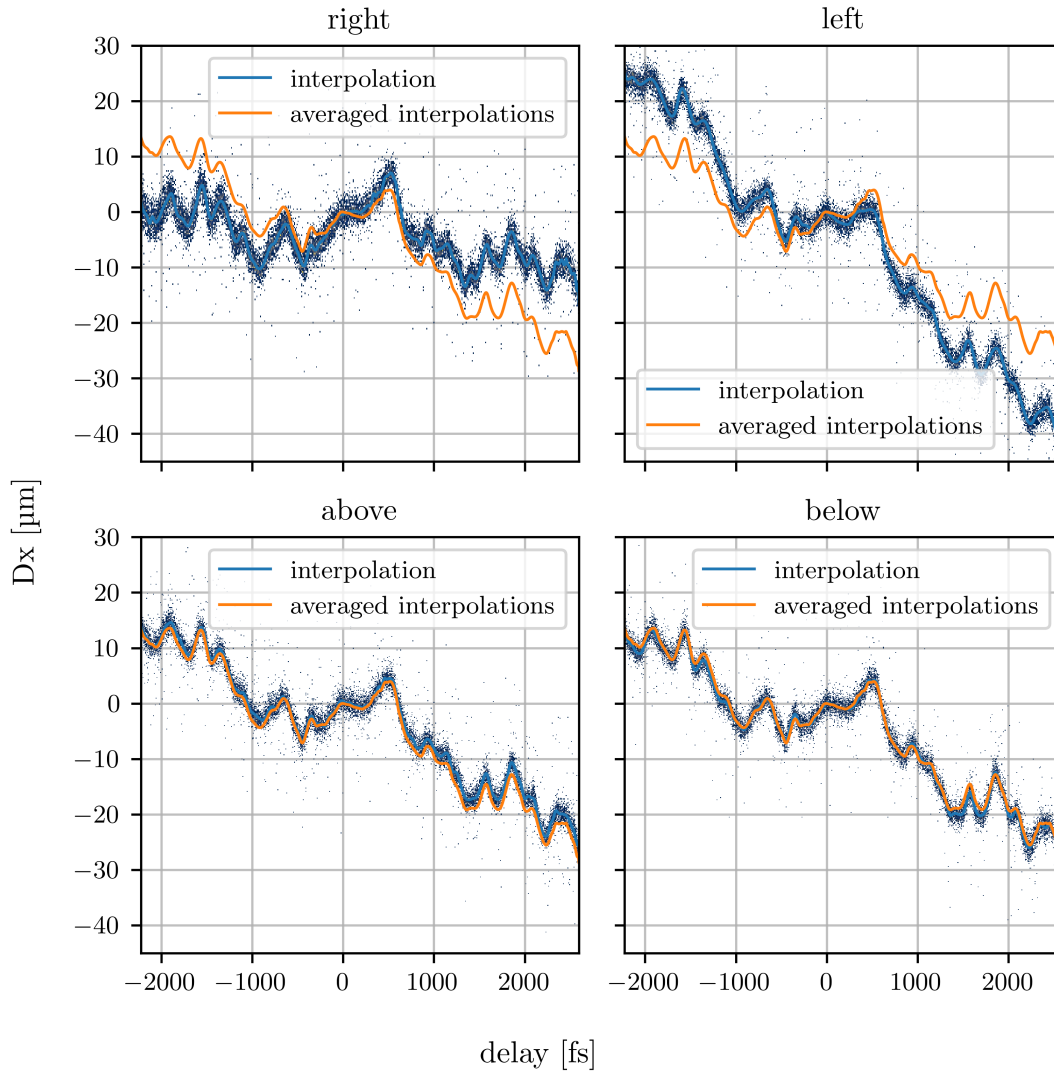
Figure 3.2.6: The four off reference measurements as in Figure 3.2.7 together with the respective spline interpolations
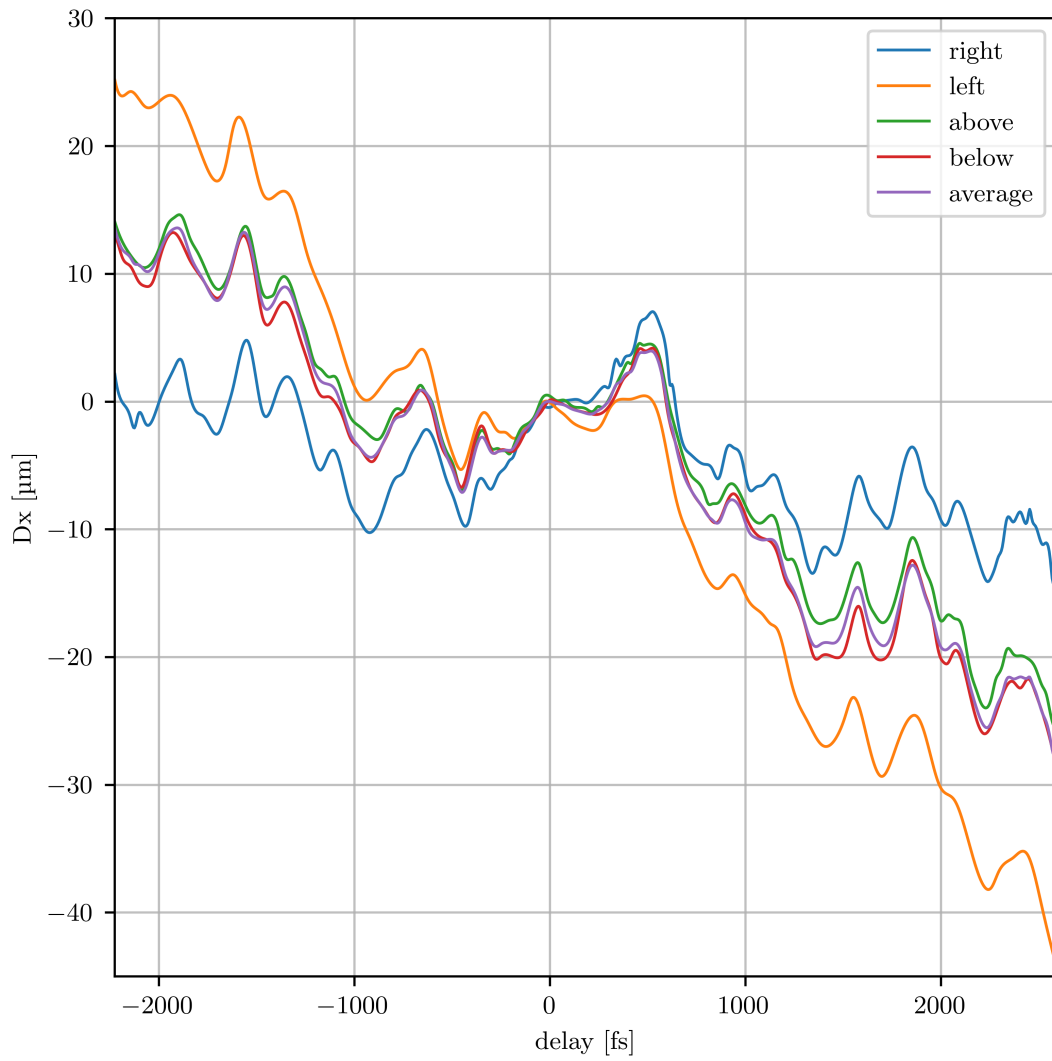
Figure 3.2.7: Splines from the four measurement points and their average curve.
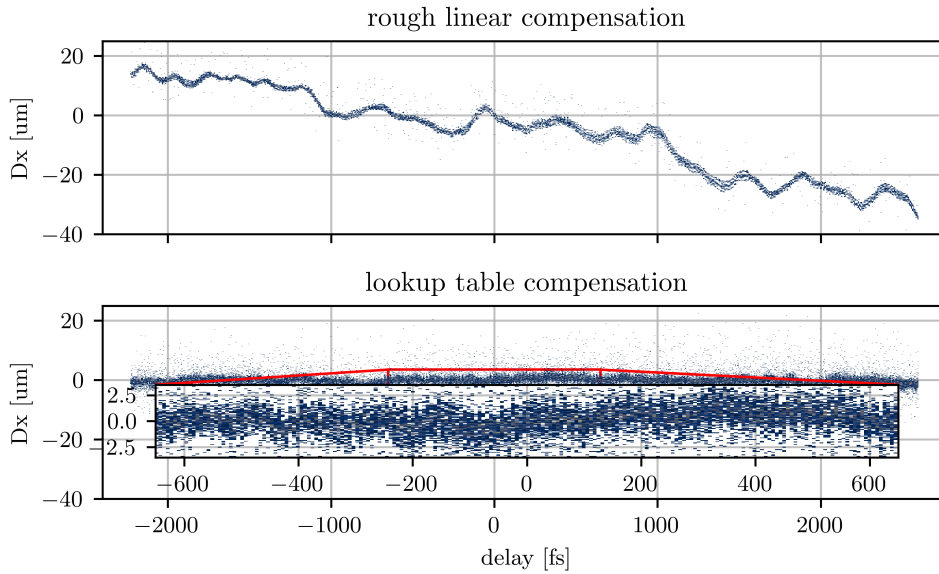
Figure 3.2.8: Comparison between the linearly corrected delay scan and the correction with a lookup table. The inset in the lower panel shows a zoom into the delay range from $-650\,\text{fs}$ to $650\,\text{fs}$ and horizontal deviation from $-3.5\,\mu\text{m}$ to $3.5\,\mu\text{m}$.

desired delay positions to iterate through in a measurement. Then we observe the spot and directly manipulate the correction values for the current delay until the spot is stable within a given tolerance to the reference point. Once the spot and the correction values remain stable over several images, we go to the next step in delay. With this procedure we can collect just enough data for each delay step and go through the scan as quickly as possible while staying within the tolerance. This way we circumvent the need for long data taking of "just" the position of the focus spot and the not fully automatized analysis of the scan data, where especially the optimisation of the spline functions had to be checked thoroughly. In comparison, the four-points scan took roughly 30 min to 60 min for each point and additionally another 30 min for analysis, while the direct, automatic procedure takes roughly 20 min to 30 min in total. Considering, that measurement time at FELs is very costly and limited, this was an important optimization to increase the amount of data taken for the actual experiment.

3.3 Monte Carlo Simulations of the Remi Experiment

We used for the analysis of the Xe momentum data many methods that were developed in our group and other groups of our field. In order to develop a deeper understanding of the methods, how they work, when and why they can be effective, we will look into Monte Carlo simulations of several methods. We will start in Section 3.3.1 with simply describing how the different isotopes of xenon form clusters and result in the observed mass spectrum. Next we develop Monte Carlo methods to randomly sample TOF and position detector hits of those clusters in Section 3.3.2. Continuing from there, we develop in Section 3.3.3 sampling momenta of a Coulomb explosion in a dimer's centre-of-mass frame and finally transforming them into detector hit samples. Next we will look at how we select coincidence channels by their momentum sum in Section 3.3.4 and find our limitations with respect to distinguishing isotope combinations of the clusters. Combining what we have achieved in those previous sections, we use our simulated models to tune the momentum calibration in Section 3.3.5. Finally we use a Molecular Dynamics simulation (MD) in Section 3.3.6 to reproduce the essential characteristics of the charge and energy transfers in Xe in simulated pump-probe measurements.

3.3.1 Isotope Combinatorics of Xenon

As Xe comes with many different stable isotopes in nature, see Table 3.1, we will see a manifold of peaks in the TOF spectrum for each charge state. When integrated, each peak should be proportional to the natural abundance of the respective isotope. Furthermore, there will be a random selection of isotope combinations when forming clusters, and the cluster mass distribution can become quite complex. The structure of five dominant peaks for atomic Xe transforms to a Poisson-like continuum distribution for large cluster sizes. We can see the mass distributions together with the relative contribution from each combination in Figure 3.3.1. In order to calculate the distribution of masses in a cluster, we can write down all possible combinations and get the abundance of each combination as the product of abundances of the individual parts. Alternatively we can directly get a representative random sample of the N-particle cluster mass by sampling
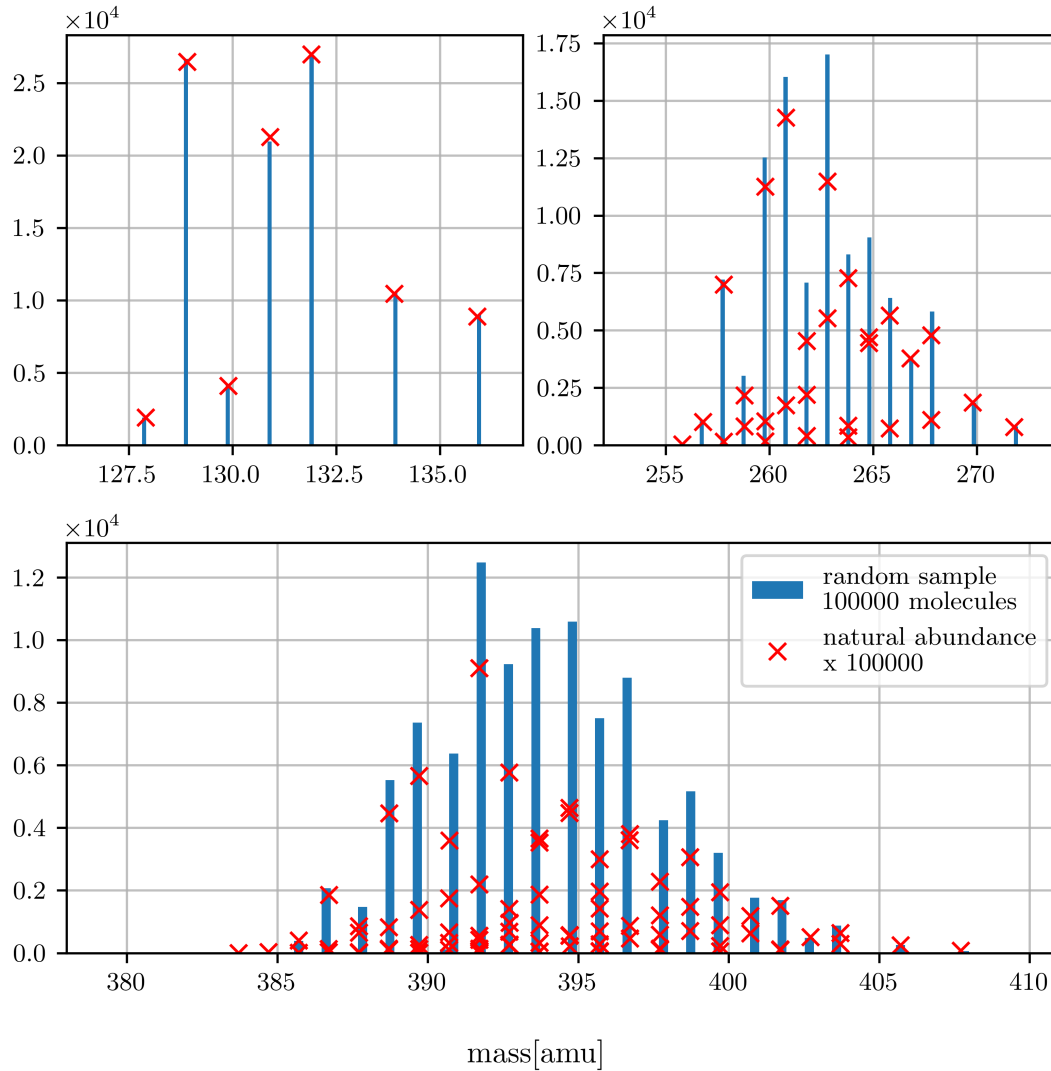
Figure 3.3.1: Distribution of mass from the natural abundance of Xe isotopes. The histogram in blue bars is from sampling of N atoms out of the natural abundance for each N atom cluster. The red crosses mark the natural abundance of unique mass combinations of isotopes summing up to the indicated mass. Top left: Xe monomers. Top right: Xe dimers. Bottom: Xe trimers.

Isotope	Mass / u	Abundance / %
^{128}Xe	127.903 531	1.91
^{129}Xe	128.904 780	26.4
^{130}Xe	129.903 509	4.1
^{131}Xe	130.905 072	21.2
^{132}Xe	131.904 144	26.9
^{134}Xe	133.905 395	10.4
^{136}Xe	135.907 214	8.9

Table 3.1: Natural abundance of Xe isotopes. Table adapted from [47], only isotopes with abundance higher than $1\,\%$ are listed.

from the single particle distribution N times and sum up the results. We will use the latter approach in the following sections, as we anyways want a sample of clusters.

3.3.2 Random Sampling Reaction Microscope Ion Hits

In order to calculate realistic detector hit distributions, we first need to generate a realistic sample of target momenta. We start with sampling a combination of isotopes from the natural abundance (see Section 3.3.1) and give them a random momentum vector, where each component is sampled independently from a normal distribution with width according to the momentum resolution of the REMI

$$p_i \propto \mathcal{N}\left(0, \sigma_i\right), \tag{3.3.1}$$

where $\sigma_x \approx \sigma_y \approx 4\,$a.u. and $\sigma_z \approx 2\,$a.u. (see Section 4.4). Then the velocity of each particle is shifted by the gas jet velocity in x-direction and we calculate the resulting momentum x-component as

$$p_x = \left(\frac{p_{x,0}}{m} + v_{\text{jet}}\right) m. \tag{3.3.2}$$

Now that we have a momentum distribution, we can choose a charge state Q for the particles, the electric potential U and acceleration distance a and calculate the TOF for each particle according to Equation (3.1.2) and positions according to Equation (3.1.14).
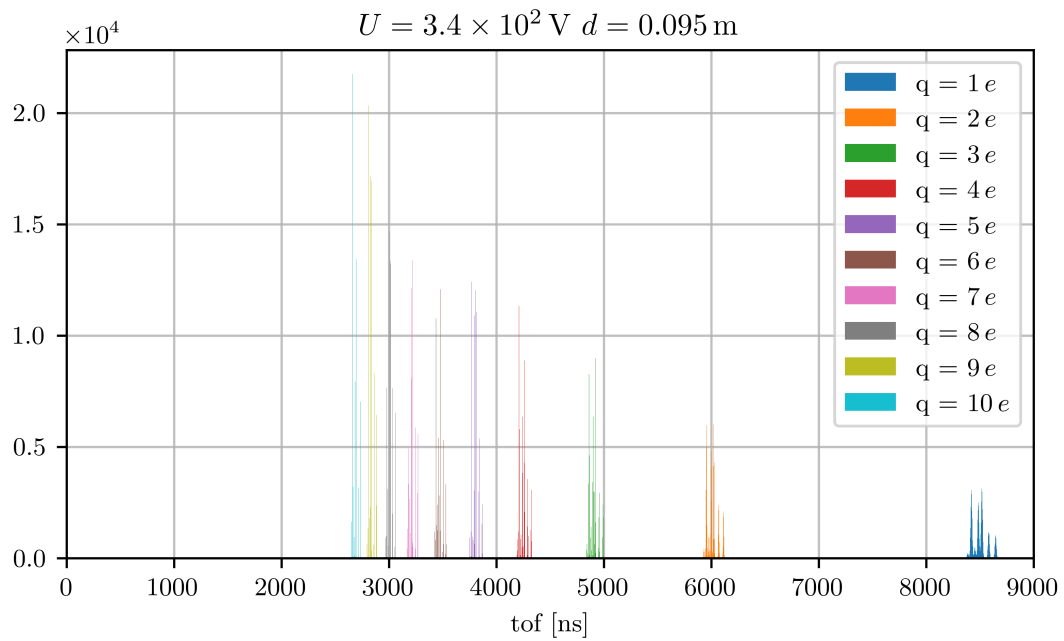
Figure 3.3.2: Distribution of TOF values for Xe isotopes in charge states up to Xe^{10+}. Each charge state has the same amount of samples and identical momentum distribution. However, as the relative momentum resolution increases with TOF, counts at shorter TOF pile up higher in a distribution with less width.

In Figure 3.3.2 we see the TOF distributions for Xe^{n+} monomers of different charge states. The influence of the jet velocity v_{jet} can be seen in the x-position vs. TOF histogram of different charge states Xe^{n+} for n up to 10 in Figure 3.3.3.
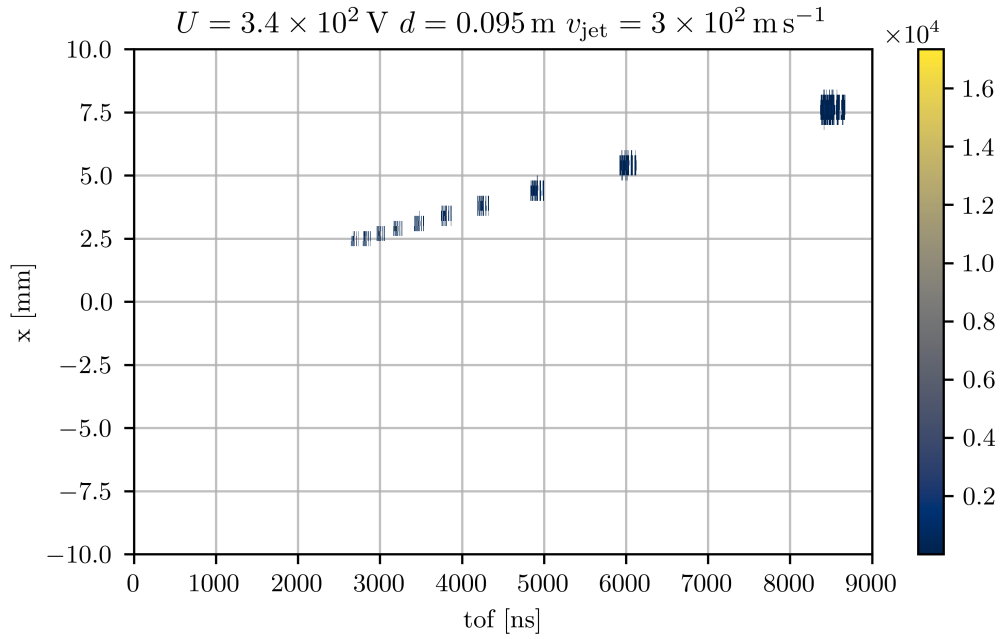

Figure 3.3.3: Distribution of TOF values for Xe isotopes in charge states up to Xe^{10+} together with the x-position where they hit the detector. The postion increases linearly with time, as the ions all start with the velocity of the SGJ on average.

3.3.3   From Coulomb Explosion to Detector Image

In order to reproduce Coulomb explosion data in a simple way we start with a fixed amount of KER in the rest frame of a dimer. We can calculate the absolute momentum of each of the particles from the mass of the particles

$$p_0 = \sqrt{\frac{2 \cdot \text{KER}}{\frac{1}{m_1} + \frac{1}{m_2}}} \tag{3.3.3}$$

and assign randomly a uniformly distributed direction to the first momentum vector

$$p_{1,x} = p_0 \sin(\theta) \cos(\varphi) \tag{3.3.4}$$

$$p_{1,y} = p_0 \sin(\theta) \sin(\varphi) \tag{3.3.5}$$

$$p_{1,z} = p_0 \cos(\theta) \tag{3.3.6}$$

where $\cos(\theta) \propto [-1, 1)$ and $\varphi \propto [0, 2\pi)$. As we are in the rest frame, we get from momentum conservation simply $\vec{p}_2 = -\vec{p}_1$. To introduce again the experimental resolution we take the momentum distribution of dimers we calculated in Section 3.3.2 and add the velocity from there to both of the ions to get the momenta in the lab frame

$$\vec{p}_{i,L} = \vec{p}_i + m_i \frac{\vec{p}_{d,L}}{M}, \tag{3.3.7}$$

where $\vec{p}_{d,L}$ is the momentum of the target dimer in the lab frame and $M = m_1 + m_2$ is the mass of the dimer. From here we can calculate the detector hits as before in Section 3.3.2. In Figure 3.3.4 we see a simulated distribution of ion hits from the Xe^{1+} / Xe^{2+} fragmentation. It shows the typical ring-like pattern, that arises from projection of the momentum vectors from a sphere onto a two-dimensional plane. As we are still considering the isotope distribution, we can now see in Figure 3.3.5 how we expect coincident data to look like in the correlated TOF spectrum. We see that for some mass combinations the contours lie on top of each other and only differ by the extend in diagonal direction. This means we will not be able to distinguish those combinations on the basis of their TOF values and values that are derived from those: the p_z components and the p_z component of the momentum sum.
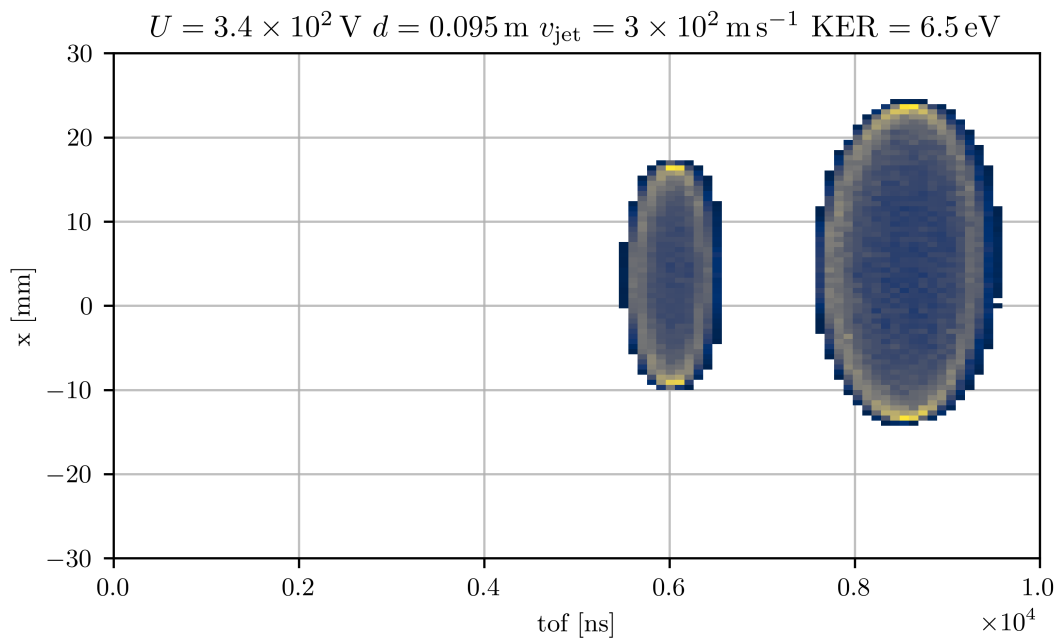
Figure 3.3.4: Histogram of the x-position and TOF spectrum from CE of different isotope combinations in the Xe^{1+} / Xe^{2+} channel. The rings represent the two charge states of Xe^{1+} and Xe^{2+} with all of the possible isotopes. However, in this position projection, we can no longer resolve the isotope momenta.
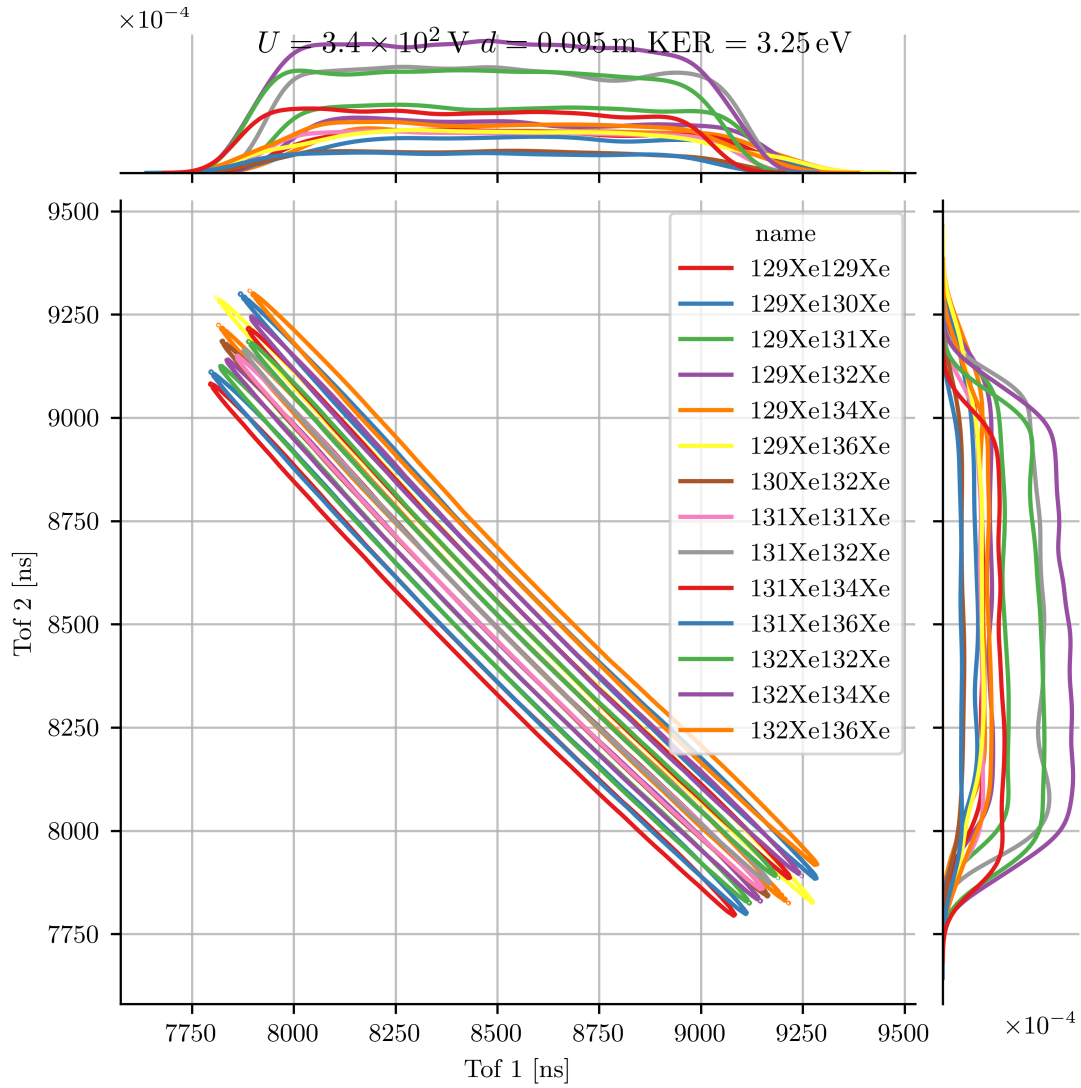
Figure 3.3.5: Contour plot of the correlated TOF spectrum from CE of different isotope combinations in the Xe^{1+} / Xe^{1+} channel.

3.3.4 Reaction Channel Selection by the Momentum Sum

In order to understand how we select data according to conservation of the momentum sum, we will reproduce this momentum sum metric from our simulated data. We take here the random sample of Xe^{1+} / Xe^{2+} Coulomb explosions from Section 3.3.3 as seen in Figures 3.3.4 and 3.3.5 with the isotope combinations as described in Section 3.3.1. But now we calculate back to momentum space, assuming a specific combination of isotope masses. The combination $^{129}Xe^{1+}$ / $^{129}Xe^{2+}$ is particularly interesting, as it has rather high abundance while at the same time its mass sum is almost free from other combinations. In comparison we will consider the combination $^{131}Xe^{1+}$ / $^{132}Xe^{2+}$, which is close to the average mass of dimers. Looking at the z-component of the momentum sum in dependence
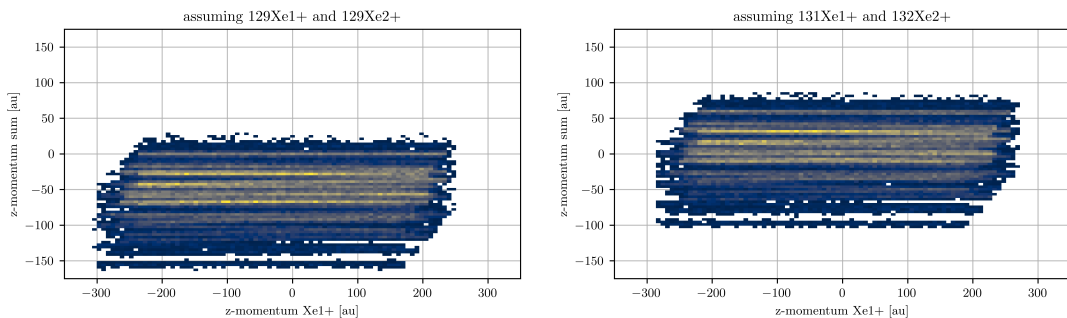
Figure 3.3.6: Distribution of the calculated momentum sum z-component. The distribution includes events from all isotopes of Xe according to their natural abundance. The momenta are calculated based on the assumed mass of Xe^{1+} / Xe^{2+} in the left panel and $^{131}Xe^{1+}$ / $^{132}Xe^{2+}$ in the right panel.

of the Xe^{1+} z-momentum in Figure 3.3.6, we can see a clear horizontal line. As expected, this shows the constant value of the momentum sum broadened by the random thermal momentum of the target. At negative values of the momentum sum we can see a forest of different lines, some horizontal, some tilted. Those lines correspond to events, where we sampled different isotopes but falsely assumed now the combination $^{129}Xe^{1+}$ / $^{129}Xe^{2+}$ in the momentum calculation. With the alternative assumption, the overall distribution is centered around the expected value, but it is hard to make out if the line of zero momentum sum is useful to filter the events. To see how well that works, we apply now a condition on p_z to be small and compare how the momentum distribution in our simulated coincidence sample changes. Starting from a 25 % systematic error in the longitudinal momenta due
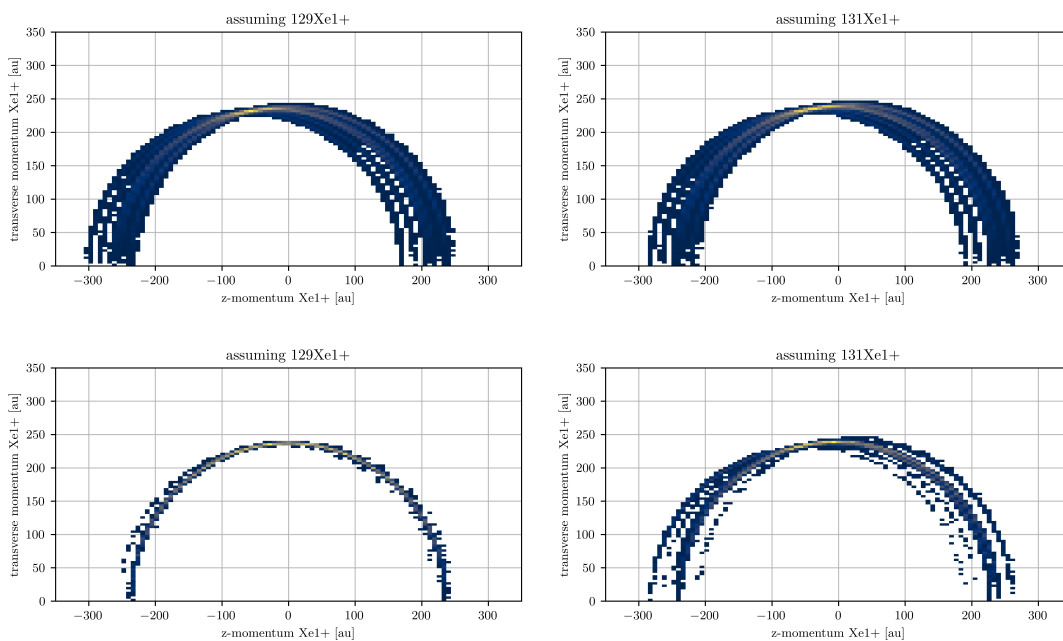
Figure 3.3.7: Randomly sampled Xe^{1+} / Xe^{2+} as in Figure 3.3.6. Here the panels show the relation between the transversal momentum and the longitudinal z-momentum. The top panels show all data, the lower panels restrict the data to $|p_{\mathrm{sum,z}}| < 4$ a.u.. The left panels assume the $^{129}Xe^{1+}$ / $^{129}Xe^{2+}$ channel, the right panels assume $^{131}Xe^{1+}$ / $^{132}Xe^{2+}$.

to the assumed incorrect masses without momentum sum condition, we improve slightly to roughly $10\,\%$ with the $^{131}\mathrm{Xe}^{1+}$ / $^{132}\mathrm{Xe}^{2+}$ channel and get rid of most false coincidences for $^{129}\mathrm{Xe}^{1+}$ / $^{129}\mathrm{Xe}^{2+}$, see Figure 3.3.7. In Figure 3.3.8 we see the
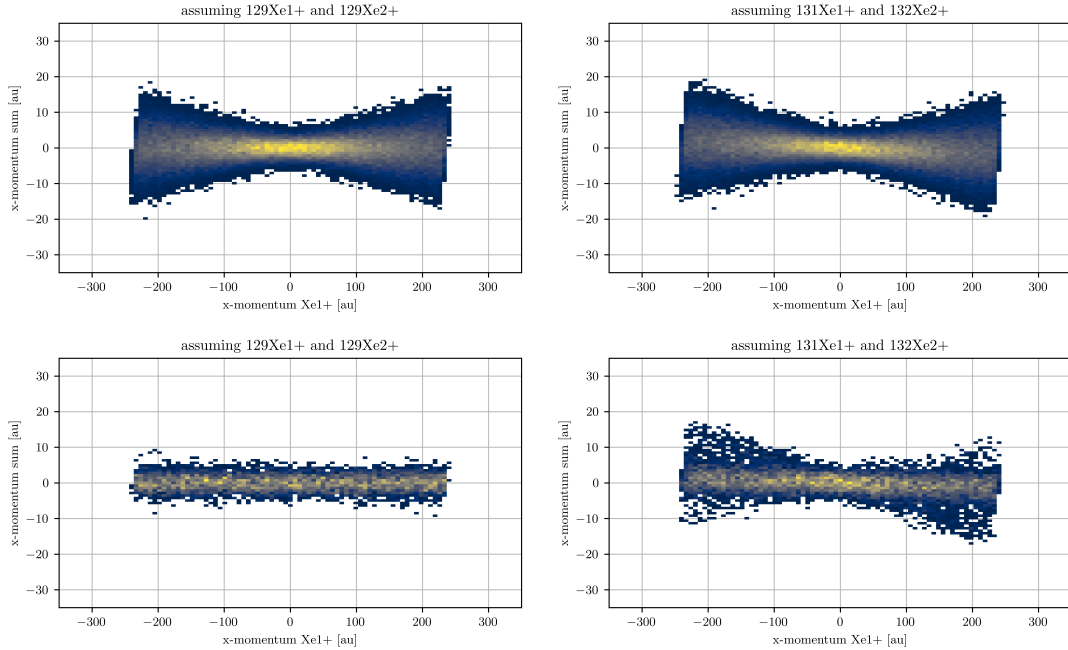
Figure 3.3.8: The same events as in Figure 3.3.7, but instead of the momenta of Xe^{1+}, the figure compares how the x-component of the momentum sum is affected by the condition $|p_{\mathrm{sum,z}}| < 4\,\mathrm{a.u.}$.

momentum sum variation for the x-component. As the hit position in transverse direction depends only on the product of transverse velocity and the TOF, different isotopes will all come to the same position when there is no relative momentum in that component. This makes the transverse momentum sum much less powerful in comparison with the longitudinal momentum sum, which can help us even when it is zero. We can see however, that it still can help to restrict the transverse momentum sums when we compare between the distribution of all events and those that are conditioned by the longitudinal momentum sum.

3.3.5   Stochastic Optimization of Momentum Calibration

Now that we have developed basic understanding of the measured distributions and procedures to transform from detector hits to momenta and vice versa in the previous Sections 3.3.1 to 3.3.4, we can use experimental data and vary the parameters of momentum calculation in order to find optimal values. The main task here is to define useful metrics on how to rate the quality of the calibration. To simplify this, we firstly start from already roughly calibrated data. By that we mean, that charge states and coincidence channels are already identified so far, that momentum sums become visible and useful so far that they distinguish different reaction channels. The energy and momentum distributions are in the right order of magnitude, but not yet with good resolution and e.g. there are systematic errors of the calculated momenta depending on the angle of emission. Starting from there we break down the problem down into four steps.

Before we actually go to momentum data, we have to check first, that the acquired data is correctly matched to the burst pattern of the FEL. To do this, we make use of an detector artifact, that arises from scattered FEL photons hitting the MCP shortly after the pulse hits the gas jet. There are usually multiple peaks in the TOF for photons, but the first one is usually corresponding to the direct path from the beam to the MCP and is therefore perfectly synchronized. We now measure the average arrival time for each burst position in the pulse and can find an overall offset in timing from measurement to measurement and additionally an drift of this timing over the pulse train when the assumed burst rate is not matching the actual burst rate, see Reference [24]. Figure 3.3.9 shows the arrival time of the photons from the following pulse for each but the last pulse. In this TOF window we take the 20th percentile of the selected distribution as the rise time t_{rise}. Then we can do a simple linear regression on

$$t_{\mathrm{rise}} = t_0 + \Delta T \cdot i, \tag{3.3.8}$$

where t_0 is the timing of one selected reference measurement, i is counting the pulses over the burst pattern and ΔT is the mismatch between the assumed and the actual period of the burst.

Now we will go towards the momentum calibration. In order to take results from step to step, we use a Markov Chain Monte Carlo (MCMC) method to not
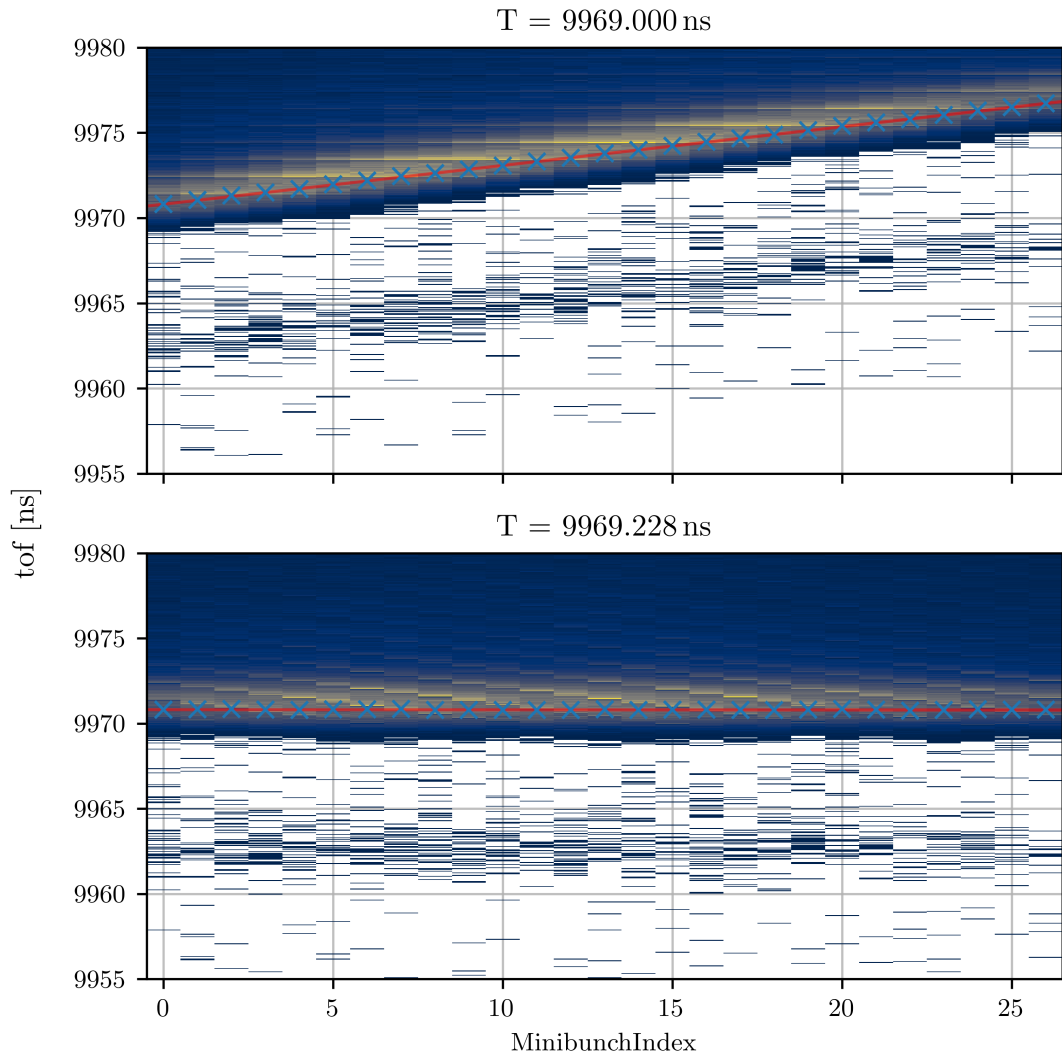
Figure 3.3.9: Arrival time on the ion detector of photons the following pulse for each but the last pulse. Top panel: The period between two pulses is chosen too small. Bottom panel: The period was adjusted by the regression result and the measured arrival time is stable.

only get optimal values of the parameters, but also an accurate estimate of the confidence intervals. The method is originating from Bayes' theorem

$$\text{Posterior}\,(\theta|M, D) = \frac{\text{Likelihood}\,(D|M, \theta)\,\text{Prior}\,(\theta)}{\text{Evidence}\,(D|M)}, \qquad (3.3.9)$$

where θ represents all parameters of the model M, D represents the recorded data. Prior(θ) is a normalised distribution representing our knowledge about the parameters, Likelihood($D|M,\theta$) is the conditional probability to measure the data, given a specific set of parameters and the model. The Evidence($D|M$) normalizes the posterior distribution and only plays a role when comparing different models, as it represents the probability to measure the specific data set given the model. We use the Python package "emcee"[1] for implementation [48]. This method allows us to define three different models of increasing complexity and carry on the results from the simpler model to next the more complex step. With this we are able to narrow down the calibration step by step.

The first model considers only the average TOF of selected ^{129}Xe charge states and does a linear regression on the mass-to-charge ratio:

$$\text{tof}_i = t_0 + C_s\sqrt{\frac{m}{q_i}}, \qquad (3.3.10)$$

where m is the ^{129}Xe mass, q_i the ion charge and C_s a scale constant. Each value is weighted by $\frac{1}{\text{Var}(tof_i)}$. As prior distributions we use a Gaussian around zero for t_0 and a χ^2 distribution for C_s since we know it must be positive. The prior distributions are chosen sufficiently broad so that the position of the posterior is mainly determined by the data. The prior should only give preference to the rough order of magnitude and suppress "nonphysical" solutions, such as negative magnitudes or arbitrary large accelerations that can not be generated by the electric field. Figure 3.3.10 shows the predicted relation between TOF and the ratio $\sqrt{\frac{m}{q}}$ and a comparison between prior and posterior for t_0 and C_s can be seen in Figure 3.3.11.

---

[1]available at `https://github.com/dfm/emcee`
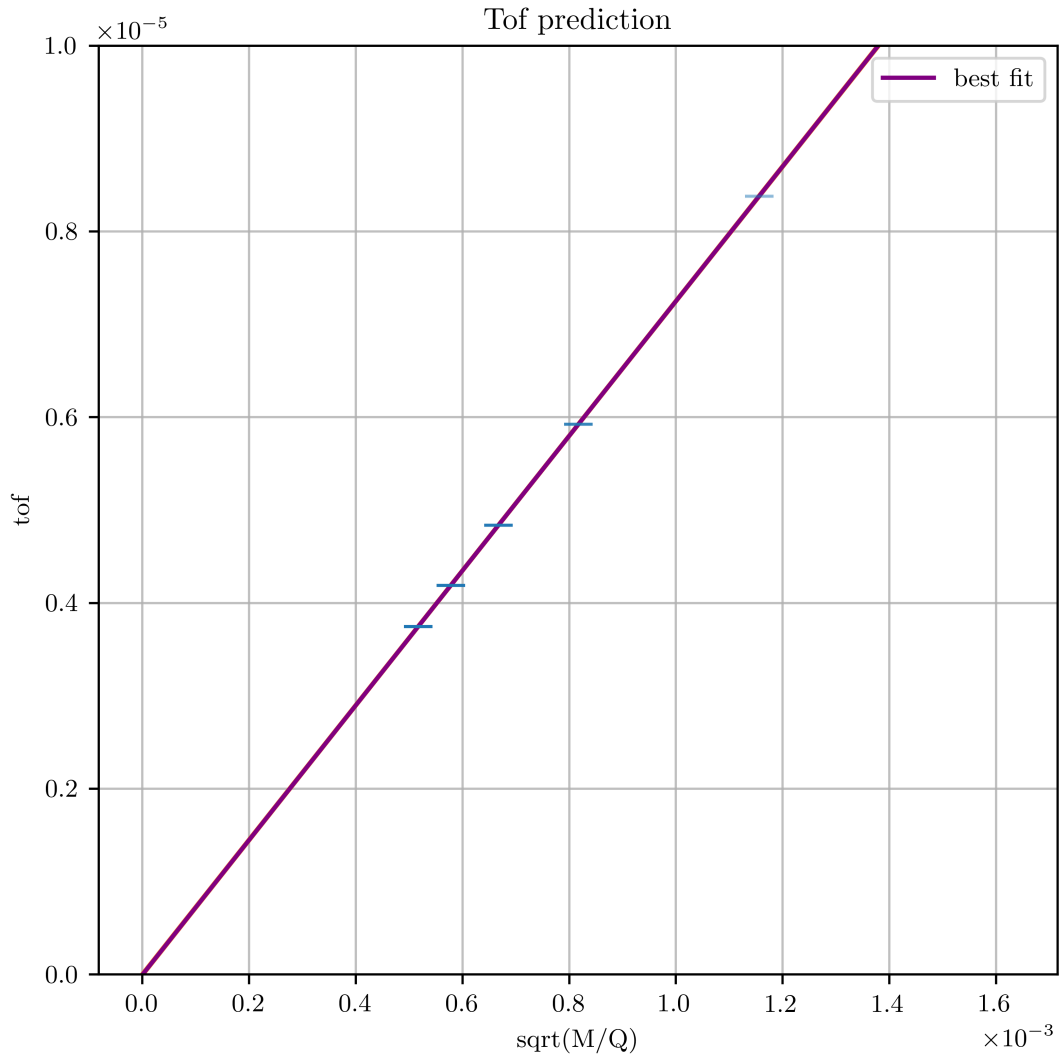
Figure 3.3.10: Predicted relation between TOF and the $\sqrt{M/Q}$ ratio. The experimental data from Xe^{n+} for n in [1, 5] is represented by blue error bars. The error bars represent the standard deviation, however it is not visible here, due to the sharp peaks of the TOFs. The transparency of error bars is proportional to their statistical weight as determined by the total amount of events compared to the other charge states. Both TOF and $\sqrt{M/Q}$ are given in SI base units.
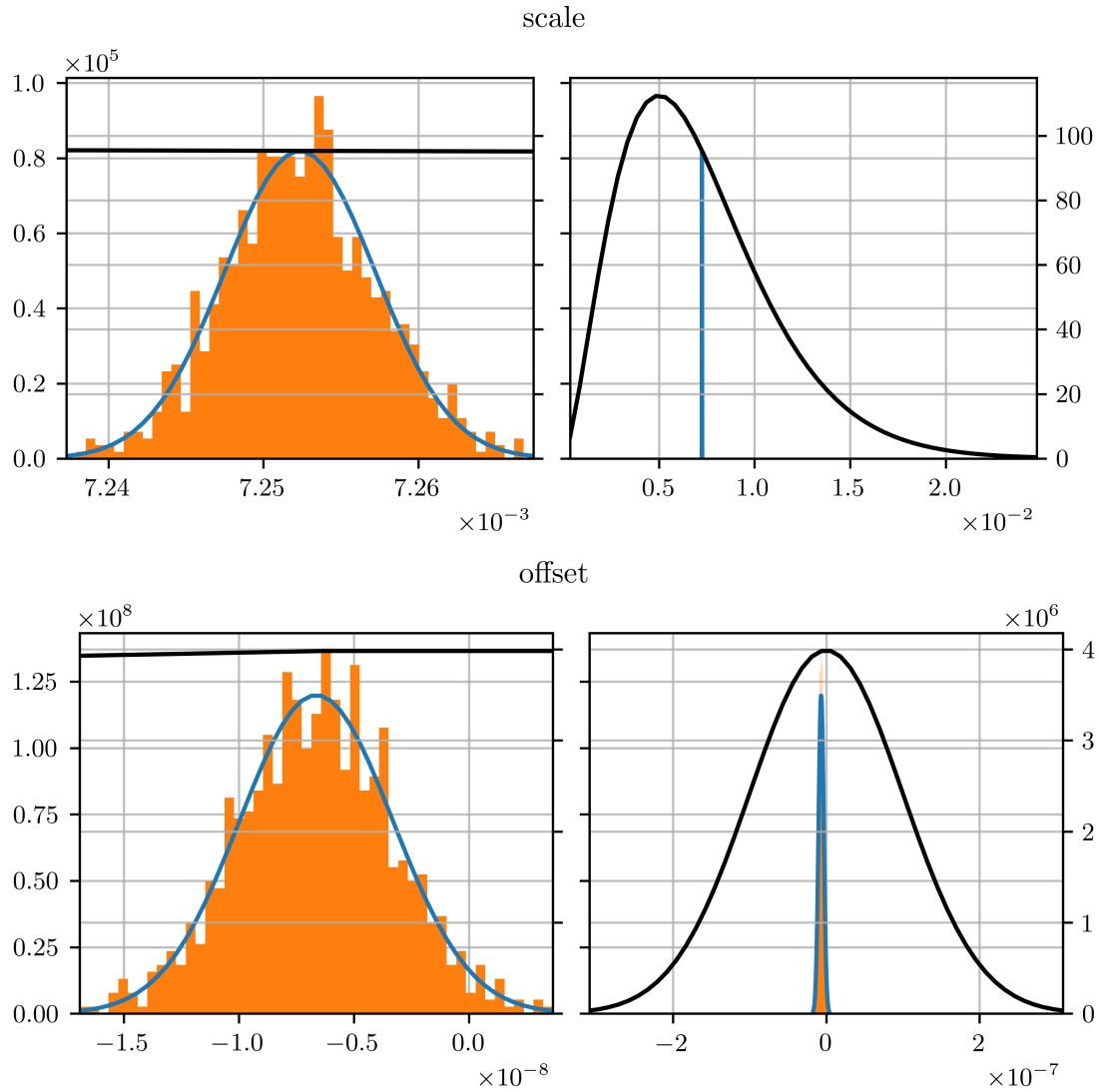
Figure 3.3.11: Comparison between prior and posterior of the TOF model based on Equation (3.3.10). For each of the two parameters, scale (C_s) and offset (t_0), the assumed prior distribution is shown as a black curve, the distribution of the Markov Chain Monte Carlo ensemble is shown as orange histogram and approximated by a Gaussian distribution, which is shown as a blue line.

The second model uses again the selected ^{129}Xe charge states but now looks at the relation between the measured positions and the TOF. We can use Equation (3.1.14) as a linear regression model for this, where we take the substitutions in Equations (3.1.15) to (3.1.18) into account. We can check if the hit position of monomer fragments is proportional to the TOF. When the calculation of detector hits is not calibrated such, that it matches the coordinate system, the flow velocity vector of the SGJ $\vec{v}_{\text{jet}}$ will have a non-zero component in y-direction. But this tells us directly the miss-match in the detector rotation angle θ_0. We also do not know exactly where the SGJ and the FEL cross each other, which is again important to calculate the transverse velocity correctly. Luckily, when we measure ions with different TOF values, we effectively measure the same velocity multiple times and can infer the point of origin (x_0, y_0). In principle, the proportionality factor for calculation of the positions is also not known, but we will not yet vary it here. As this model deals only with the transverse velocity, the accelerated motion due to the electric field is irrelevant in contrast to the previous model. Still the pure TOF model gives as a better estimate of the time zero t_0 and we approximate the posterior result from the TOF model with a Gaussian and use it as prior information in this model. The other priors are again broad Gaussians around zero for φ_0, x_0 and y_0 and a χ^2 distribution for the absolute value of v_{jet}. The posterior sample and predicted relations between position and TOF can be seen in Figure 3.3.12
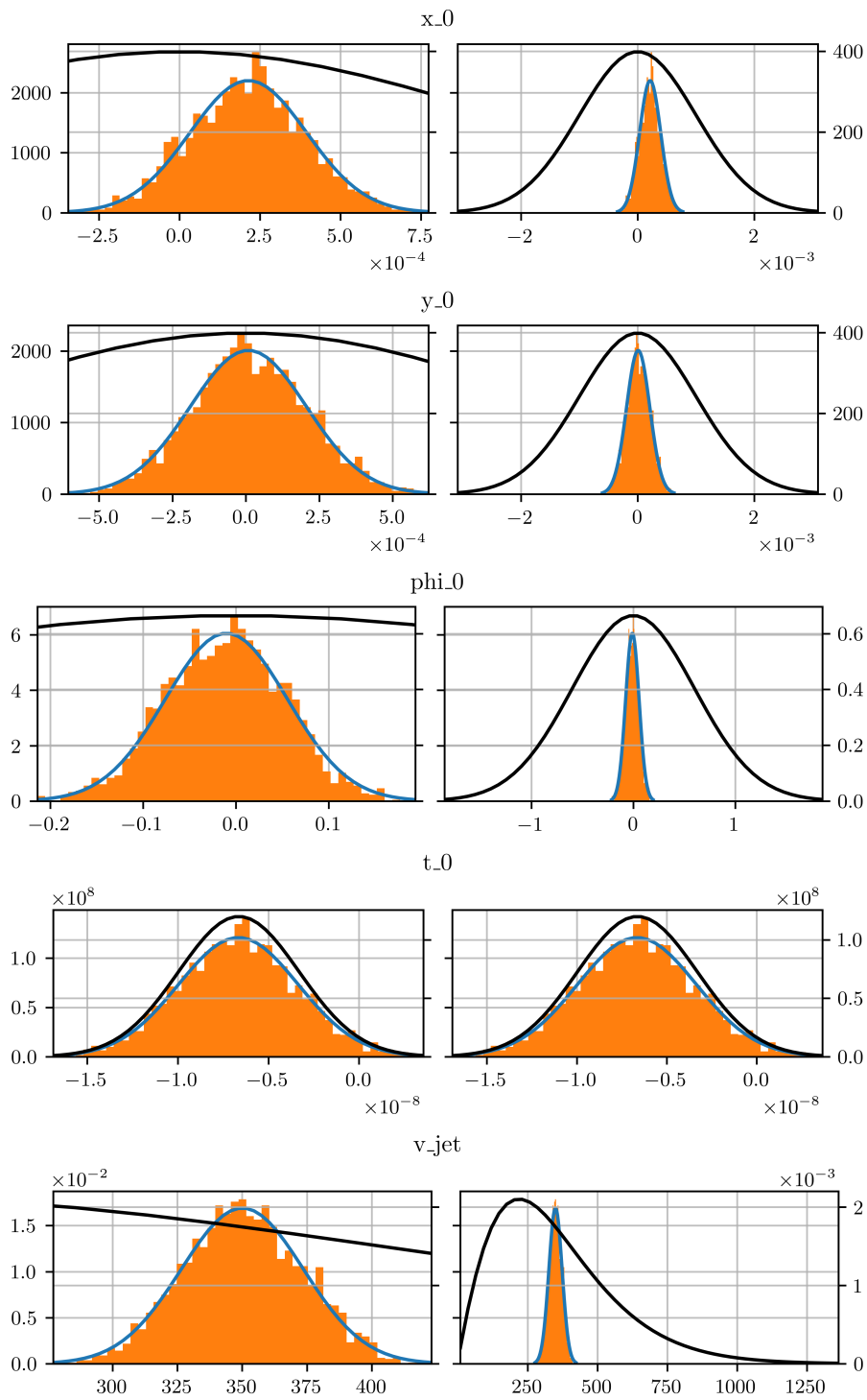
Figure 3.3.12: Comparison between prior and posterior distributions as in Figure 3.3.11, but for the force free position versus TOF model. The estimated parameters are the offset substitutions given by Equations (3.1.15) to (3.1.18) and the jet velocity. All values are given in SI base units.
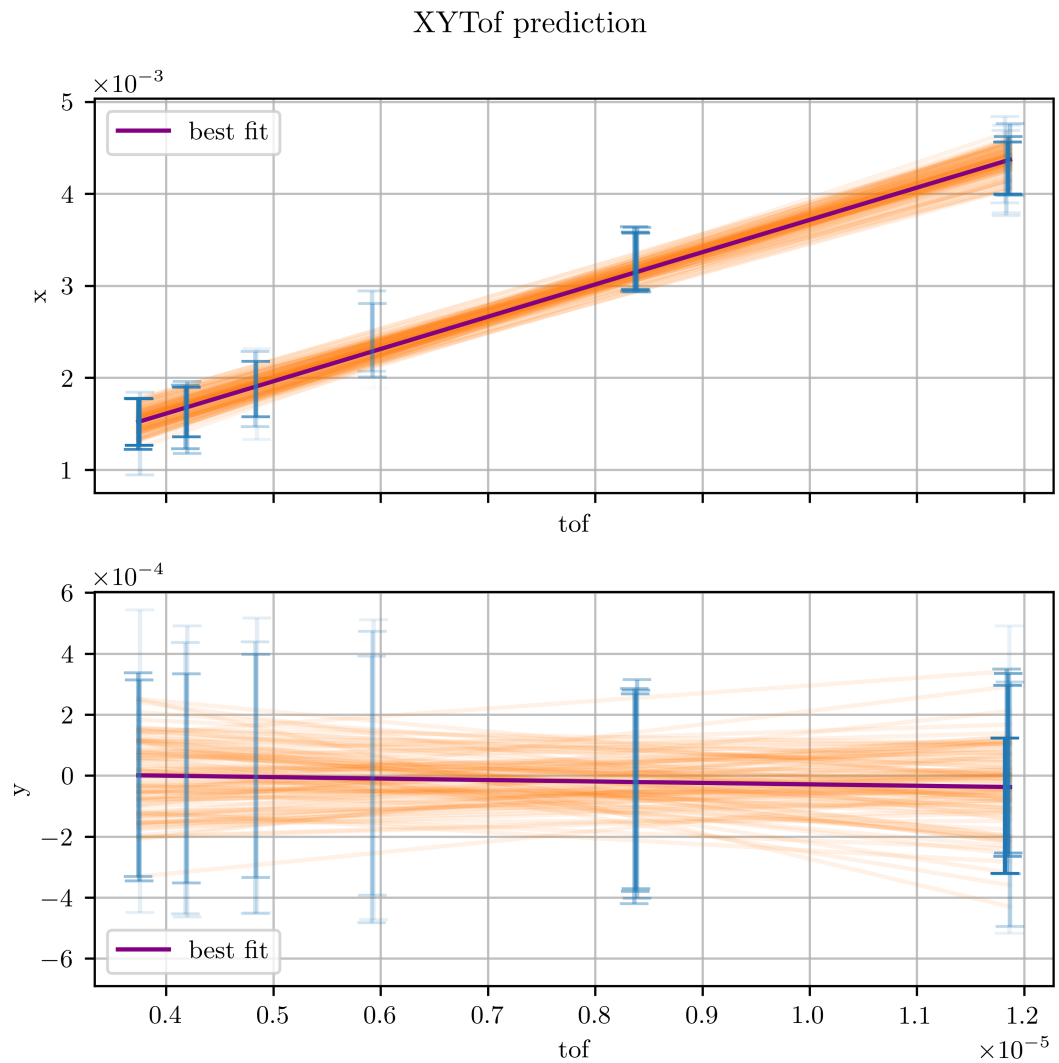
Figure 3.3.13: Predicted relation between x and y position to the TOF. The experimental data from Xe^{n+} for n in [1, 5] and stable $Xe^{...}Xe^{+}$ ions is represented by blue error bars. The error bars represent the standard deviation, however it is not visible here, due to the sharp peaks of the TOFs. The transparency of error bars is proportional to their statistical weight as determined by the total amount of events compared to the other charge states. Multiple error bars at one charge state correspond to the different isotopes of Xe. Both positions and TOF are given in SI base units.

The third model includes now all parameters, that we want to tune for the momentum calibration. So in addition to the parameters in the previous model, we will also vary the acceleration distance through the homogeneous electric field d, the electric field strength in that section E, the TOF offset correction for the in-homogeneous part of the spectrometer δ, the scaling factors for the positions s_x and s_y. From these 10 parameters and the measured data set in position and TOF space we calculate momentum distributions in each iteration. Additionally to these ten calibration parameters, we also use the target temperature T to define the thermal distribution in the frame of reference of the SGJ. The thermal distributions will not actually be resolved for the Xe experiment. But as it is just Gaussian in each momentum component, it will reflect the average momentum resolution instead.

To find a sufficiently good metric for this model is difficult, so we rely on a combination of multiple metrics. Those metrics try to reflect the observations that are usually used to manually tweak the momentum calculation. First, we now want to calibrate the momenta further away from the zero momentum case that is covered by the monomer ions. So we now make use one of the coincidence channels, the $^{129}\mathrm{Xe}^{1+}$ / $^{129}\mathrm{Xe}^{2+}$ channel. That channel shows only one dominant peak in KER and as the dimers are randomly oriented, the angular distribution of momenta should be uniform. We can define the following five metrics for this specifc channel:

1. The momentum sum vector is given by a thermal distribution around $\vec{0}$ with temperature T.

2. The KER does not vary with the spherical angles φ and θ.

3. The width of the KER distribution should be minimal for optimal resolution.

4. Each component of the momentum vectors should have similar distributions.

5. The average KER should be close to the expected value.

Additionally to that we keep looking at the monomer data from before. But in contrast to the two previous models now with the metric, that their momentum vector should also be from the thermal distribution around $\vec{0}$ with the temperature T as for the momentum sum of the coincidence channel. The metrics for those points are shown in Appendix A.

As before we now use results from the previous 5D model as prior information. The results for x_0, y_0, t_0, v_{jet} and φ_0 are approximated by independent Gaussian distributions and significantly reduce the parameter volume that needs to be explored now. The prior for electric potential is given by a χ^2 distribution around the applied voltage from the power supply U with 10% standard deviation. The distance is also taken as a χ^2 distribution around the design value of $11\,\text{cm}$ with again 10% width. The value for δ is estimated by comparing the calculated TOF of $^{129}\text{Xe}^{1+}$ with the measured TOF, however we take for that estimate an increased potential of $1.6U$ in order to take into account the increasing field strength at the MCP. We then take a χ^2 distribution around the estimate value with an 50% standard deviation as we only want to consider this as a rough estimate. For the priors of the spatial coordinates scales s_x and s_y we chose rather narrow χ^2 distributions around 1 with an standard deviation of 20%, as the observed detector diameter should not differ significantly from the MCP diameter. Figure 3.3.14 shows, how we can finally narrow down all of the calibration parameters to small confidence intervals.

To come to final values, we do this procedure for all measurement runs and then use a weighted average of the parameters for each set of measurements, that share identical settings of the spectrometer and detector voltages. Timing instabilities of the data acquisition or the arrival time of the FEL are compensated by referencing each measurement to its arrival time of photons, see Figure 3.3.9.
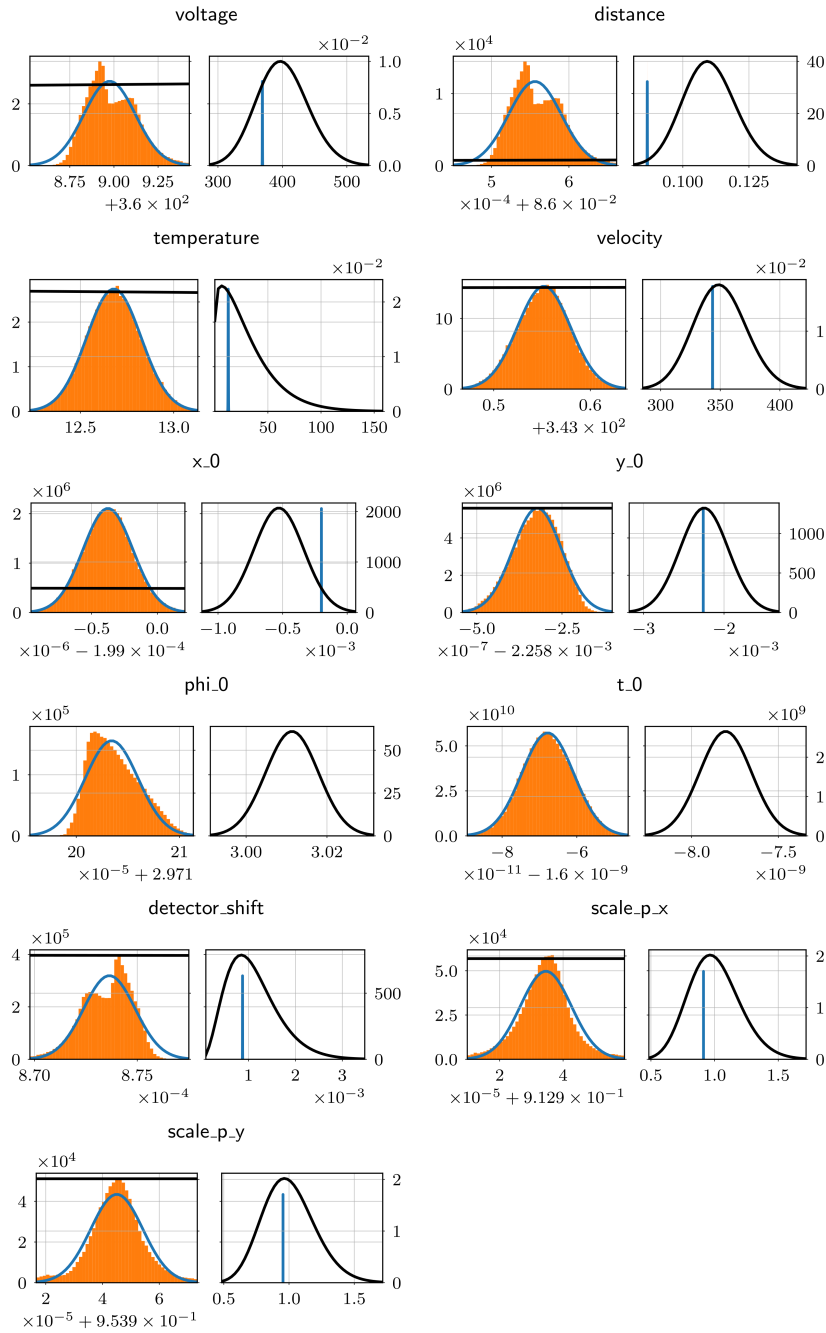
Figure 3.3.14: Comparison between prior and posterior distributions as in Figures 3.3.11 and 3.3.12, but for the full model of momentum calculation in the remi analysis. The estimated parameters in addition to those in Figure 3.3.12 are mainly the parameters for calculation of the longitudinal momentum: distance (d), voltage (U), detector shift (δ). Also estimated is the detector linearity errors for positions s_x and s_y and the width of the momentum sum in terms of temperature. All values are given in SI base units.

3.3.6   Molecular Dynamics Simulation of a Pump-Probe Measurement including Transfer Processes

In order to validate interpretations of experimental data qualitatively we will use a classical molecular dynamics simulation. For simplicity, we will stick to only the ^{129}Xe isotope and we will directly use the simulated momenta as result and not consider also the simulation of detection in the REMI. Instead of programming a complete simulation from scratch, we use the Julia package "Molly.jl"[2] [49]. Molly.jl offers a straightforward programmatic interface to define molecular systems (or in general, systems of interacting entities) and ships with typical interaction potentials such as Coulomb, Lennard-Jones (LJ) or Buckingham potentials. From the provided integration schemes we will use the "VelocityVerlet" integrator. As full treatment of the Xe system with its large amount of electrons is hard, we will stick to simulating only the trajectories of atoms and ions with Coulomb and LJ pairwise interactions. As LJ parameters we use the values given in reference [50] for the neutral ground state and try to roughly mimic the potential of charged dimers as seen in reference [17]. We use the position of the potential minimum as it is shown there, but still vary the depth of the potential ϵ as we do not distinguish all of the sub-states and do not know the correct average potential and also will not distinguish different charge states for the LJ interaction and assume that this is not crucial to get a qualitative picture. The LJ parameters are listed in Table 3.2. The resulting potential curves are shown in Figure 3.3.15. On top of

	$\sigma/2^{1/6}$ / Å	ϵ / eV
both neutral	4.42	0.0227
neutral/charged	3.6	0.1
both charged	2.9	0.44

Table 3.2: LJ parameters for combinations of neutral and charged parameters. The two body interaction parameters are calculated by the geometric mean of single particle parameters.

those interactions for the forces on the particles we extend the package by a charge transfer interaction and a ETMD(3) interaction. The rate of CT is calculated as

---

[2]available at `https://github.com/JuliaMolSim/Molly.jl`
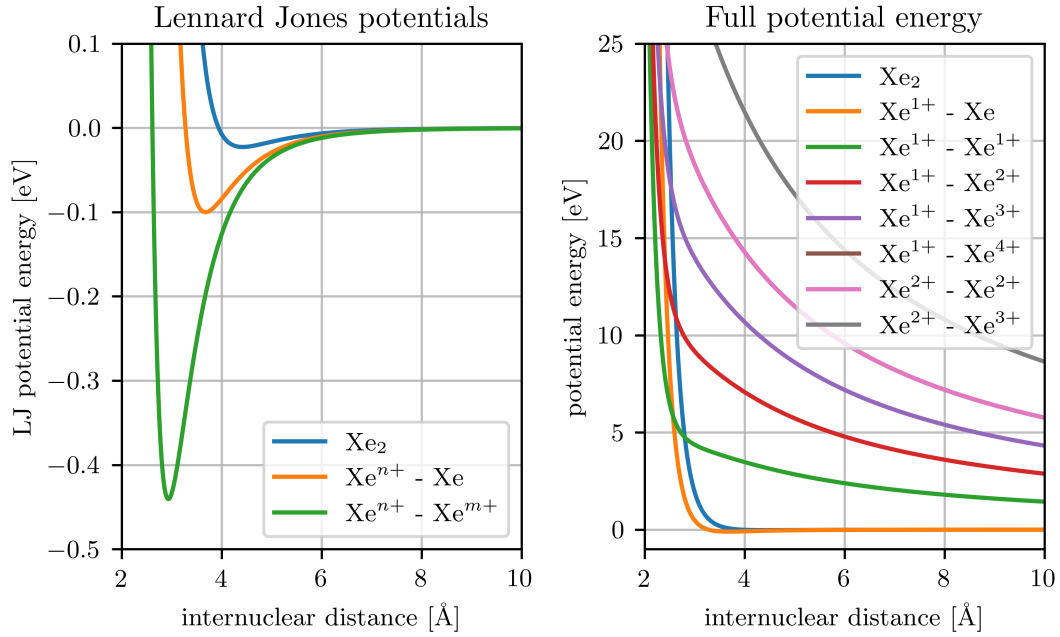
Figure 3.3.15: Potential energy curves for the MD simulation. Left: only LJ part, Right: Full potential energy.

the product of the s-type orbital overlap integral and an empiric constant:

$$\Gamma_{CT}\left(r_{i,j}\right) = A \exp\left(-\frac{r_{i,j}}{r_s}\right)\left(1 + \frac{r_{i,j}}{r_s} + \frac{r_{i,j}^2}{3r_s^2}\right), \text{where} \tag{3.3.11}$$

$$r_s = \frac{r_c}{8} \text{ and } r_c = \frac{2\sqrt{Q_iQ_j} + Q_j}{4\pi\varepsilon_0 \text{IP}_j} \tag{3.3.12}$$

is the critical distance of the semi-classical Over The Barrier Model (OTBM) [28]. We use the scale distance of $r_c/8$ as this is the point where the overlap factor drops down to $1\,\%$ and charge transfer should stop, see Figures 3.3.16 and 3.3.17. The rate for occurrence of ETMD(3) events is calculated as the product of the CT rate from first to second atom, the $\frac{1}{r_{1,3}^6}$ scaling of ICD with the distance between first and third atom and another empirical factor:

$$\Gamma_{\text{ETMD(3)}} = \frac{B}{r_{1,3}^6}\Gamma_{CT}\left(r_{1,2}\right). \tag{3.3.13}$$

Figure 3.3.16: Dependence of the charge transfer rate on the inter nuclear distance for different combinations of ion charge states. The left axis shows the value of the orbital overlap factor, the right axis shows the rate at which charge transfer occurs. The horizontal dashed line marks the 1 % value of the overlap factor and the curves cross it at their critical distance.
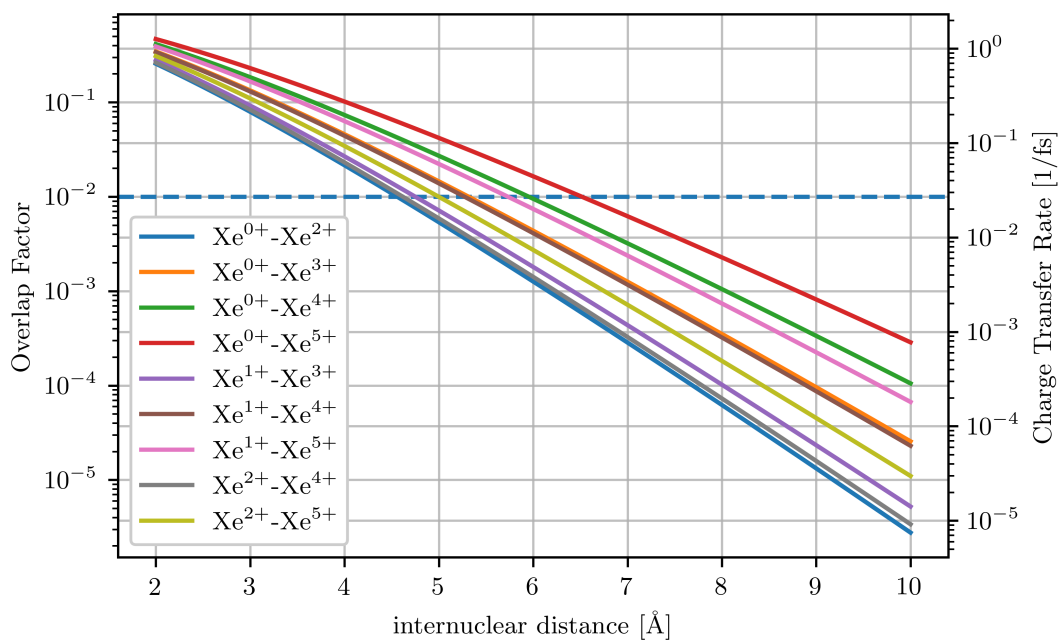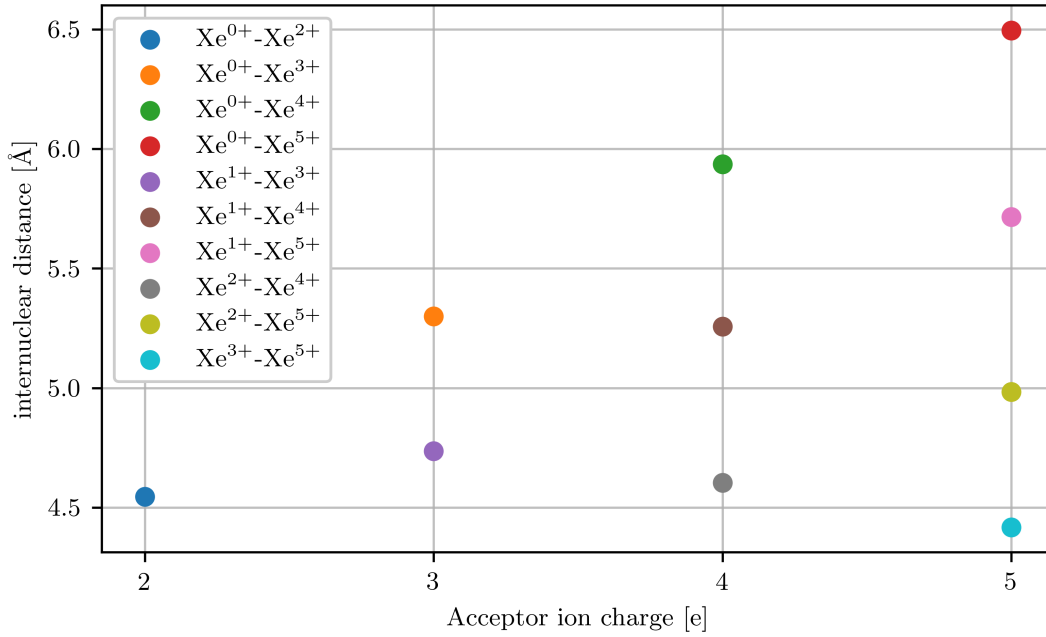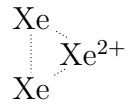
Figure 3.3.17: The critical distance of charge transfer for different combinations of donor and acceptor ion charge states.

In Figure 3.3.18 both the CT and ETMD(3) rates are shown for the $\begin{smallmatrix} \text{Xe} \\ | \\ \text{Xe} \end{smallmatrix}$ Xe^{2+} trimer. We only consider ETMD(3) in this particular charge state.

The simulation is started with N ^{129}Xe particles with given initial charges. The positions are chosen for dimers such that the distance between the particles is drawn randomly from the quantum mechanical ground state, approximated by a Gaussian with mean $\mu = 4.45\,\text{Å}$ and standard deviation $\sigma = 0.12\,\text{Å}$. For dimers, three distances are drawn from the same distribution and the three particles are arranged in a triangle with the respective distances.

In order to simulate pump-probe scans we have to consider the actual time difference between the absorption of two photons. One could, in principle, model this by coupling the system with a varying probability of absorbing photons proportional to the sum of intensities of the pump and the probe pulses. However, we chose to simplify the model in order to precisely choose events where we absorbed exactly two photons. Then we can describe the delay such that we draw in total two time values, t_1 and t_2, from the two pulse envelopes. The relevant result for the pump-probe scheme is the absolute difference $|t_1 - t_2|$ between the
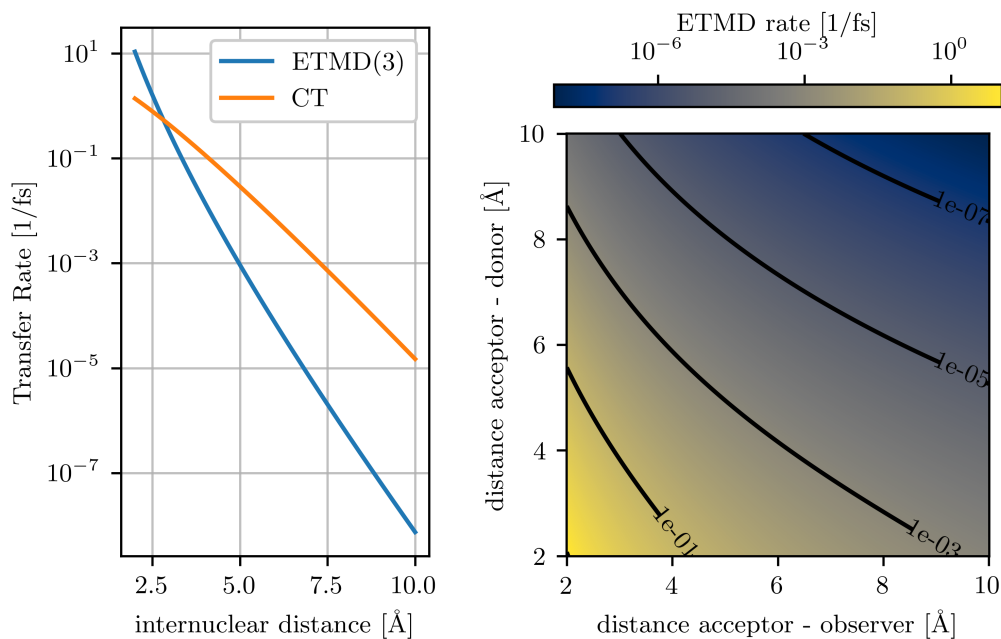
Figure 3.3.18: Left Panel: Rate of occurence for ETMD(3) compared with the rate for CT in Xe_3^{2+} trimers. The trimer is assumed to be in the equidistant triangle configuration. Note that the CT rate is doubled compared to dimers, as there are now two donor ions at the same distance. Right Panel: ETMD(3) rate as function of both distances from the acceptor Xe^{2+} ion to the neutral Xe atoms. For both panels is $A = 2.7\,1/\text{fs}$ and $B = 500$

two times as we assume that all photons have identical polarization and wavelength. We describe the two pulses by the Gaussian distributions

$$P(t_1|\tau_0, \sigma) = \mathcal{N}(0, \sigma) \text{ and} \tag{3.3.14}$$

$$P(t_2|\tau_0, \sigma) = \mathcal{N}(\tau_0, \sigma), \tag{3.3.15}$$

where σ is the photon pulse envelope standard deviation, τ_0 is the desired delay value and $\mathcal{N}(\mu, \sigma)(x) = \exp\left(-\frac{(x-\mu)^2}{2\sigma^2}\right)/\sqrt{2\pi\sigma^2}$. Assuming optimal spatial overlap of the pulses we can distinguish four elementary combinations:

1. Both photons from first pulse.

2. One from first pulse, one from second pulse.

3. One from second pulse, one from first pulse.

4. Both photons from second pulse.

So effectively we get two cases which we describe by

$$P(t_1 - t_2|\tau_0, \sigma) = \frac{1}{2}\left(\mathcal{N}\left(0, \sigma\sqrt{2}\right) + \mathcal{N}\left(\tau_0, \sigma\sqrt{2}\right)\right), \tag{3.3.16}$$

as sums and differences of Gaussian distributed random variables add up their variances, i.e. they add their standard deviations as $\sigma = \sqrt{\sigma_1^2 + \sigma_2^2}$. To get the absolute difference we have to replace each of the Normal distributions with a folded normal distribution where negative values are flipped to positive ones:

$$P(\tau|\tau_0, \sigma) = \frac{1}{2}\left(2\mathcal{N}\left(0, \sigma\sqrt{2}\right) + \mathcal{N}\left(\tau_0, \sigma\sqrt{2}\right) + \mathcal{N}\left(-\tau_0, \sigma\sqrt{2}\right)\right)$$
$$\text{for } \tau >= 0. \tag{3.3.17}$$

With this result, we can draw a random delay value before running each simulation and implement the probe coupling at one specific step in the simulation. Once this step is reached, we increase the charge count of one random atom in the system by 2. To extend Molly.jl with a pump-probe scheme, we implemented this through a custom coupling function. As the Coulomb Potential is a long range potential, it would take very long integration times until we can completely neglect the remaining energy compared to the kinetic energy after a coulomb explosion.

So we run the simulation for a reasonable time span of $5\,\text{ps}$ where the particles gained the majority of the energy, typically around $95\,\%$ to $98\,\%$, and then scale all momenta such that the KER becomes equal to the total energy before scaling but the sum of momenta is still zero.

In summary, the simulation remains effectively with 5 free parameters:

1. the photon pulse length σ

2. the potential depth of the LJ interaction ϵ

3. the empirical rate factor A for CT

4. the empirical multiplier B for ETMD(3)

5. the choice of r_s relative to r_c

We will later adjust the first four to find good qualitative agreement with the measurement. The range scaling r_s was not further varied. This model will give us some qualitative understanding with regard to the orders of magnitude when comparing event rates of the different process, the resulting KERs or the time it takes to accelerate the ions. However as it is purely classical, it will not be able to reproduce quantum mechanical interference in the nuclear part of the wave function. To reproduce those, one needs to propagate the whole dissociation properly in a quantum theory. This was done recently for another system in References [51, 52].

Chapter 4

The Reaction Microscope Beamline at FLASH2

The experimental setup for this work has already been described in previous publications, e.g. [53, 54]. Thus we will focus here on the general overview and discuss the parameters specific to this study. For a detailed description of the experimental setup, refer to [53] as there the state of the beamline corresponds to when the experiments for this project were performed. We will first look at our light source, the Free electron LASer in Hamburg 2 (FLASH2), and how it was set up for the experiment in Section 4.1. Then in Section 4.2, we discuss how the light pulse is split into two delayed pules and focused into the REMI. After that, we will show how the Xenon target is prepared in Section 4.3 and the charged fragments are detected in Section 4.4.

4.1 The Free Electron Laser

The measurements in this work were all done using FLASH2 as a light source during one beamtime in April 2018. Here we will not go into detail about the facility and its capabilities, this can be found in references [55, 56]. The layout of the facility can be seen in Figure 4.1.1. Briefly, FLASH2 provides intense light pulses in the wavelength range from 4 nm to 90 nm, restricted additionally by the simultaneous operation of FLASH1 to the range between 1 and 3 times the wavelength at FLASH1. The accesible range of pulse duration is 10 fs to 200 fs, for pulse energy it is 1 μJ to 500 μJ. However, there is a strong correlation
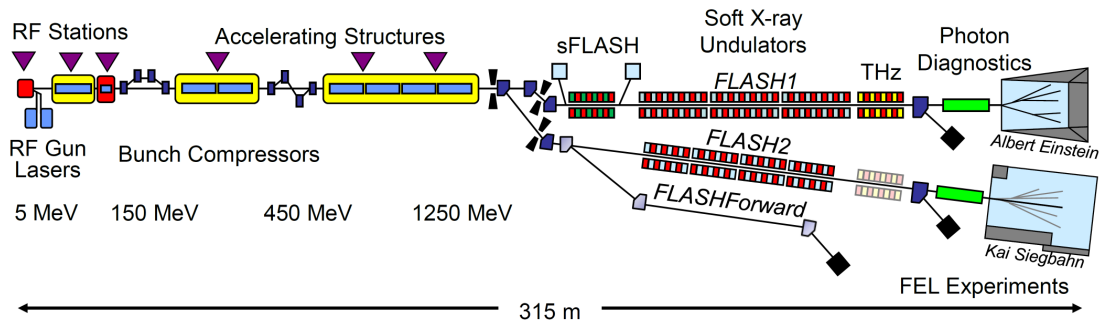
Figure 4.1.1: Layout of the Flash facility. The linear accelerator is shared between Free electron LASer in Hamburg 1 (FLASH1) and FLASH2 and delivers electron bunches with up to 1250 MeV kinetic energy per electron. After accelerating, the beam can be diverted by a fast-switching magnet into the desired beamline. In our case, the beam goes into the FLASH2 section, where the undulators create a photon pulse and afterwards the electron pulse is dumped. In the following section, indicated in green, various diagnostic tools characterize the photon pulse before it comes to the experimental hall "Kai Siegbahn", where the FlashRemi endstation is located. Taken from Rönsch-Schulenburg et al. [56] without change, licensed under CC BY 3.0.

between the achievable wavelength, pulse length and pulse energy, as can be seen in reference [56]. The pulses are provided in a burst mode, such that 10 pulse trains are produced every second, and each pulse train contains pulses with a repetition rate of 1 MHz or fractions of that rate. The maximum train length is 800 µs for both FLASH1 and FLASH2 together with a switching time between both FEL of 50 µs. For REMI experiments, one typically chooses a repetition rate out of 100 kHz, 200 kHz or 250 kHz, where the TOF of the heaviest fragments is the limiting factor. An equal sharing of accelerator time between two beamlines this results in a maximum of 37 to 93 pulses per pulse train, at 100 kHz or 250 kHz burst rate. The average pulse rate is then 370 Hz to 930 Hz, respectively. When FLASH1 is operated only with a single pulse, the maximum number of pulses available for the FlashRemi increases to a range of 74 to 185. An example of the latter pulse pattern at 200 kHz intra-burst rate is shown in Figure 4.1.2.

The data presented here was recorded at a photon energy of roughly 100 eV, or 12.4 nm wavelength, with an average pulse energy in the order of 10 µJ. The FEL was running at a burst rate of 100 kHz, initially 49 pulses but later dropping to 28 due to stability problems with the accelerator. The maximum intensity on the gas target was estimated by [22] from the highest detected charge state of
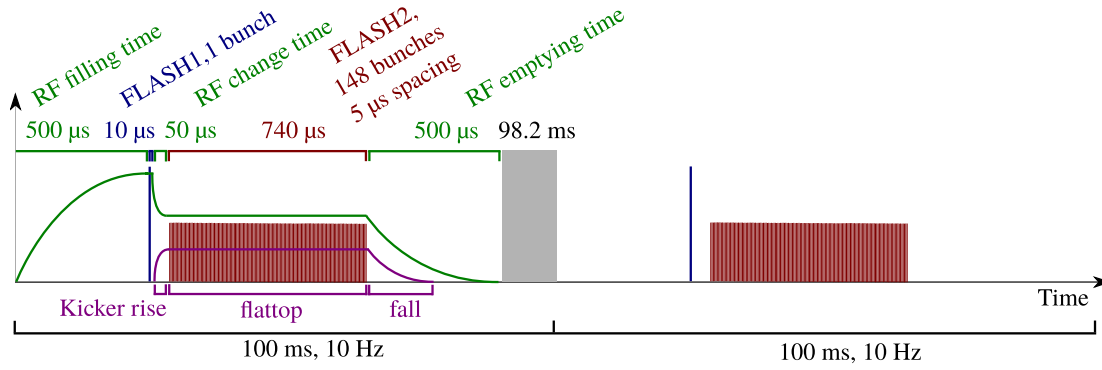
Figure 4.1.2: Accelerator burst mode pattern of FLASH1 and FLASH2. Every 100 ms the radio-frequency cavities are filled with radiation. First, settings are adjusted for FLASH1 and electron pulses are delivered to there. Then, the accelerator settings are adjusted to the parameters for FLASH2 while at the same time, a so-called "Kicker" magnet is enabled for diverting the beam to FLASH2. Once the fields are stable again, pulses are delivered to FLASH2. Image taken from Schmid [22] with permission.

Xe^{15+} to $I \approx 1 \times 10^{15}\,\mathrm{W/cm^2}$ to $2 \times 10^{15}\,\mathrm{W/cm^2}$ in accordance with $10\,\mu\mathrm{J}$ pulse energy, a pulse duration of $T = 50\,\mathrm{fs}$ and a focus diameter of $3\,\mu\mathrm{m}$ (Full Width at Half Maximum (FWHM)). When the beam is split into two equally intense parts, significant amount of intensity is lost. Then only up to Xe^{11+} is detected, which leads to an estimate of $I \approx 5 \times 10^{14}\,\mathrm{W/cm^2}$ for both beams together. The FEL is polarized in the horizontal direction. For our setup, that means the polarization is oriented perpendicular to the REMI electric and magnetic field and along the gas jet flow. The target clusters are not oriented beforehand, so they have a random alignment with respect to the polarization.

4.2 The XUV Optics

The FlashRemi beamline includes a mirror chamber with a set of 3 grazing incidence mirrors. Two of those mirrors are plane mirrors and are mounted together form the split-and-delay unit. The third mirror is an off-axis ellipsoidal mirror which images the source volume of the FEL beam into the reaction volume inside the REMI, see Figure 4.2.1. Design and implementation were done as part of a previous doctoral project [22]. Development of motor controls software, commissioning of the XUV-XUV pump-probe operation and development of procedures to maintain
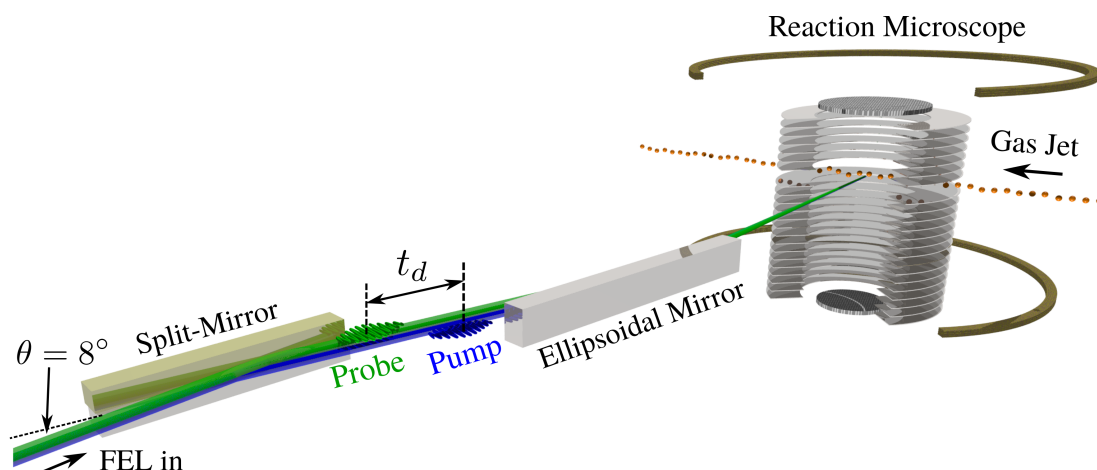
Figure 4.2.1: Design sketch of the XUV split, delay and focus optics. The FEL beam comes from the left and is first split by a pair of plane mirrors where one of them introduces a delay by a spatial path difference. After that, both beams are focused by an ellipsoidal mirror into the reaction microscope. The focus is adjusted such that it is inside the SGJ. Image taken from Schmid [22] with permission.

spatial overlap of the split beams were part of this doctoral project. Sufficient stability of this spatial overlap over long delay ranges up to 2 ps was first achieved in preparation of the Xenon experiment, whose results are discussed in this thesis. The method and further developments of it are described in Section 3.1.3.

Both the split mirror and the ellipsoidal mirror are mounted on a mirror holder that is connected to six linear actuators by stiff connectors with steel ropes as joints. By a coordinated movement, it is possible to translate and rotate the mirror holder in all 6 dimensions. The algorithm to calculate the linear stage positions is given in [22, section 9.4.1]. The absolute limits for translations and rotations by this mechanism are hard to determine, as they are not independent of each other. However, in practice, translations of ± 3 mm and rotations of $0.5°$ are feasible.

In order to control the temporal delay between the two split parts of the FEL pulse, the upper part of the split plane mirror pair is mounted on several linear stages. The positioning is steered by closed-loop controlled piezo motors with high-resolution spatial encoders. It allows translation normal to the mirror surface and rotations around the other two mirror axes, see Figure 4.2.3. The encoder resolution is specified to 4 nm and the repeatability of positioning to ± 60 nm [22, section 9.4.2]. Together with the experimentally determined conversion factor from translation to photon delay of 0.923 fs/µm [22, section 9.6.3] this translates
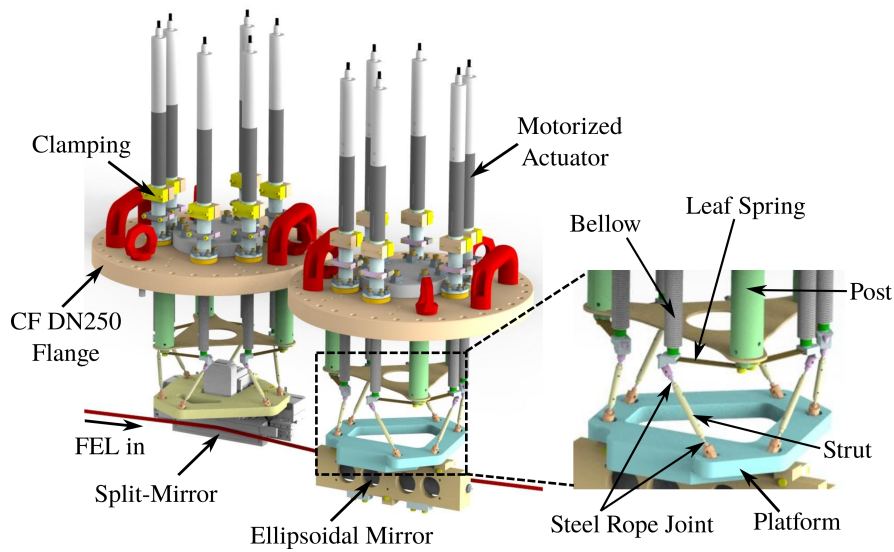
Figure 4.2.2: Annotated CAD drawing of the motorized grazing incidence mirror mounts. The mirror holders can be moved by 6 linear motors each. The parallel linear translation of the 6 motors is converted to translation and rotation in all spatial dimensions by a combination of diagonal struts and steel rope joints. The upper ends are additionally forced by leaf springs. Image taken from Schmid [22] with permission.
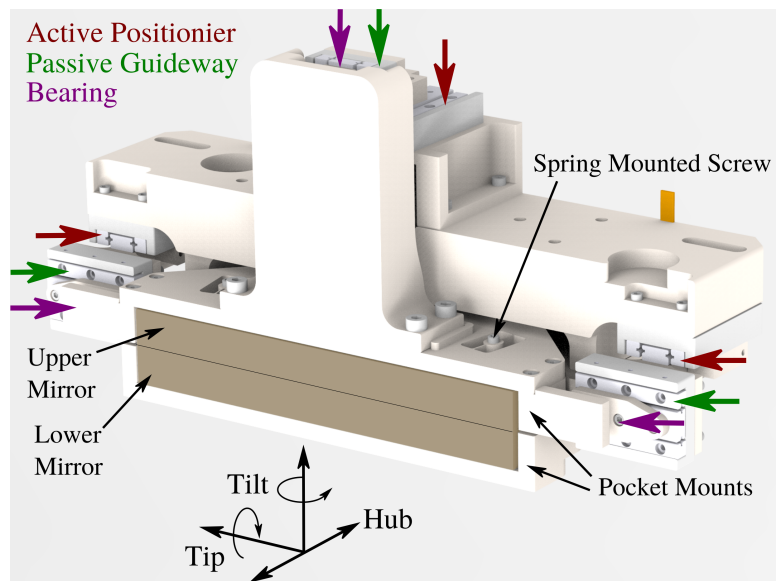

Figure 4.2.3: Annotated CAD drawing of the motorized grazing incidence mirror mounts. The upper mirror can be translated in normal direction and rotated around two axes by controlled movement of three piezo motor linear stages. Image taken from Schmid [22] with permission.

to repeatability in photon delay of 0.055 fs which is well below the photon pulse length. The two rotational degrees of freedom are necessary to overlap the focii of two beams spatially into the same spot. This is illustrated in Figure 3.1.7 and the overlap methodis discussed in Section 3.1.3.

The grazing incidence mirrors were specifically designed and manufactured for the application in this beamline. They consist of a Si substrate with a low surface roughness of 0.19 nm to 0.24 nm with a coating of (30.0 ± 1.5) nm C in order to achieve high reflectivity with high quality of the desired plane and ellipsoidal surfaces [22, section 9.4.2/9.4.3]. The ellipsoidal mirror is chosen such that it produces a point-to-point image of the FEL source point at 85 m distance into the focal point at 1 m distance. The focusing was commissioned using a wavefront sensor where a focal spot size as low as 3 μm (FWHM of diameter) could be achieved [22, section 9.6.1]
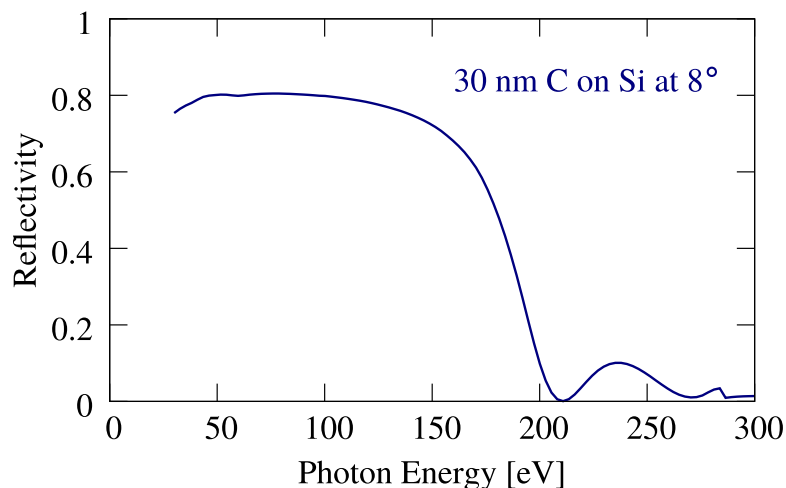
Figure 4.2.4: Reflectivity of the grazing incidence mirrors for varying photon energy at an angle of 8°. The mirrors have a reflectivity of roughly 75 % up to 150 eV. Image taken from Schmid [22] with permission.

The FEL beam can be diagnosed on four fluorescent screens along the beam path in the FlashRemi endstation. They are positioned before the split-and-delay mirrors, between the split-and-delay mirrors and the focusing mirrors, at the crossing point with the gas jet and behind the REMI main chamber. Most important is the screen in the reaction zone as it allows to determine the focal position and qualitatively also the quality of the focus. Thanks to that, it can be used to centre the focal plane into the gas jet and start with initial optimization of

the focal spot size observed from the fluorescence. When it comes to pump-probe experiments, this screen becomes a crucial part of the experiment as it is the measure to validate the spatial overlap between the two split beams in the focus. This procedure is further described in Section 3.1.3.

4.3 The Xenon Gas Jet

The SGJ is produced by supersonic expansion of xenon from a pressurized bottle with a pressure regulator through a nozzle of 30 um into the vacuum chamber. The pressure was reduced to below the lower end of the scale at 0.5 bar for optimal yield of dimers compared to large clusters. The setup is described in great detail by [22, 28, 53] and was used without change as described therein. The gas enters the vacuum chambers through a small nozzle, see Figure 4.3.1 on the right. A 3D translation manipulator can move the nozzle. A so-called skimmer extracts the SGJ from inside the indicated shock fronts, the so-called zone of silence. Afterwards, the SGJ has to pass several apertures before it enters the main chamber and crosses the focal point of the FEL. At the end, it is dumped directly into a turbo molecular pump, that is mounted at an angle, that optimizes pumping the SGJ. Horizontal and vertical slits can adjust the gas beam profile. Several pressure stages with additional turbo pumps remove the gas which was scattered from skimmers, apertures and slits in order to keep the background pressure in the main chamber as low as possible. The SGJ is usually cut in the horizontal direction such that it becomes thin, typically $d \approx 0.5\,\text{mm}$ to $1\,\text{mm}$, in the direction of FEL beam propagation. The target density was not directly measured. However, we can roughly estimate the density from the amount of singly charged xenon ions produced. Those are produced only by outer valence ionisation from the 5s or 5p orbitals. The measured ionisation yield is given by

$$Y = \varepsilon \cdot \sigma \cdot \frac{P}{A} \cdot N = \varepsilon \cdot \sigma \cdot \frac{P}{A} \cdot (\rho \cdot d \cdot A) \tag{4.3.1}$$

$$N = \frac{Y \cdot A}{\varepsilon \cdot \sigma \cdot P}, \tag{4.3.2}$$

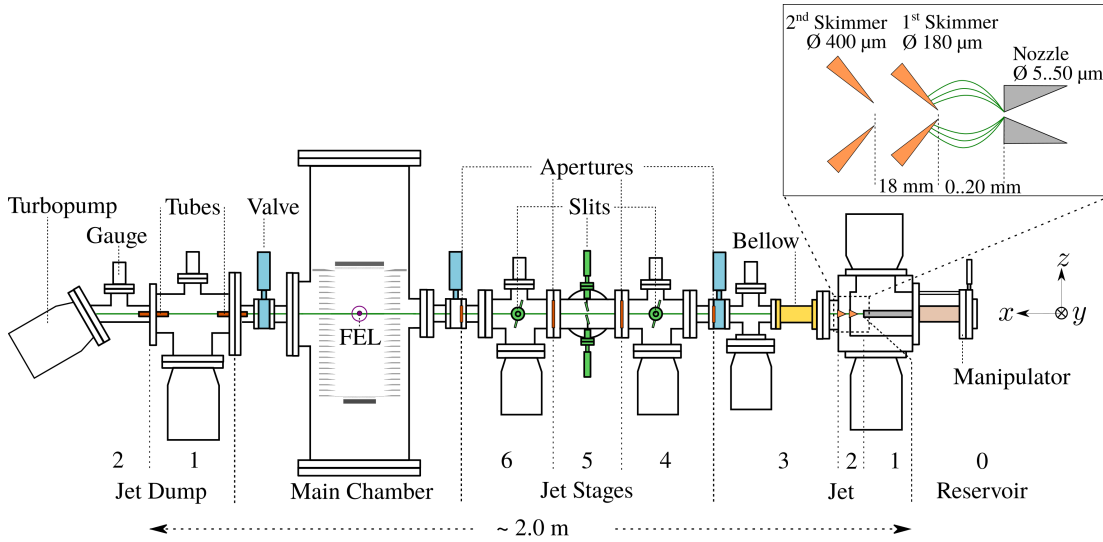$$\rho = \frac{Y}{\varepsilon \cdot \sigma \cdot P \cdot d}, \tag{4.3.3}$$

Figure 4.3.1: Schematic of SGJ target preparation. See main text for explanations. Image taken from Schmid [22] with permission.

where $Y = 0.087$ is the average ion yield measured for singly ionized xenon, $\sigma = 0.334\,\mathrm{Mb}$ is the total cross section at $100\,\mathrm{eV}$ photon energy [57] for 5s and 5p orbitals, $\varepsilon \approx 0.17$ is the detection efficiency for the Xe^{1+} ions (see Section 4.4), $P \approx 10\,\mathrm{\mu J}/100\,\mathrm{eV} \approx 6 \times 10^{11}$ is the average number of photons in a pulse and N is the number of Xenon atoms in the focal volume. The number of atoms is given by the product of the density ρ, the SGJ thickness d and the focal area $A \approx 10\,\mathrm{\mu m}^2$. Since the area part of the reaction volume is determined by the focal size and the ionisation rate is proportional to the intensity, the focal area cancels out in the area for the rate of linear processes. With this, we estimate target number densities in the order of $\rho_1 \approx 2.6 \times 10^7\,\mathrm{cm}^{-3}$ or on average $\langle N_1 \rangle \approx 0.26$ xenon atoms in the focal volume. Unfortunately, the density of dimers and trimers is harder to estimate as it is not certain, that they remain bound after absorption of a single photon. Nevertheless, we can give an upper limit on the dimer density by assuming that indeed all dimers stay bond and singly charged after outer valence ionisation. Then we can adjust Equation (4.3.3) to

$$\rho_2 = \frac{Y_2}{\varepsilon \cdot 2\sigma \cdot I \cdot d \cdot A} = \frac{Y_2}{2Y_1}\rho_1, \qquad (4.3.4)$$

where the additional factor of 2 comes from the fact that each dimer will have roughly twice the cross section for ionising of one of the constituents. Following

this, we get a dimer density of $\rho_2 \leq 6.6 \times 10^4 \, \text{cm}^{-3}$ or $\langle N_2 \rangle \leq 6.6 \times 10^{-4}$. The trimer density can not be estimated this way as stable trimers are not detected due to overlapping values of TOF and impact positions with ions from coulomb explosions resulting in Xe^{3+} or Xe^{4+} after ionisation by the following FEL pulse. Therefore we try to get a very rough estimate by extrapolating the dimer-to-monomer ratio to the trimer-to-dimer ratio. The production of dimers is typically modeled as a sequence of two collisions

$$Xe + Xe \rightleftharpoons Xe_2^* \qquad\qquad \{4.3.1\}$$

$$Xe_2^* + X \rightleftharpoons Xe_2 + X, \qquad\qquad \{4.3.2\}$$

where in the first step, the dimer forms in a (highly) excited state and in the second collision, any other particle X carries away the excitation energy as kinetic energy [58]. The equilibrium concentration of dimers is then an interplay between the forward and backward reaction rates of those collisions, which all depend on the strongly varying temperature and pressure during the adiabatic expansion through the nozzle. After the expansion, the mean distance between collisions is expected to be longer than the path to the reaction volume so that the dimer concentration remains stable from there on. In this picture, one can imagine the formation of trimers as further steps in the chain of collisions, namely

$$Xe_2 + Xe \rightleftharpoons Xe_3^* \qquad\qquad \{4.3.3\}$$

$$Xe_3^* + X \rightleftharpoons Xe_3 + X \cdot \qquad\qquad \{4.3.4\}$$

Here the difference is that the first collision happens between a dimer Xe_2, which already has a low concentration and a monomer. However, the concentration of the other collision partners Xe and X is identical to the scheme in the production of dimers. We can expect the forward reaction rate of Reaction $\{4.3.3\}$ to roughly scale with the dimer concentration compared to Reaction $\{4.3.1\}$. Following these assumptions we can also estimate here an upper limit of $\rho_3 \leq 167 \, \text{cm}^{-3}$ for the density of xenon trimers and $\langle N_3 \rangle \leq 1.7 \times 10^{-6}$. So, in conclusion, we will often find a xenon atom in focus and only rarely a dimer or a trimer.

The target temperature can be estimated based on the initial state of the gas before expansion into the experimental chamber. Assuming an adiabatic expansion of the gas initially at pressure p_0 and temperature T_0 through a thin circular hole

of diameter $d = 30\,\mu\text{m}$, one can derive the speed ratio

$$S_\infty = \frac{v_{\textbf{jet}}}{v_{\textbf{th}}} = A \left(\sqrt{2} \frac{p_0 d}{k_B T_0} \left(\frac{53 C_6}{k_B T_0} \right)^{1/3} \right)^B, \qquad (4.3.5)$$

where $v_{\textbf{jet}}$ is the directed flow velocity and $v_{\textbf{th}}$ is the maximum likelihood thermal velocity after expansion in the co-moving frame. A and B are empirical parameters which depend on the nozzle geometry and Laplace's coefficient γ of the gas, C_6 corresponds to the attractive part of the Lennard-Jones potential energy at a characteristic distance, and k_B is Boltzmann's constant [59]. The two fractions can be interpreted as first the area density of particles in the nozzle and second the cross section for collisions between two particles based on the Lennard-Jones potential. Unfortunately, we have no measurement of the initial pressure for the xenon measurements as it was below the scale minimum of 1 bar. From the spread of measured xenon monomer momenta in the direction of jet propagation $p_{\textbf{rms}} \approx (4.0 \pm 0.1)$ a.u. (see Table 4.1) we can estimate only an upper limit for the thermal velocity $v_{\textbf{th}} = \sqrt{\frac{2}{3}} v_{\textbf{rms}} \approx (29.9 \pm 0.8)\,\text{m/s}$, corresponding to a temperature of $T_\infty \leq (7.1 \pm 0.3)\,\text{K}$ and a backing pressure of $p_0 \geq (0.19 \pm 0.01)\,\text{bar}$, where we use Equation (4.3.5) with $A = 0.778$, $B = 0.495$, $C_6/k_B = 41.2 \times 10^{-43}\,\text{Kcm}^6$ [59] and $T_0 \approx 293.15\,\text{K}$. Dehmer and Dehmer report an optimized Xe_2 dimer ratio of $1\,\%$ using a $35\,\mu\text{m}$ diameter nozzle and a backing pressure of $460\,\text{Torr}$ (approximately $0.6\,\text{bar}$) at their SGJ source. From the pressure scale minimum, we can calculate a lower limit of $T_\infty \geq 1.4\,\text{K}$ or a momentum spread of $p_{\textbf{rms}} \geq 1.8$ a.u. accordingly.

4.4 The Reaction Microscope

Here, we will discuss the specifics of the FlashRemi, the measurement principle of REMIs is discussed earlier in Section 3.1.1. The FlashRemi, as it is now, was designed to observe especially coulomb explosion processes from small molecules together with some of the emitted electrons. A detailed description of the apparatus can be found in references [22, 28, 53]. Here we will compile the most relevant aspects of the xenon experiment and parameters specific to this experiment.

The spectrometer setup is illustrated in Figure 4.4.1. Ionic fragments from those processes will have a large momentum, so one has to keep the TOF small to

Figure 4.4.1: Spectrometer of the Remi. Image taken from Schmid [22] with permission.

prevent ions from missing the detector in the transverse direction. To deal with this, one can either apply a high electric extraction field or keep the distance between the reaction point and the detector small. In both cases the detector should be as large as possible. Strong extraction fields, however, reduce the momentum resolution in the TOF direction and would not allow to simultaneously resolve electron energies. Therefore the ion detector is placed rather close (10.5 mm) to interaction region, and the largest available MCP with a diameter of 120 mm is used. The electron detector has a diameter of 80 mm. A "Z stack" of three MCPs each is used and spatial resolution is achieved by delay line anodes. The ion detector has a set of two orthogonal delay lines, and the electron detector has three delay lines at an angle of 60° for reduced dead times. The electron detector is located further away at roughly 19.5 mm. Typical extraction fields over the 300 mm distance between the ion and the electron detector are $\frac{1200\,\text{V}}{300\,\text{mm}} \approx 40\,\text{V/cm}$. In measurements for improved resolution of the electrons momenta, the field strength was reduced to $\frac{220\,\text{V}}{300\,\text{mm}} \approx 7\,\text{V/cm}$. In front of each detector are two fine metal grids with a transmission area of 80 %. Those grids help to keep their plane on a homogeneous potential so that the high potential of the MCP detector is screened from the inner spectrometer part, where a homogeneous electric field is desired. An in-homogeneous field would imply lensing of ions and electrons and thereby blur the recorded impact positions and TOF.

In order to estimate the overall detection efficiency for ions, we compare the coincident detection event rate $R_\mathbf{c}$ with the event rate of ions $R_\mathbf{nc}$, both inside a specific kinetic energy region corresponding to that coincidence channel. If we detect the first ion from this coincidence, the probability of also detecting the second ion is given by the detection efficiency for the second ion. So we can calculate

$$\varepsilon_\mathbf{second} = \frac{R_\mathbf{both}}{R_\mathbf{first}}. \tag{4.4.1}$$

For this estimate, we use the reaction channel Xe^{1+} / Xe^{2+} as that channel, in contrast to other charge states, has a single, clear peak in KER around 6.5 eV. As the condition, we choose now that the kinetic energy of Xe^{1+} or Xe^{2+} is $2.5\,\text{eV} \leq E_\mathbf{kin} \leq 4.5\,\text{eV}$. We get $\varepsilon_{\text{Xe}^{1+}} = 0.17$ and $\varepsilon_{\text{Xe}^{2+}} = 0.22$. The maximum efficiency is in the worst case of the geometrical alignment limited by the product of the Open Area Ratio (OAR) ≈ 0.6 of the MCP and the transmissions of the grids in front of the MCP is ≈ 0.8 each. So geometrically, we could achieve at

least up to $\varepsilon = 0.384$, which is significantly higher than the values we calculated for Xe^{1+} / Xe^{2+}. Additionally, the detection efficiency of MCPs depends on the impact energy and the mass of the fragment. Heavy particles generally require more impact energy to reach the same detection efficiency [61]. The impact energy of the ions $Q \cdot V$ with a potential of $V \approx 3\,kV$ was already quite high and could not be further improved. Considering that for N-particle coincidences the detection efficiency scales like ε^N, these low values are clearly still problematic.

We will estimate the momentum resolution of the REMI for detected $^{129}Xe^{1+}$ ions from the measured momentum of isolated monomers and the momentum sum for a coincidence channel. The standard deviations of the respective distributions are listed in Table 4.1. We see that the best resolution is achieved in the $p_{\mathbf{z}}$

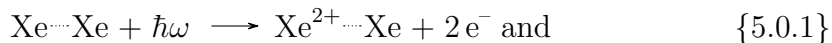| component	monomer	momentum sum $/\sqrt{2}$	electron
x	4.4	3.5	0.05
y	4.5	3.6	0.06
z	2.1	1.7	0.05

Table 4.1: Overview for resolution of $^{129}Xe^{1+}$ momenta from monomers and coincident detection of dimer fragments as well as uncorrelated electrons at the energy of 4d photoelectrons. All values are in a.u. and correspond to standard deviations of the respective distribution. The electron distributions are conditioned such that both other vector components fullfil $-0.2\,a.u. \leq p_i \leq 0.2\,a.u.$.

component, which corresponds to the TOF direction. The spatial dimensions corresponding to $p_{\mathbf{x}}$ and $p_{\mathbf{y}}$ show similar resolutions, roughly double the $p_{\mathbf{z}}$ value. The electron momenta are resolved much better due to the large difference in mass. However, the tabulated values are not achieved for all momenta. Firstly for $p_z \approx 0$, only energies up to $45\,eV$ can be detected in the transverse direction as higher energetic electrons are not captured by the magnetic field of approximately $10\,G$. Secondly, at a TOF of multiples of the cyclotron period, all electrons are guided to the same point on the detector. This leads to divergence of the resolution of the $p_{\mathbf{x}}$ and $p_{\mathbf{y}}$ vector components as well as severe issues with detector dead times.

Chapter 5

Results

The single-site ionized system is the starting point in all of the distribution processes that we want to study in this work. The charge is localized at one of the atoms because at a photon energy of $100\,\mathrm{eV}$ the ionisation of a 4d inner-valence electron has the largest cross-section. In the Xe monomer, this is followed by single or double AMD and we get Xe^{2+} or Xe^{3+} ions. For dimers this gives us the reactions

$$\mathrm{Xe}\text{···}\mathrm{Xe} + \hbar\omega \longrightarrow \mathrm{Xe}^{2+}\text{···}\mathrm{Xe} + 2\,\mathrm{e}^- \text{ and} \qquad \{5.0.1\}$$

$$\mathrm{Xe}\text{···}\mathrm{Xe} + \hbar\omega \longrightarrow \mathrm{Xe}^{3+}\text{···}\mathrm{Xe} + 3\,\mathrm{e}^- \; . \qquad \{5.0.2\}$$

When the single ion is at least doubly ionized, the system is always in a highly excited meta-stable state, as two separate but singly ionized ions have a potential energy that is lower by the difference of the first and second ionization potentials. But first the sudden increase of the electric dipole moment after ionization strongly increases the Van der Waals interaction between the ion and the near by neutral. This increase initially sets the system in a state that is stronger bound than the previous neutral state. Already in the $\mathrm{Xe}\text{···}\mathrm{Xe}^+$ state, the configuration with the least potential depth of $0.06\,\mathrm{eV}$[62] is more than two times deeper than the neutral ground state potential with $0.023\,\mathrm{eV}$[63]. In consequence, the single-site multiply-charged dimer ions will initially experience a force that is directed towards shorter bonds. Only when our system turns into a dimer with multiple charge centres the Coulomb force on the nuclei leads to sudden dissociation, the so-called Coulomb Explosion, and the system relaxes to its final potential minimum while releasing

the energy into kinetic energy. The goal for this study on the smallest Xe clusters is to investigate those processes that bring a system from localized charge and electronic excitation to a system with distributed charges and finally its end by fragmentation. In Section 5.3 we will discuss, how charge is distributed over the dimer from the ionized, yet still bond states after Reactions {5.0.1} and {5.0.2}. We find that the triply-charged dimer rapidly distributes the charges, but the doubly-charged dimers distribute it rather slowly.

The first indication of processes that go beyond simply distributing the charge over the dimer can be seen by comparing the total charge of the final state between individual Xe ions and dimers. In the isolated case, Xe^{2+} is the dominant channel while for the dimer it is a charge count of 3 (see Figure 5.0.1). Additionally, it is observed that some dimers are detected still with intact bond when they have a single charge, but not when they have a higher charge. So the Xe_2^+ dimer states are stable up to the µs timescale of the TOF, which is not the case for 2 or more charges.
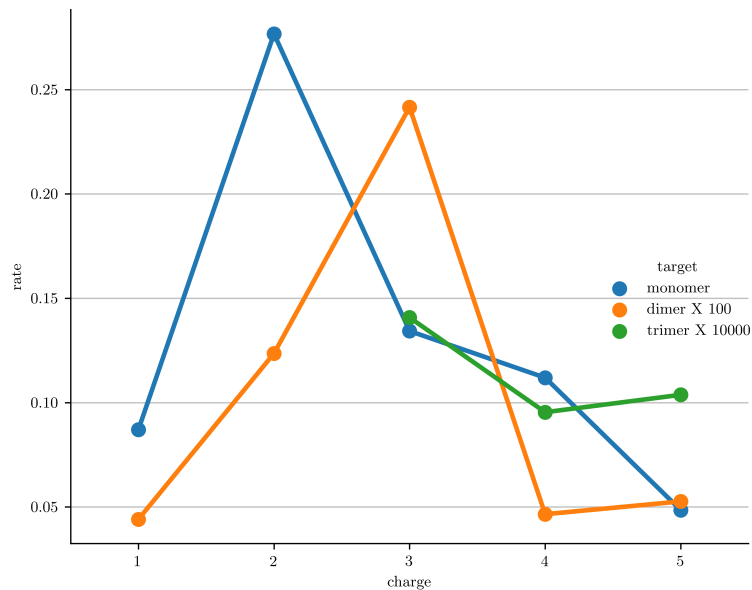

Figure 5.0.1: Event rate for monomers, dimers and trimers of Xe for different total charge counts, i.e. the sum of positive charges on all ions that were assigned to one coincidence by the momentum sum condition. While two charges is the most likely final state for monomers, three charges becomes the most likely result in dimers. Dimers are only detected intact for a charge of 1, all higher charges are only detected by their fragments. Trimer events are not detected below 3 charges.

To go further, we can compare how the energy of the emitted electrons correlates with monomers, dimers and trimers. In Figure 5.0.2 we see that a charge state of 3 comes for monomers together with many low-energy electrons. This is the marker for double AMD, where the two electrons share only 6.5 eV or less, depending on the final state of the ion. But when we get 3 charges in sum on a dimer this marker at low energy decreases, and even more for the trimer. This indicates that double AMD is not anymore the driving process producing the additional charges. It must be something that ionizes the electrons from one of the other atoms where electrons are still weaker bound and can leave the system with more kinetic energy. So we have to look into reaction chains that go via single AMD or
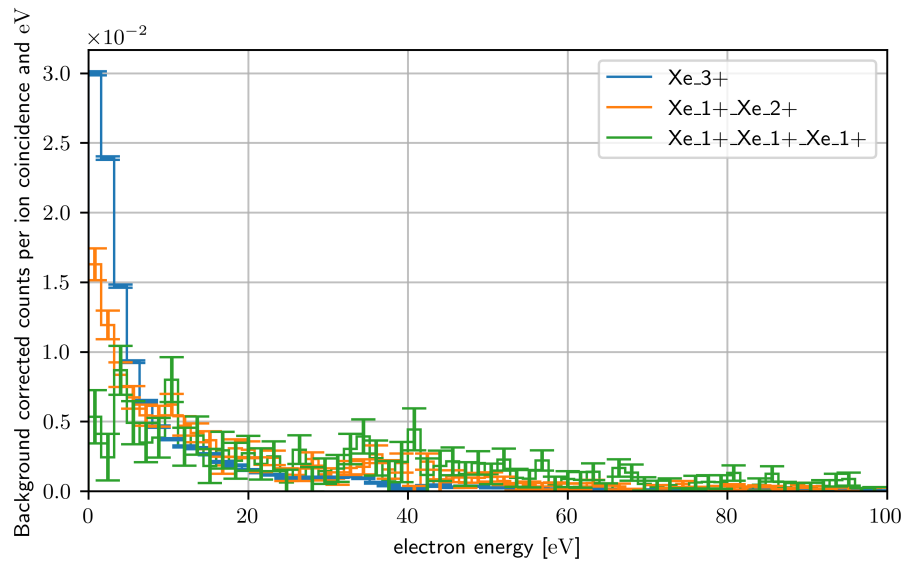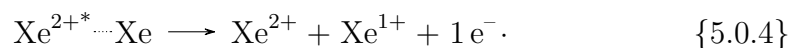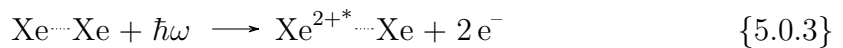

Figure 5.0.2: Distribution of electron energies in correlation with Xe^{3+}(blue), Xe^{1+} / Xe^{2+}(orange) and Xe^{1+} / Xe^{1+} / Xe^{1+}(green). All three distributions are corrected for background events (see Section 3.2.3) and normalized to the event rate for the respective ion channel. A total count of three charges is mainly correlated with low energetic electrons from double AMD in monomers. In dimers and trimers, the distribution is correlated more with higher energetic electrons.
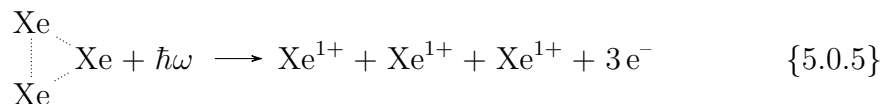
Shake Up photoionization (SU) into an electronically excited state and then use the energy to drive further ionization of the dimer:

$$Xe\text{---}Xe + \hbar\omega \longrightarrow Xe^{2+^*}\text{---}Xe + 2\,e^- \qquad \{5.0.3\}$$

$$Xe^{2+^*}\text{---}Xe \longrightarrow Xe^{2+} + Xe^{1+} + 1\,e^- \cdot \qquad \{5.0.4\}$$

These processes of delayed ionization of the neutral partner atom are expected to be cICD or ETMD(2), see Section 2.4. We will go into the question of how the dimer is charged triply in Section 5.3.2 by looking deeper into one specific reaction channel, the cICD. This channel starts from doubly excited $5s^{-2}$ states of the Xe^{2+} ion that have sufficient energy to ionize the neutral Xe immediately at the inter-nuclear distance of the ground state of the dimer.

However, not all of the dimers relax their electronic excitation into further ionization. We also see that it can be transferred to kinetic energy of the ions by the mechanism of Frustrated Ionisation (FI). Section 5.4 shows clear evidence of FI.

In the Xe trimer systems we can only see fragments with total charge of 3 or more. So, energetically we can only get one coincidence channel by a single photon, which is that all ions are Xe^{1+}

$$\begin{matrix} Xe \\ | \\ Xe \end{matrix} Xe + \hbar\omega \ \longrightarrow \ Xe^{1+} + Xe^{1+} + Xe^{1+} + 3\,e^{-} \hspace{2em} \{5.0.5\}$$

We will discuss the ETMD(3) mechanism as main driver of Reaction {5.0.5} in Section 5.5 and estimate an upper limit for the timescale of the reaction.

In the Sections 5.3 to 5.5 we will compare the experimental data with our classical simulation (see Section 3.3.6) to validate our interpretation of the measured data. For this we use different scenarios that we describe in Section 5.2.

5.1 Nomenclature for Reactions

When describing the individual steps of reactions, we will use the following short notation in the next sections. When we write the reaction as

$$A + B \xrightarrow[\text{condition}]{\text{time scale}} C + D,$$
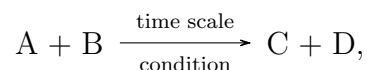
we mean: The reaction happens at given time scale, but only if the condition holds. If the scale is τ, this further means the reaction happens after a random time t which is exponentially distributed like $P(t) \propto \exp(-t/\tau)$. If the reaction is fast or there is no further condition, they are omitted:
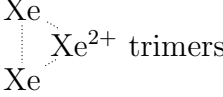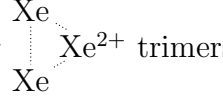
$$A + B \xrightarrow[\text{always}]{\tau \approx 0} C + D$$
$$\Longleftrightarrow A + B \longrightarrow C + D$$
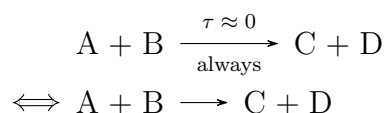
When we skip to final states, this is marked as:

$$A + B \xrightarrow{\infty} C + D$$
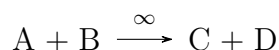
5.2 Scenarios of the Classical Simulation

The classical simulation is described in Section 3.3.6. We simulated five different scenarios:

1. All distribution of charge is described by a single fast CT model after local ionisation

2. All distribution of charge is described by a single slow CT model after local ionisation

3. Charge is distributed instantly after the pump pulse, but with CT after probe

4. Additionally to fast CT, ETMD(3) is allowed for $\begin{matrix} \text{Xe} \\ | \\ \text{Xe} \end{matrix}$ Xe^{2+} trimers

5. Additionally to slow CT, ETMD(3) is allowed for $\begin{matrix} \text{Xe} \\ | \\ \text{Xe} \end{matrix}$ Xe^{2+} trimers

The last two scenarios with ETMD(3) are only relevant for trimers, as ETMD(3) is by definition not active for dimers. All of the scenarios are simulated once with absorption of only one single photon and once with absorption of two photons in a delay scan. The dimers start either as Xe_2^{2+} or Xe_2^{3+}, the trimers start as Xe_3^{3+} or, especially for the ETMD(3) scenarios, as Xe_3^{2+}. The two rates of CT

scenario	A / fs^{-1}	B/Å^6	initial charges
1	2.7	0	local
2	0.0108	0	local
3	2.7	0	distributed
4	2.7	500	local
5	0.0108	500	local

Table 5.1: Simulation parameters for the different scenarios. A is the rate factor of CT and B is the additional factor for ETMD(3) processes, see Equations (3.3.11) and (3.3.13). Local initial charges means the system starts with all charges on one ion. Distributed initial charges means all charges are equally distributed among the cluster.

were chosen such that for the fast rate of 2.7 1/fs the variation of the event rate of the $^{129}Xe^{1+}$ / $^{129}Xe^{4+}$ channel matches between simulation and the experiment, see Figure 5.2.1. The slow rate of 0.01 1/fs was chosen such that it matches the variation of the event rate of $^{129}Xe^{1+}$ / $^{129}Xe^{3+}$, see Figure 5.2.1. For each delay value in the range from -120 fs to 1000 fs in steps of 0.1 fs, one simulation was performed for each scenario. The FEL pulse duration was assumed to be 50 fs (std). The results are then binned into the same bins as the experimental data.
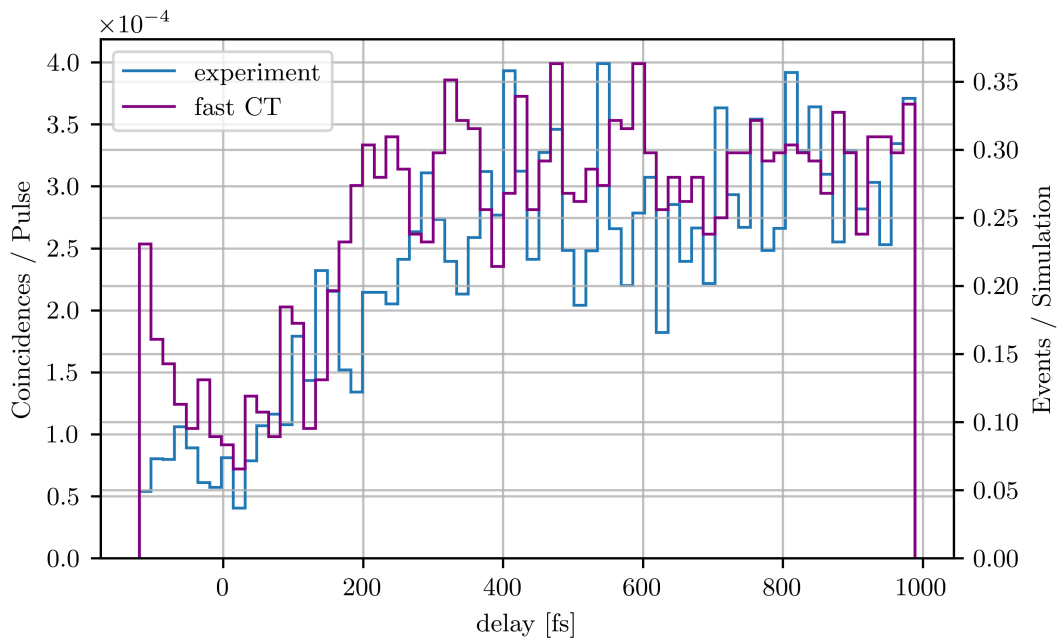
Figure 5.2.1: Event rate for the coincidence channel $^{129}\text{Xe}^{1+}$ / $^{129}\text{Xe}^{4+}$ from experiment and simulation scenario 1, the fast CT.
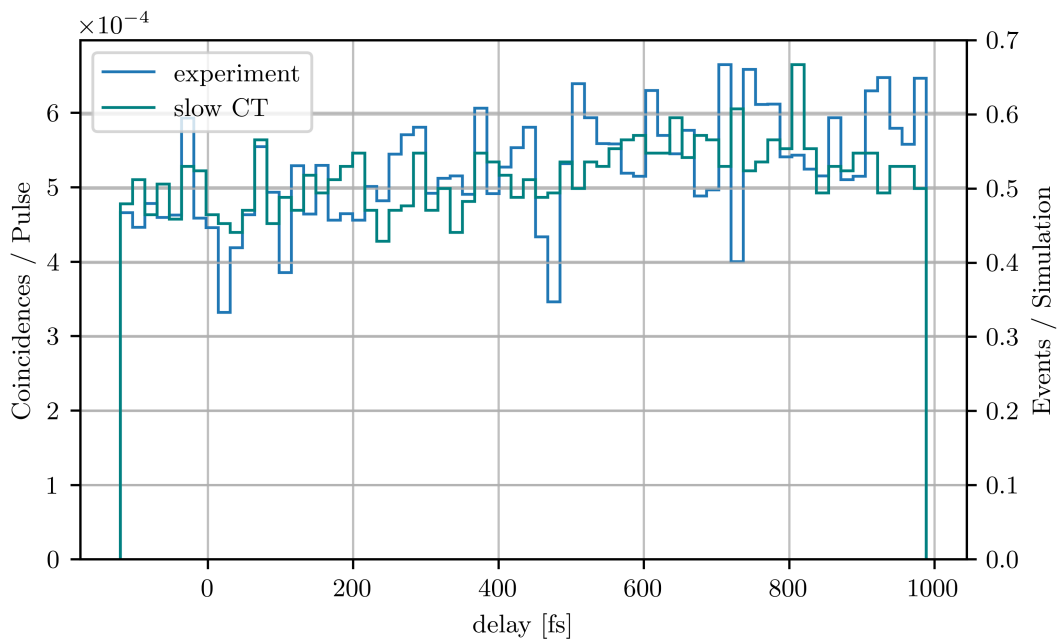

Figure 5.2.2: Event rate for the coincidence channel $^{129}\text{Xe}^{1+}$ / $^{129}\text{Xe}^{3+}$ from experiment and simulation scenario 2, the slow CT.
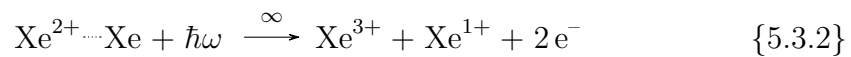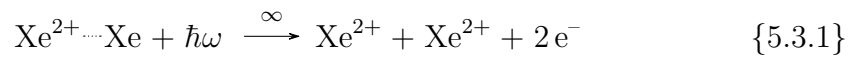
5.3 Charge Transfer from Single-Site into Two-Site Ionised Dimers

The 4d inner-valence photoionisation is the dominant process when Xe absorbs its first photon in the $100\,\mathrm{eV}$ region. It is followed by a fast local single or double AMD turning the atom into a Xe^{2+} or Xe^{3+} ion. For Xe dimers that means they are ionized into an state of asymmetric distribution of those charges. The question arises how the cluster reacts in the following and we will go through the following reaction chain in this Section.

5.3.1 Slow Charge Transfer into Xe^{1+} / Xe^{1+}

When we compare the measured KER of Xe^{1+} / Xe^{1+} with the expected values at $4.4\,\text{Å}$, the distribution is clearly shifted to higher KERs with a peak around $3.8\,\mathrm{eV}$, corresponding to $3.9\,\text{Å}$ internuclear distance. Therefore, we conclude that the nuclei move to closer distances before CT takes place. As movement of such heavy nuclei takes some time, the process must be rather slow. Comparing the Xe^{1+} / Xe^{1+} KER with simulated values (see Figure 5.3.1), we see that a slow CT can explain the distribution very well, but the instant transfer and the fast CT cases can be excluded.

We investigate the dynamics by looking into reaction products that are created by another photon. The second photon can still trigger the 4d ionization and subsequent single AMD and thereby does a double ionization on one of the Xe. The double AMD of the neutral Xe, however, is now blocked by the Coulomb potential of the already ionized partner. As they only separate once both are charged, we do not expect any double AMD to be possible in the second step. This means our pump-probe scheme turns $\mathrm{Xe_2}^{2+}$ into $\mathrm{Xe_2}^{4+}$ systems

$$\mathrm{Xe}^{2+}\text{---}\mathrm{Xe} + \hbar\omega \xrightarrow{\infty} \mathrm{Xe}^{2+} + \mathrm{Xe}^{2+} + 2\,\mathrm{e}^- \qquad \{5.3.1\}$$

$$\mathrm{Xe}^{2+}\text{---}\mathrm{Xe} + \hbar\omega \xrightarrow{\infty} \mathrm{Xe}^{3+} + \mathrm{Xe}^{1+} + 2\,\mathrm{e}^- \qquad \{5.3.2\}$$

When we probe a $\mathrm{Xe}\text{---}\mathrm{Xe}^{2+}$ system, the probe photon can either arrive before
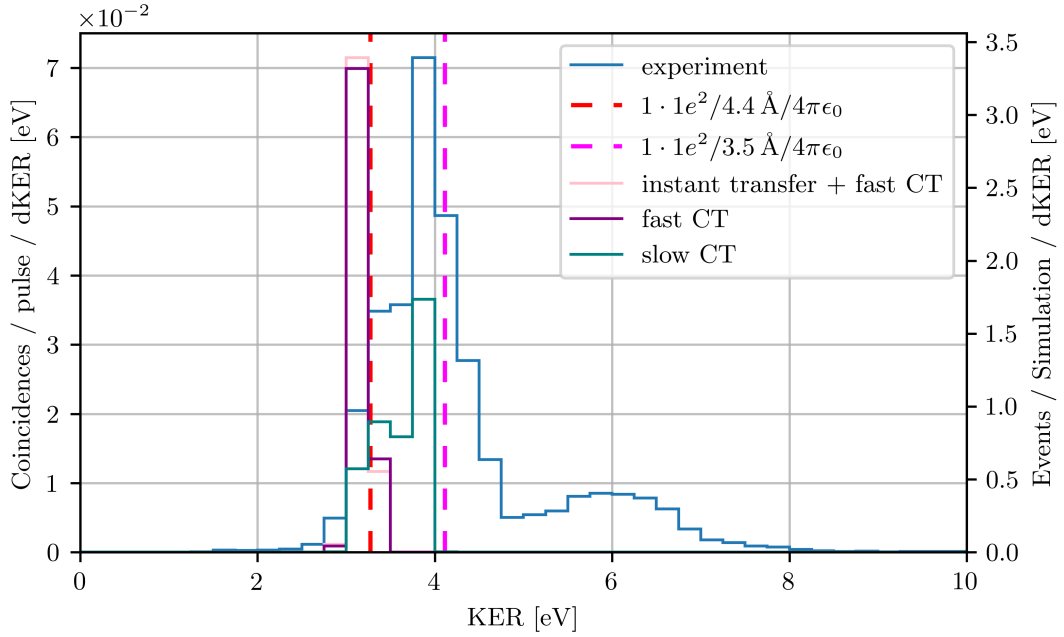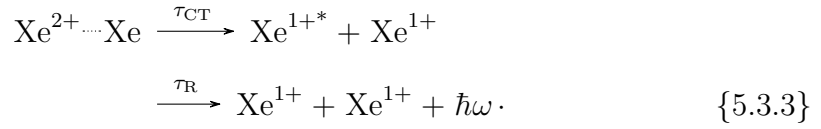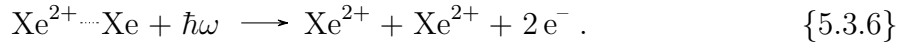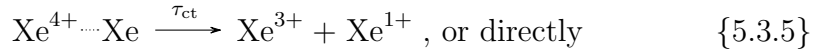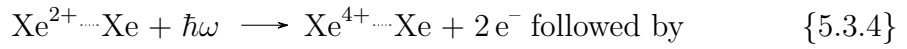
Figure 5.3.1: Distribution of simulated KER values of $^{129}\text{Xe}^{1+}$ / $^{129}\text{Xe}^{1+}$ in comparison with the measured distribution.
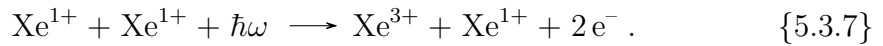
or after the charge transfer, which is by itself

$$\text{Xe}^{2+}\text{-}\text{Xe} \xrightarrow{\tau_{\text{CT}}} \text{Xe}^{1+*} + \text{Xe}^{1+}$$

$$\xrightarrow{\tau_{\text{R}}} \text{Xe}^{1+} + \text{Xe}^{1+} + \hbar\omega \cdot \qquad \{5.3.3\}$$

When it arrives before, we can get

$$\text{Xe}^{2+}\text{-}\text{Xe} + \hbar\omega \longrightarrow \text{Xe}^{4+}\text{-}\text{Xe} + 2\,\text{e}^{-} \text{ followed by} \qquad \{5.3.4\}$$

$$\text{Xe}^{4+}\text{-}\text{Xe} \xrightarrow{\tau_{\text{ct}}} \text{Xe}^{3+} + \text{Xe}^{1+} \text{ , or directly} \qquad \{5.3.5\}$$

$$\text{Xe}^{2+}\text{-}\text{Xe} + \hbar\omega \longrightarrow \text{Xe}^{2+} + \text{Xe}^{2+} + 2\,\text{e}^{-} . \qquad \{5.3.6\}$$

If charge transfer already happened, there is only one possibility with

$$\text{Xe}^{1+} + \text{Xe}^{1+} + \hbar\omega \longrightarrow \text{Xe}^{3+} + \text{Xe}^{1+} + 2\,\text{e}^{-} . \qquad \{5.3.7\}$$

No matter how we get to Xe^{1+} / Xe^{3+}, as long as the ions are close together, CT

is still possible

$$Xe^{3+} + Xe^{1+} \xrightarrow[R < R_c]{\tau_{ct}} Xe^{2+*} + Xe^{2+}$$

$$\xrightarrow{\tau_R} Xe^{2+} + Xe^{2+} + \hbar\omega \ . \qquad \{5.3.8\}$$
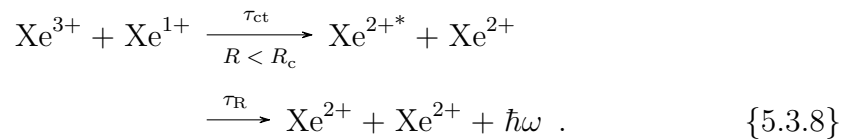
In Figure 5.3.2 we can see all channels associated with the pump-probe measurement of $Xe\text{-}Xe^{2+}$. We see that Xe^{1+} / Xe^{1+} shows no change of the KER distribution with respect to the delay, Xe^{2+} / Xe^{2+} only a very weak change for KER below 10 eV, but Xe^{1+} / Xe^{3+} shows a clear difference between the single-pulse measurement and pump-probe at long delay. To validate that the $Xe\text{-}Xe^{2+}$ channel is probed into Xe^{1+} / Xe^{3+} and Xe^{2+} / Xe^{2+} we can check that the KER asymptotically goes to the KER value of Xe^{1+} / Xe^{1+}. This can be seen in Figure 5.3.3.

In the pump-probe measurement channel Xe^{1+} / Xe^{3+} we see that a certain area below the main peak in KER fills up the region from 4 eV to 8 eV. Although the event rate is small, there appears a clear cut off at low energy. The cut off separates from the main line roughly after 200 fs and asymptotically goes to the Xe^{1+} / Xe^{1+} KER value. This continuously distributed KER arises since the fragmentation of the precursor state is randomly distributed. This behaviour is reproduced by the simulation, see Figure 5.3.4. The simulation seems to overestimate the tail towards high KER, however.

The other probe channel Xe^{2+} / Xe^{2+} is shown in Figure 5.3.5. Both in simulation and experiment, there is mainly a constant KER around the expected value. However we see only in the simulation that after roughly 200 fs a part of the distribution splits apart towards higher KER. This part correspond to dimers that move closer together in the bound ion state and then the neutral is ionized by the second photon. That brings it immediately to the exploding Xe^{2+} / Xe^{2+} state. This behaviour is not clearly happening at a certain delay in the experimental data. In that region of KER, there is apparently constant background in the experimental data that might hide the effect.
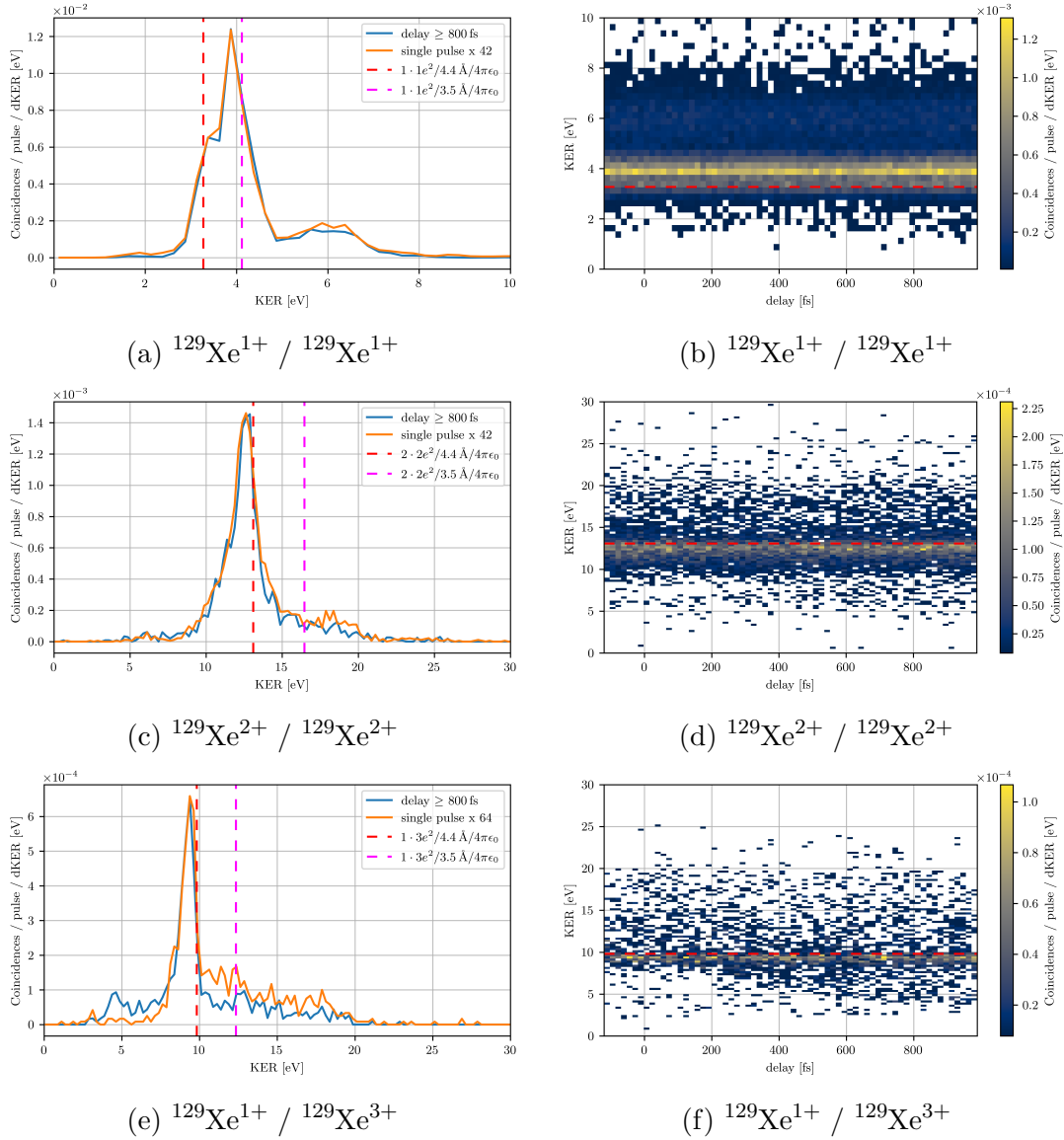
(a) $^{129}\text{Xe}^{1+}$ / $^{129}\text{Xe}^{1+}$

(b) $^{129}\text{Xe}^{1+}$ / $^{129}\text{Xe}^{1+}$

(c) $^{129}\text{Xe}^{2+}$ / $^{129}\text{Xe}^{2+}$

(d) $^{129}\text{Xe}^{2+}$ / $^{129}\text{Xe}^{2+}$

(e) $^{129}\text{Xe}^{1+}$ / $^{129}\text{Xe}^{3+}$

(f) $^{129}\text{Xe}^{1+}$ / $^{129}\text{Xe}^{3+}$

Figure 5.3.2: Left column: Comparison of KER spectra for long delays ($\geq 800\,\text{fs}$) with a single pulse measurement. The single pulse spectrum is scaled such that the maximum is equal to the other spectrum. Only in the Xe^{1+} / Xe^{3+} channel slight differences above and below the main KER peak are visible in panel (e). Right Column: Corresponding Histograms of KER versus delay. In panels (b) and (d) no obvious delay dependence is visible, but in panel (f) it is visible that the Xe^{1+} / Xe^{3+} event rate is reduced for small delays in the KER region from $4\,\text{eV}$ to $8\,\text{eV}$.
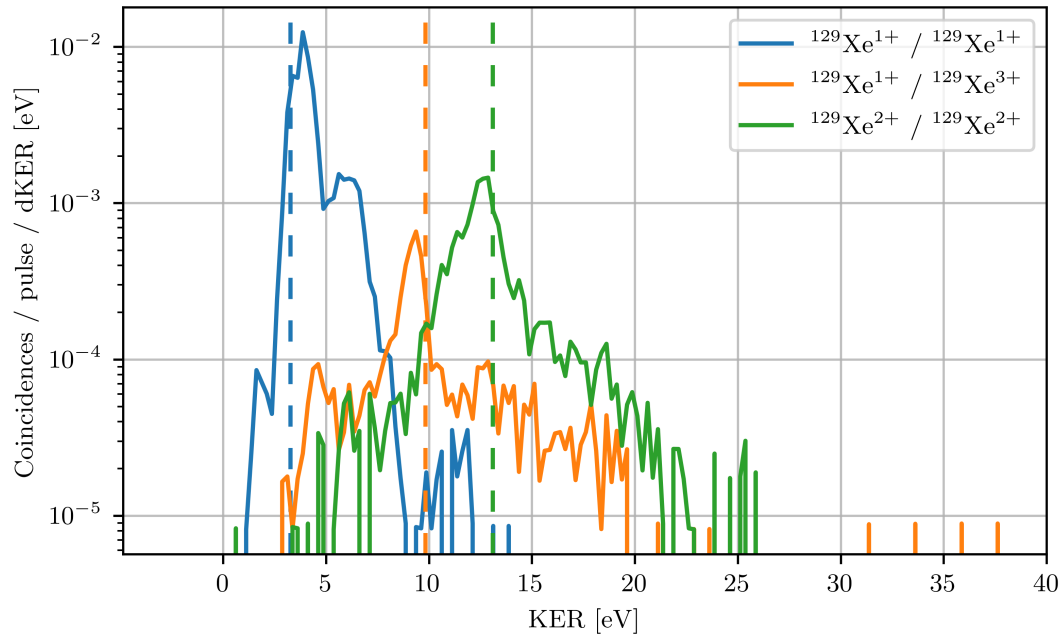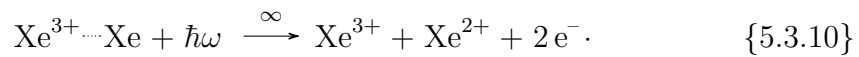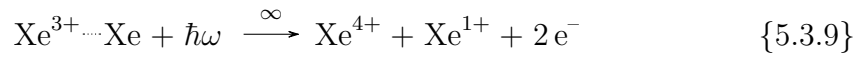
Figure 5.3.3: Distribution of KER at long pump-probe delay ($\geq 800\,\mathrm{fs}$). Part of the distributions of the $^{129}\mathrm{Xe}^{1+}$ / $^{129}\mathrm{Xe}^{3+}$ and $^{129}\mathrm{Xe}^{2+}$ / $^{129}\mathrm{Xe}^{2+}$ channels come close to the average value of $^{129}\mathrm{Xe}^{1+}$ / $^{129}\mathrm{Xe}^{1+}$.

5.3.2 Triple Ionisation of Xenon Dimers by Collective ICD

In this Section we consider the process of cICD as one of the mechanisms that drive the increased charge count on dimers compared to monomers. This channel is expected to occur from the doubly excited $5\mathrm{s}^{-2}$ $\mathrm{Xe\cdots Xe}^{2+}$ states, see Section 2.4 or Figure 5.3.6.

As before in Section 5.3, the second photon can not bring any of two Xe to a state that results in double AMD due to the Coulomb blocking. The probe photon will bring $\mathrm{Xe_2}^{3+}$ into $\mathrm{Xe_2}^{5+}$ systems by photoionisation and single AMD

$$\mathrm{Xe}^{3+}\!\cdots\mathrm{Xe} + \hbar\omega \xrightarrow{\infty} \mathrm{Xe}^{4+} + \mathrm{Xe}^{1+} + 2\,\mathrm{e}^{-} \qquad \{5.3.9\}$$

$$\mathrm{Xe}^{3+}\!\cdots\mathrm{Xe} + \hbar\omega \xrightarrow{\infty} \mathrm{Xe}^{3+} + \mathrm{Xe}^{2+} + 2\,\mathrm{e}^{-}. \qquad \{5.3.10\}$$

When we look at the reaction channels that start with a $\mathrm{Xe\cdots Xe}^{3+}$ dimer ion, we see very prominent pump-probe features in Figure 5.3.7. And in Figure 5.3.8 we see that both Xe^{1+} / Xe^{4+} and Xe^{2+} / Xe^{3+} show a prominent peak close to
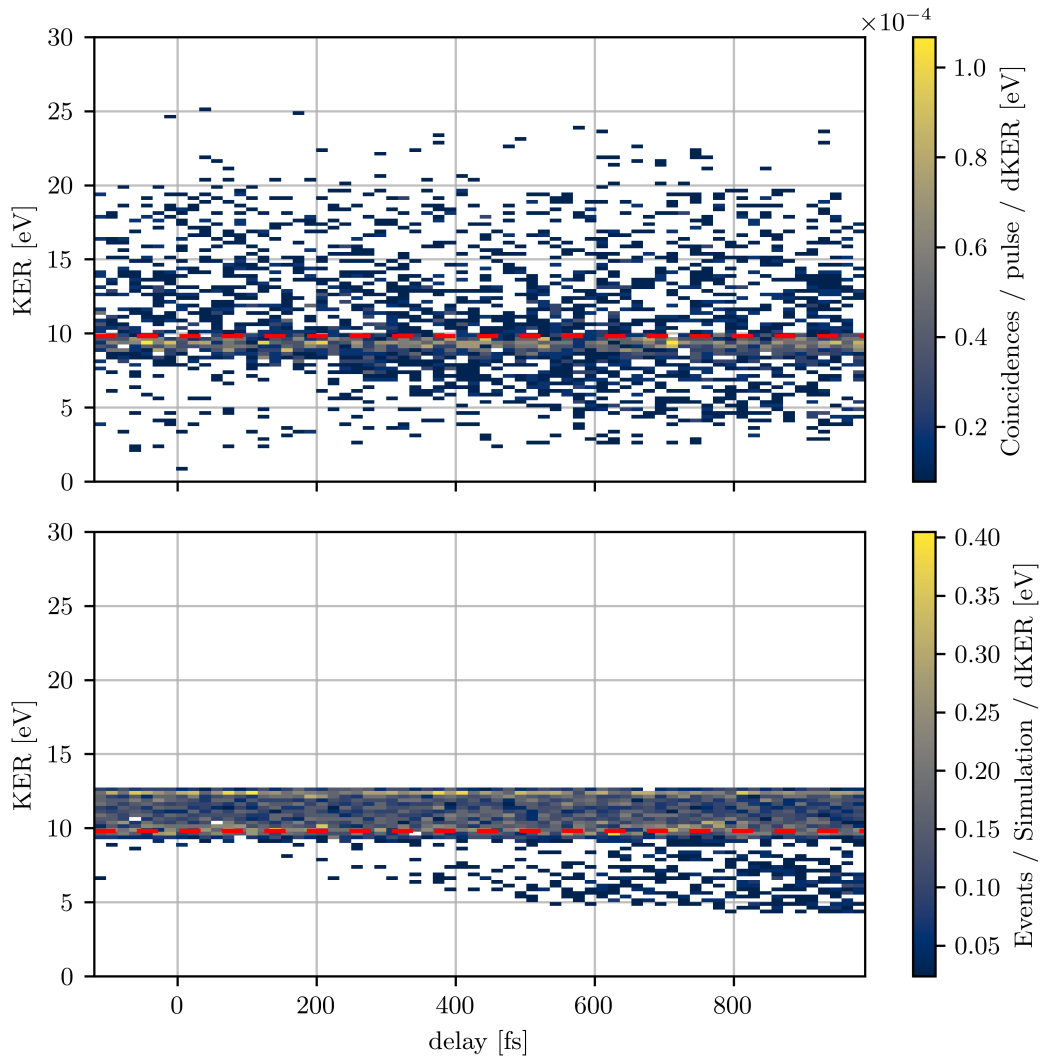
Figure 5.3.4: Distribution of KER values of $^{129}\text{Xe}^{1+}$ / $^{129}\text{Xe}^{3+}$ in dependence of the delay. The top panel shows experimental data, the bottom panel shows simulated data with the slow CT scenario.
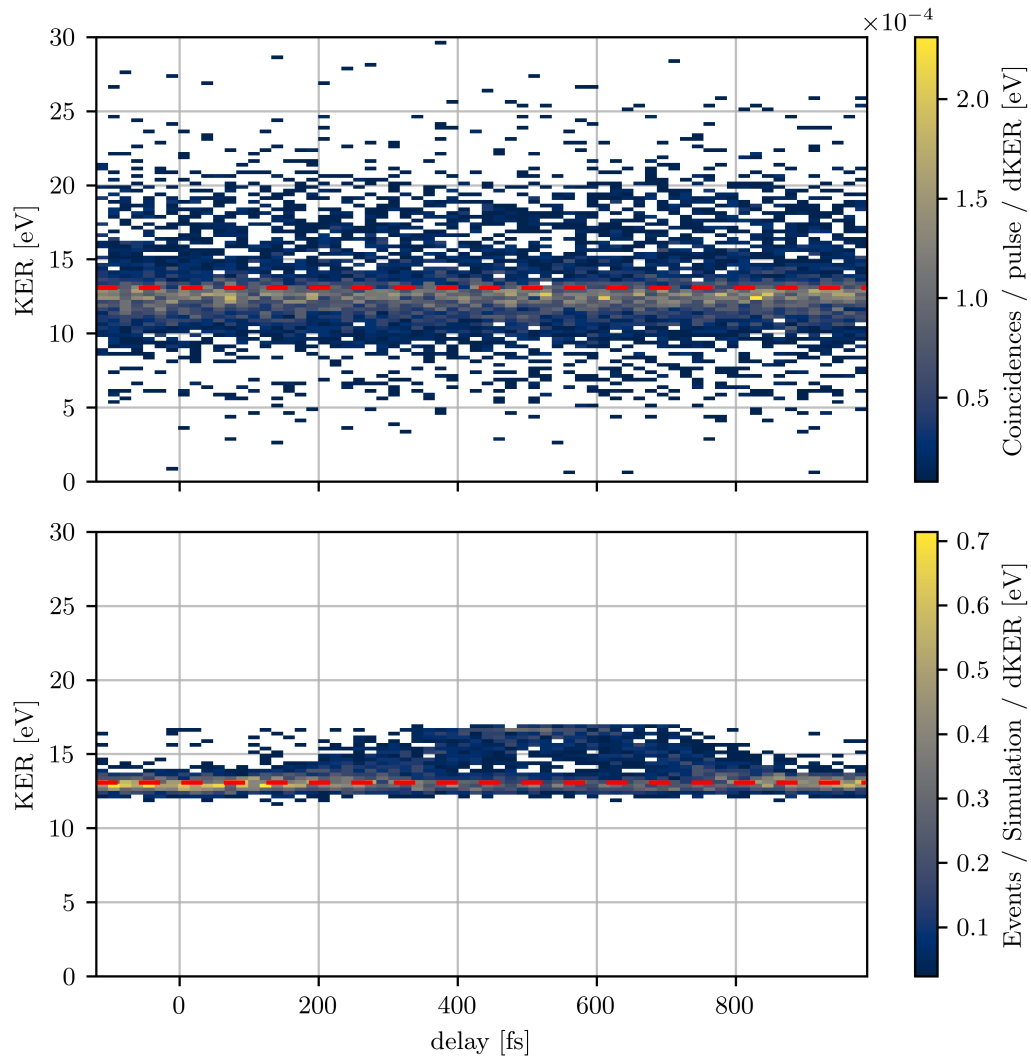
Figure 5.3.5: Distribution of KER values of $^{129}\mathrm{Xe}^{2+}$ / $^{129}\mathrm{Xe}^{2+}$ in dependence of the delay. The top panel shows experimental data, the bottom panel shows simulated data with the slow CT scenario.
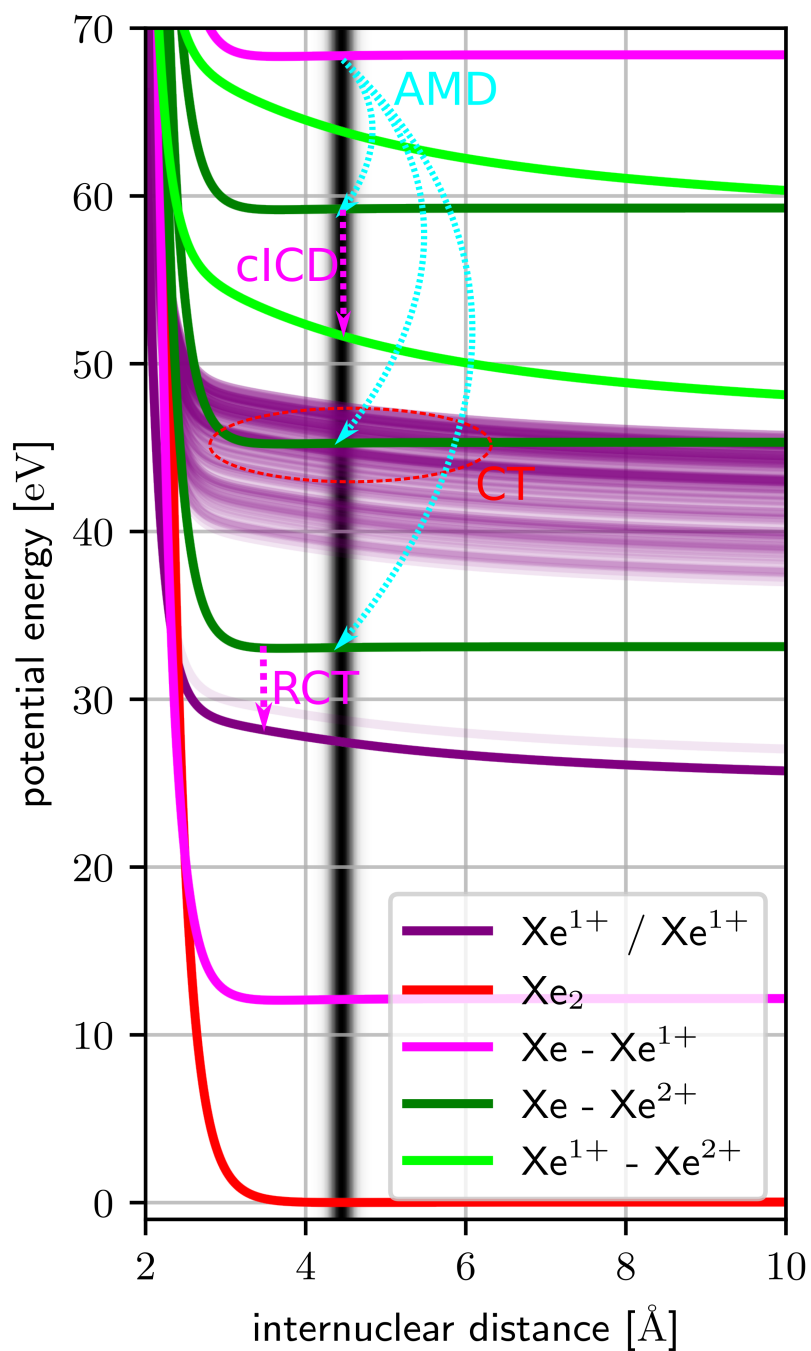
Figure 5.3.6: Selected potential energy curves of Xe⋯Xe and Xe⋯Xe²⁺ dimers. The expected decay processes after 4d inner-valence ionisation and single AMD are indicated between the curves. For further explanation see Figure 2.4.1 in Section 2.4.
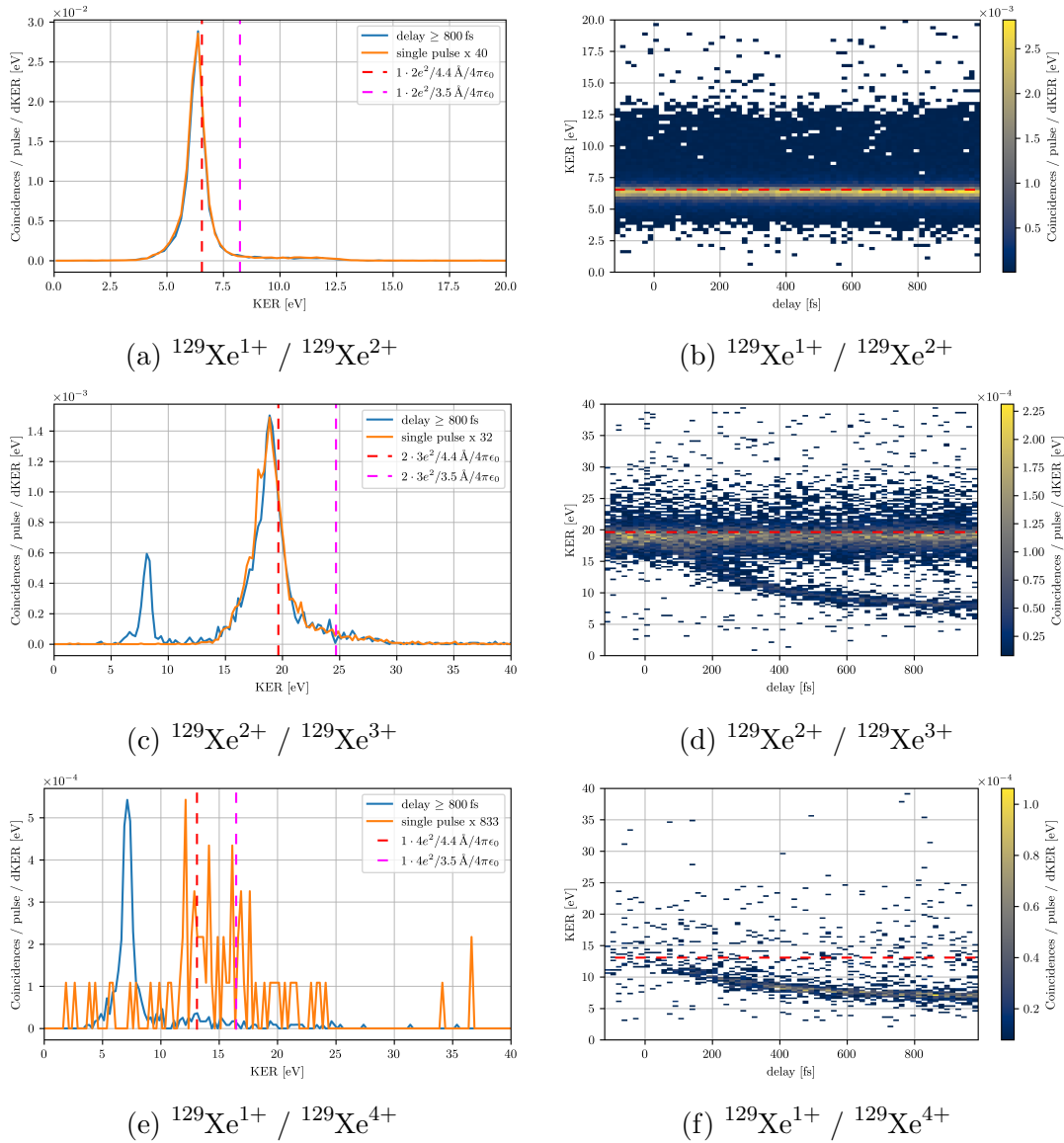
(a) $^{129}Xe^{1+}$ / $^{129}Xe^{2+}$

(b) $^{129}Xe^{1+}$ / $^{129}Xe^{2+}$

(c) $^{129}Xe^{2+}$ / $^{129}Xe^{3+}$

(d) $^{129}Xe^{2+}$ / $^{129}Xe^{3+}$

(e) $^{129}Xe^{1+}$ / $^{129}Xe^{4+}$

(f) $^{129}Xe^{1+}$ / $^{129}Xe^{4+}$

Figure 5.3.7: Left column: Comparison of KER spectra for long delays ($\geq 800\,\mathrm{fs}$) with a single pulse measurement. The single pulse spectrum is scaled such that the maximum is equal to the other spectrum. Right column: respective histograms of KER versus delay. No delay dependence is visible in panels (a) and (b) for the Xe^{1+} / Xe^{2+} channel. The Xe^{2+} / Xe^{3+} channel in panels (c) and (d) shows a pump-probe signature of fragmenting dimers in addition to a constant contribution of dimers that explode at the equilibrium internuclear distance. The Xe^{1+} / Xe^{4+} channel in panel (e) and (f) only shows the delay dependent signature of fragmenting dimers and almost no events at zero delay.
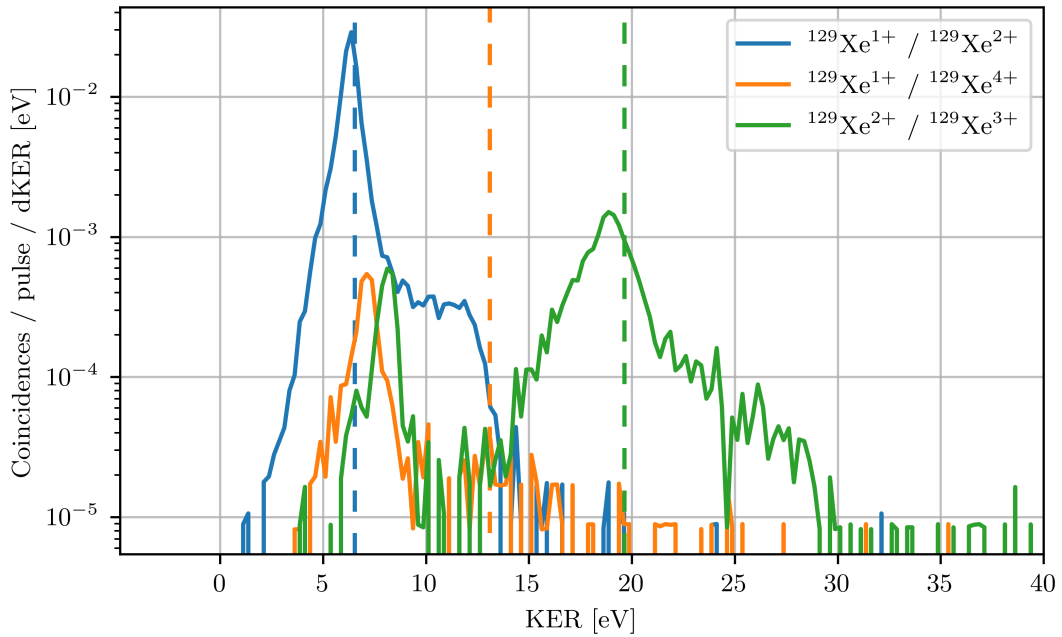
Figure 5.3.8: Distribution of KER at long pump-probe delay ($\geq 800\,\text{fs}$). Part of the distributions of the $^{129}\text{Xe}^{1+}$ / $^{129}\text{Xe}^{4+}$ and $^{129}\text{Xe}^{2+}$ / $^{129}\text{Xe}^{3+}$ channels come close to the average value of $^{129}\text{Xe}^{1+}$ / $^{129}\text{Xe}^{2+}$.

the KER of Xe^{1+} / Xe^{2+}. For Xe^{1+} / Xe^{4+}, this is the dominant peak at long delays and at short delays the event rate drops to zero. That indicates that this channel is efficiently suppressed at zero delay. Looking at Figure 5.3.9, we see that for Xe^{1+} / Xe^{2+} the slow CT can not be the most relevant process, as no such peak at high KER is observed in the experimental data. The fast CT or even instant ionisation into Xe^{1+} / Xe^{2+} agree much better with the measurement.

As the fast CT scenario was fitted to the event rate of Xe^{1+} / Xe^{4+}, it naturally reproduces the suppression of events at zero delay, see also Figure 5.2.1. However, it also reproduces both Xe^{1+} / Xe^{4+} and Xe^{2+} / Xe^{3+} very good in the relation of KER and delay, see Figures 5.3.10 and 5.3.11. When we compare this to the smeared out KER in Xe^{1+} / Xe^{3+}, see Figure 5.3.4, we can tell from the appearance of a defined line in the KER-delay plot: The probed intermediate state must be reached very shortly after the pump photon was absorbed.

Figure 5.3.12 shows the event rate of the Xe^{1+} / Xe^{4+} channel depending on the delay. Around zero delay, one can see a reduction of the rate to below 1/3 of the rate at long delay. We can fit the rate by a convolution of a normal distribution
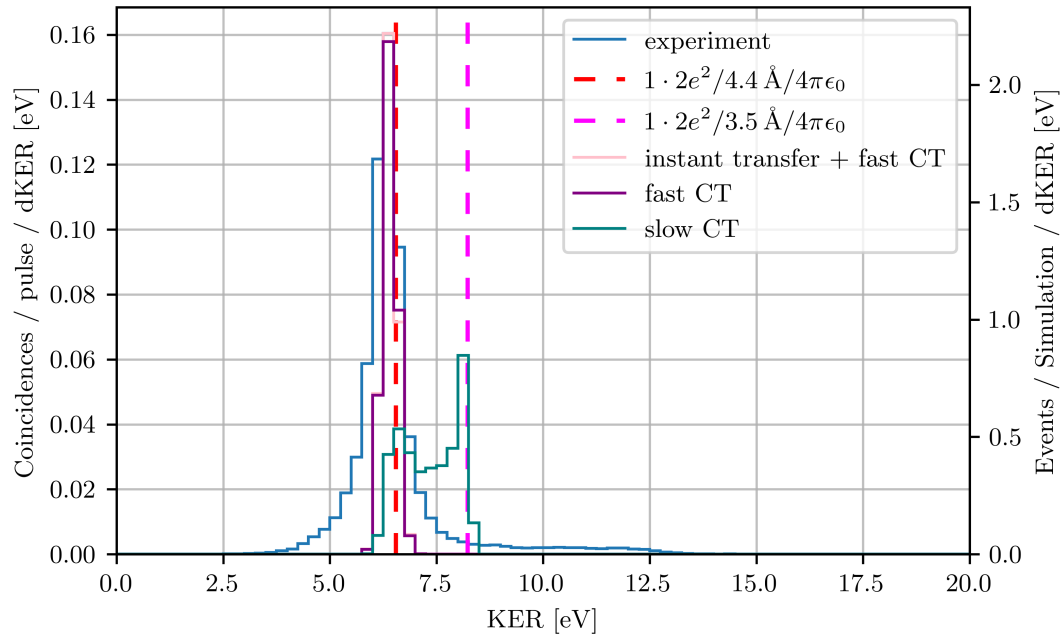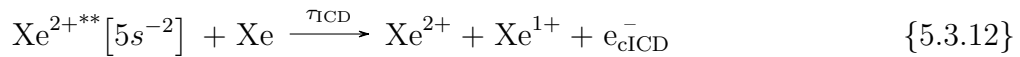
Figure 5.3.9: Distribution of simulated KER values of ^{129}Xe^{1+} / ^{129}Xe^{2+} in comparison with the measured distribution.

that describes the pulse duration and a exponential rise function that describes the suppression of the channel towards zero delay

$$Y(t) = \mathcal{N}(t_0, \sigma) * \left(A \exp\left(\frac{t - t_0}{\tau} \right) \right). \tag{5.3.1}$$

The convolution is calculated numerically and the opimized parameters are given in Figure 5.3.12. The FEL pulse length is estimated to $\sigma = (51.8 \pm 3.4)\,\mathrm{fs}$ and the time constant is estimated to $\tau = (186 \pm 6)\,\mathrm{fs}$.

$$\mathrm{Xe}\!\cdots\!\mathrm{Xe} + \hbar\omega \longrightarrow \mathrm{Xe}^{2+**}\left[5s^{-2}\right] + \mathrm{Xe} + e^-_{\mathrm{PI}} + e^-_{\mathrm{AMD}} \qquad \{5.3.11\}$$

$$\mathrm{Xe}^{2+**}\left[5s^{-2}\right] + \mathrm{Xe} \xrightarrow{\tau_{\mathrm{ICD}}} \mathrm{Xe}^{2+} + \mathrm{Xe}^{1+} + e^-_{\mathrm{cICD}} \qquad \{5.3.12\}$$

The signature that would clearly identify the cICD process is the energy of the e^-_{cICD} electron. As only the two ions and the electron are products of the reaction, the sum of their energy must be constant. When measured in coincidence one would expect that the electron gets less kinetic energy when the KER is increased.
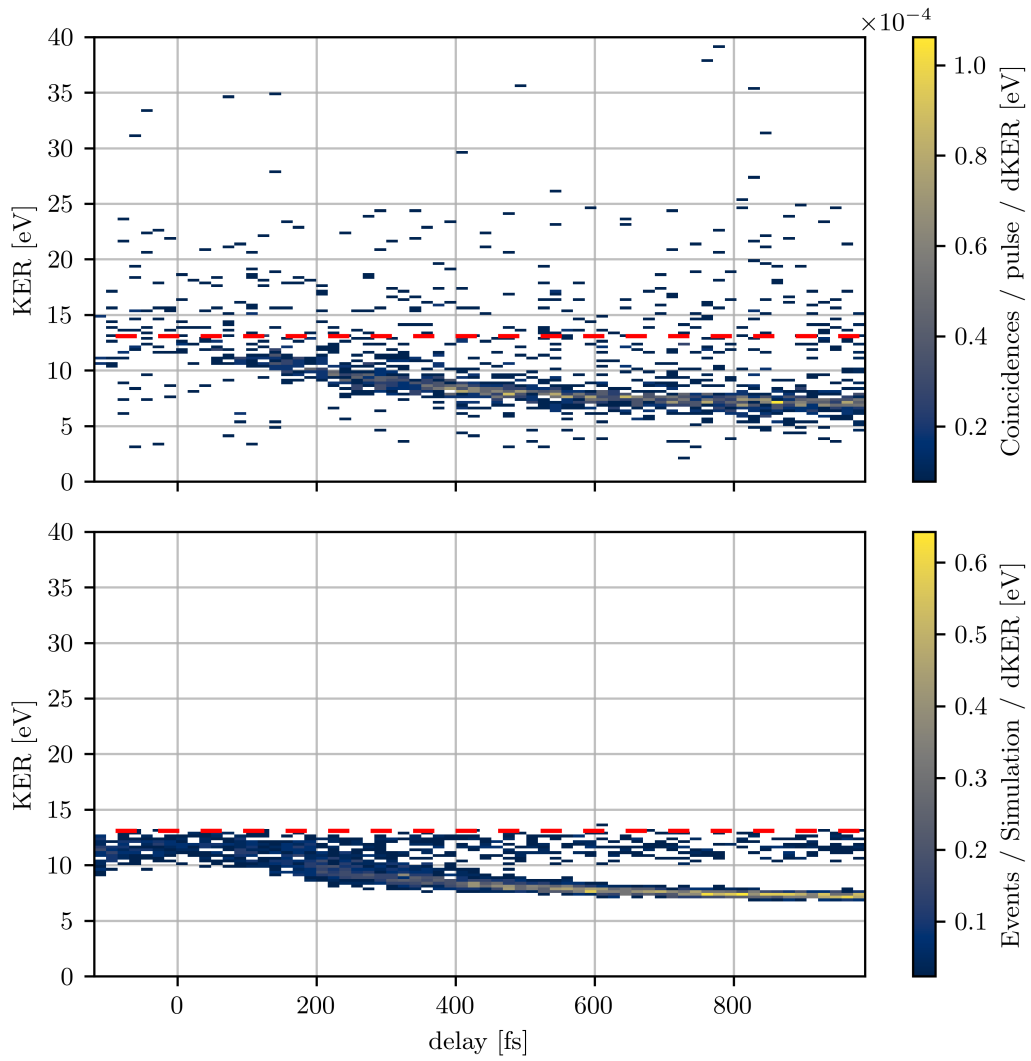
Figure 5.3.10: Distribution of KER values of $^{129}\text{Xe}^{1+}$ / $^{129}\text{Xe}^{4+}$ in dependence of the delay. The top panel shows experimental data, the bottom panel shows simulated data with the fast CT scenario.
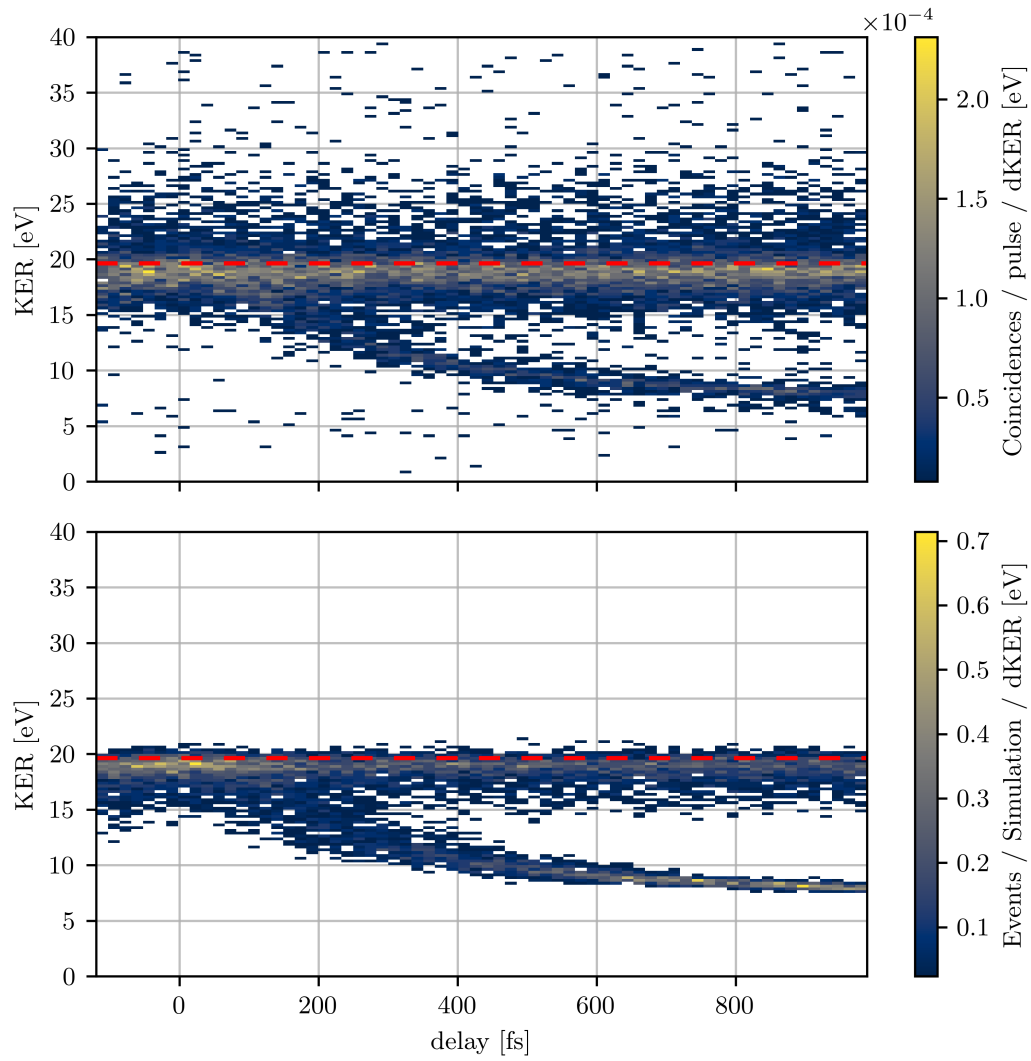
Figure 5.3.11: Distribution of KER values of $^{129}Xe^{2+}$ / $^{129}Xe^{3+}$ in dependence of the delay. The top panel shows experimental data, the bottom panel shows simulated data with the fast CT scenario.
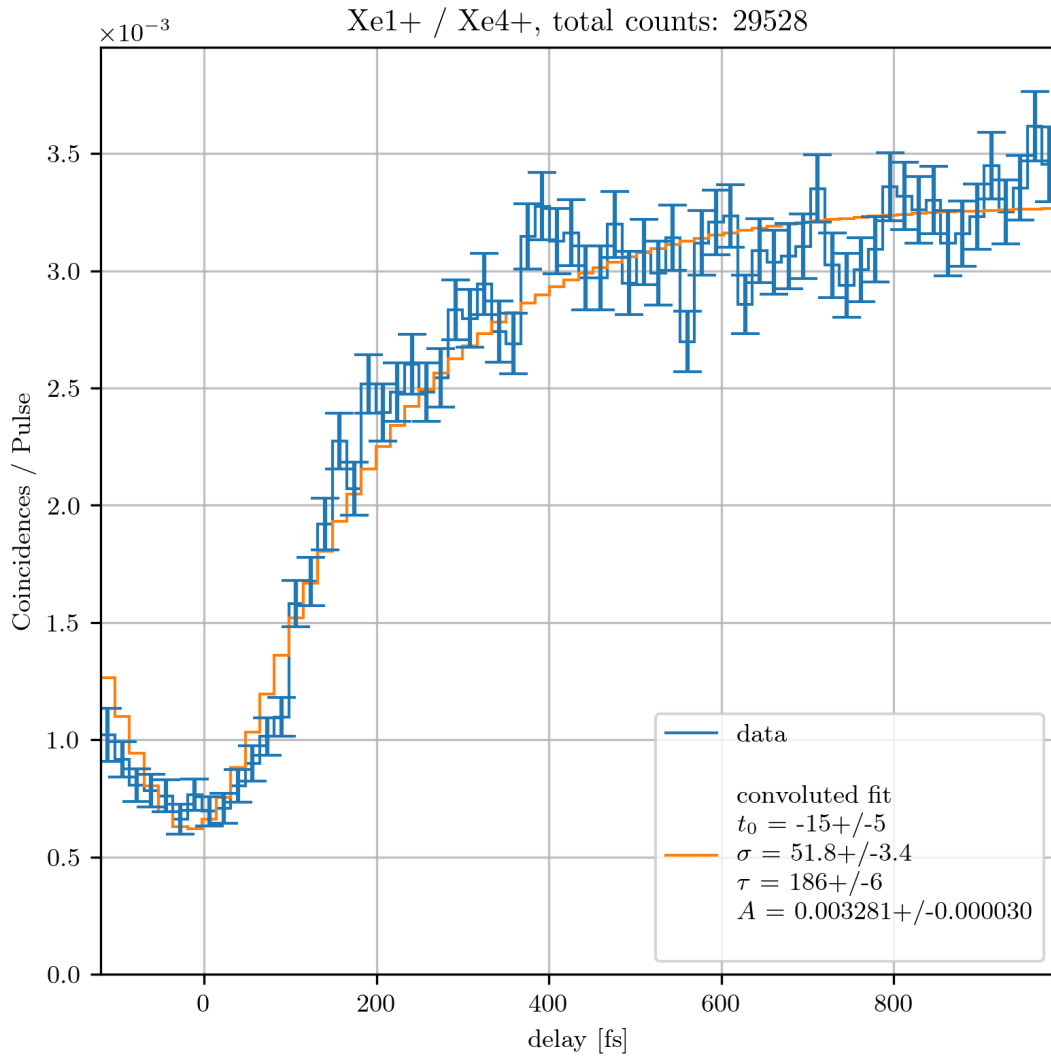
Figure 5.3.12: Fit of Equation (5.3.1) of the event rate of the Xe^{1+} / Xe^{4+} channel. We do not consider different isotopes, as the event rate integrates over all energies and we do not lose anything by reduced momentum or energy resolution.

However, the amount of statistics at hand and the electron energy resolution is insufficient to observe this signature, see Figure 5.3.13.
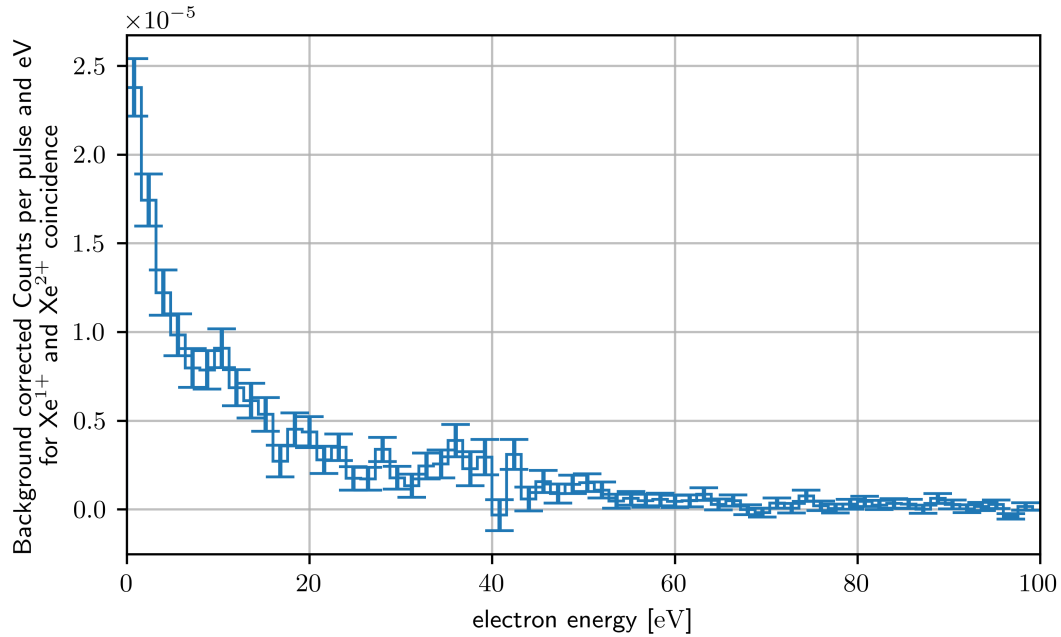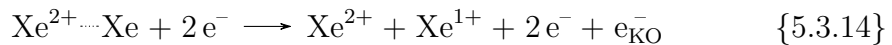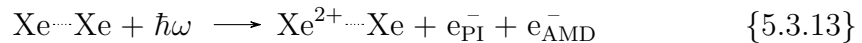

Figure 5.3.13: Distribution of electron energies in correlation with the Xe^{1+} / Xe^{2+} channel. The highest rate is at zero energy, where electrons from double AMD appear. There are faint hints to peaks around $40\,eV$ and shoulder peaks between the $0\,eV$ and $40\,eV$ peaks. The photoelectron is expected around $36\,eV$ and lines from single AMD between $8\,eV$ and $36\,eV$[64].
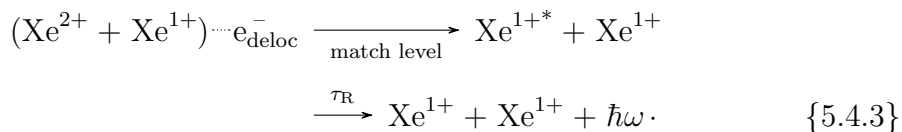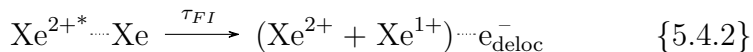
Besides cICD, we can get additional Xe^{1+} / Xe^{2+} events by the ETMD(2) channel with similar signatures as with cICD. Or from the KO ionisation, which has a different signature. The KO ionisation requires, that either the photoelectron or the single AMD electron is emitted towards the neutral Xe.

$$Xe\text{---}Xe + \hbar\omega \;\longrightarrow\; Xe^{2+}\text{---}Xe + e_{PI}^- + e_{AMD}^- \qquad \{5.3.13\}$$

$$Xe^{2+}\text{---}Xe + 2\,e^- \;\longrightarrow\; Xe^{2+} + Xe^{1+} + 2\,e^- + e_{KO}^- \qquad \{5.3.14\}$$

This results in a preference of certain emission angles of the electrons with respect to the internuclear axis. This can be seen from the study of Sequential Ionisation (SI) by electron impact, as explained for example in the thesis of Pflüger [65]. However, as with the electron energy in the other channels, we lack in the amount of correlated electrons to be able to see such angular correlations.

5.4 Frustrated Ionisation of Dimers – A small Plasma

The FI process is similar to what we have discussed for CT, but now the excited electron is not in a low excited state, but in a highly excited, delocalized state. These states have spatial distributions which are mainly distributed in a volume that encloses both of the nuclei and thus does not provide screening of the electric potential between the nuclei. This leads to an increased electrostatic repulsion on the nuclei although the electron is still bound to the system. The behaviour of FI was observed before, e.g. in Ar_2 dimers [66] or larger clusters of Ar, where it is closely connected to the formation of a nanoplasma [67]. The simplest case is the frustrated triple ionisation

$$Xe\text{----}Xe + \hbar\omega \longrightarrow Xe^{2+^*}\text{----}Xe + 2\,e^-_{free} \qquad \{5.4.1\}$$

$$Xe^{2+^*}\text{----}Xe \xrightarrow{\ \tau_{FI}\ } (Xe^{2+} + Xe^{1+})\text{----}e^-_{deloc} \qquad \{5.4.2\}$$

$$(Xe^{2+} + Xe^{1+})\text{----}e^-_{deloc} \xrightarrow[\text{match level}]{} Xe^{1+^*} + Xe^{1+}$$

$$\xrightarrow{\ \tau_R\ } Xe^{1+} + Xe^{1+} + \hbar\omega\,\cdot \qquad \{5.4.3\}$$

Here, the initial steps are local ionization of a 4d inner-valence electron followed by single AMD that leaves the ion in an excited state. If the excitation would be high enough to provide enough energy for both the ionisation potential of the neutral and the energy to overcome the Coulomb potential between the ions, one would now expect ICD to happen. But when we are in the energy region between the monomer ionisation potential and the threshold for ICD, we can give an electron of the neutral atom enough energy to leave its atom, but just not enough to escape the electrostatic potential of the whole system. After that excitation happened, the nuclear part of the system reacts with CE, like two ions would do, but still with an overall bond to the electron, as in Reaction {5.4.2} and Figure 5.4.1. At some point, the nuclei will be so far apart that they do not form a common potential well anymore and the electron will be back to the CT-like situation. Most likely, it will stick to the higher-charged ion as it can access a higher phase space volume at the same energy there. Finally at some point there will be emission of a photon by RD.
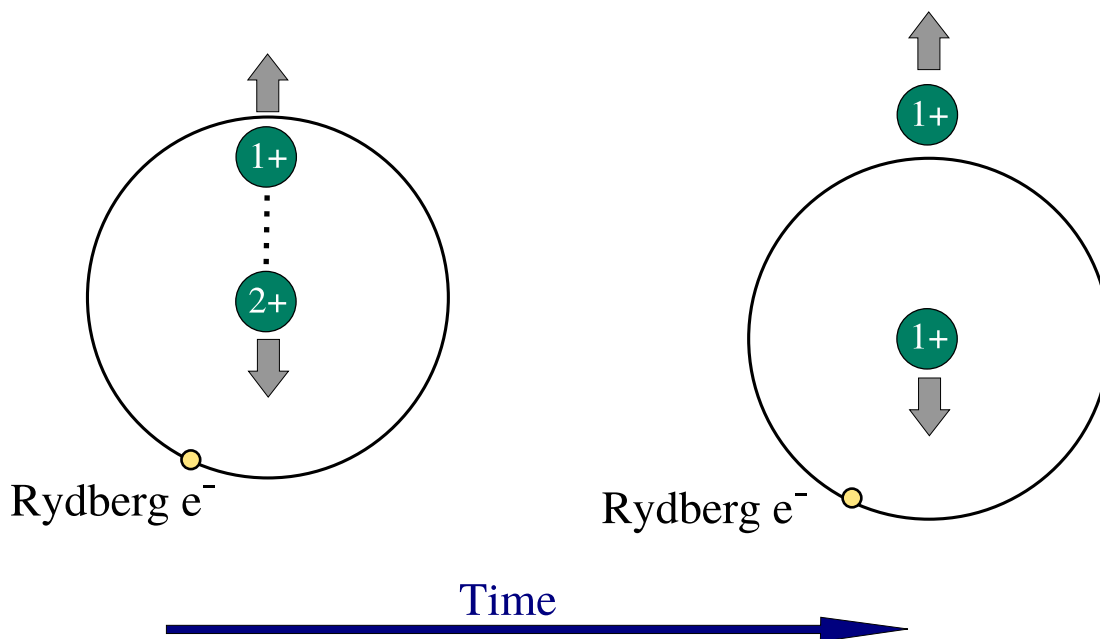
Figure 5.4.1: Sketch of Frustrated Ionisation (FI), Image taken from Schmid [22] with permission.

The experimental signature is a significant increase in the KER compared to the value expected from the measured charge states. As the ions repel as if there was a higher charge state, the effect is up to a factor of two in the Xe^{1+} / Xe^{1+} channel, see Figure 5.4.2. The event rate for this process does not form a peak, but rather forms a plateau between the main peak from the regular ionisation into this channel and the KER values that we would expect from the next ionisation levels. Once the KER is even higher, the plateau ends and the rate drops exponentially. This plateau and cut-off feature is especially pronounced in the Xe^{1+} / Xe^{2+} channel, see Figure 5.4.3. This effect of FI is seen in both asymmetric and symmetric charge distribution without qualitative difference, for example in comparison of the Xe^{1+} / Xe^{3+} and Xe^{2+} / Xe^{2+} channels, see Figures 5.4.4 and 5.4.5.

Figure 5.4.2: Distribution of KER in the ^{129}Xe^{1+} / ^{129}Xe^{1+} channel. The vertical lines mark the expected values given by the Coulomb potential of the respective charge product and distance.
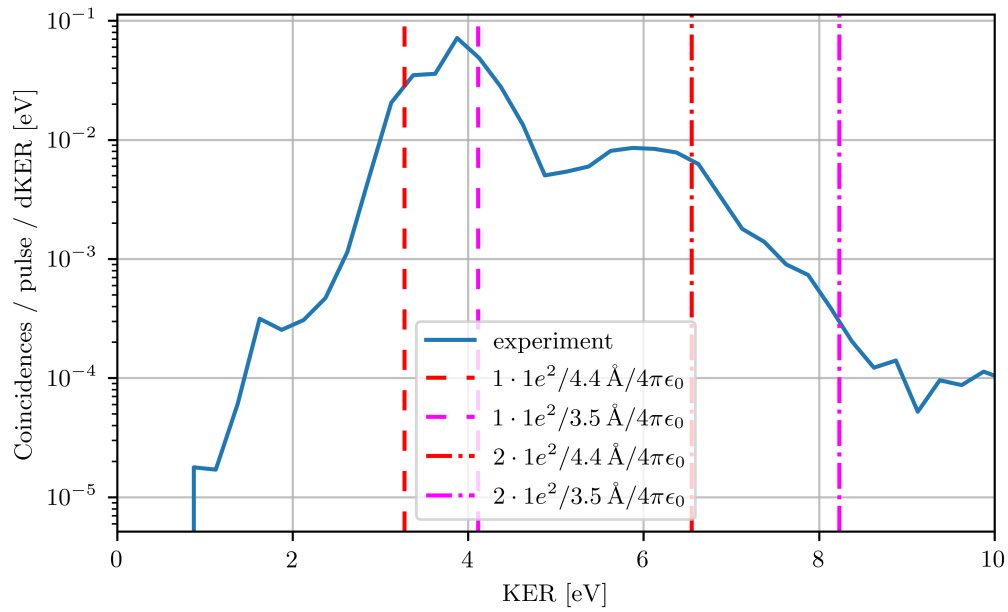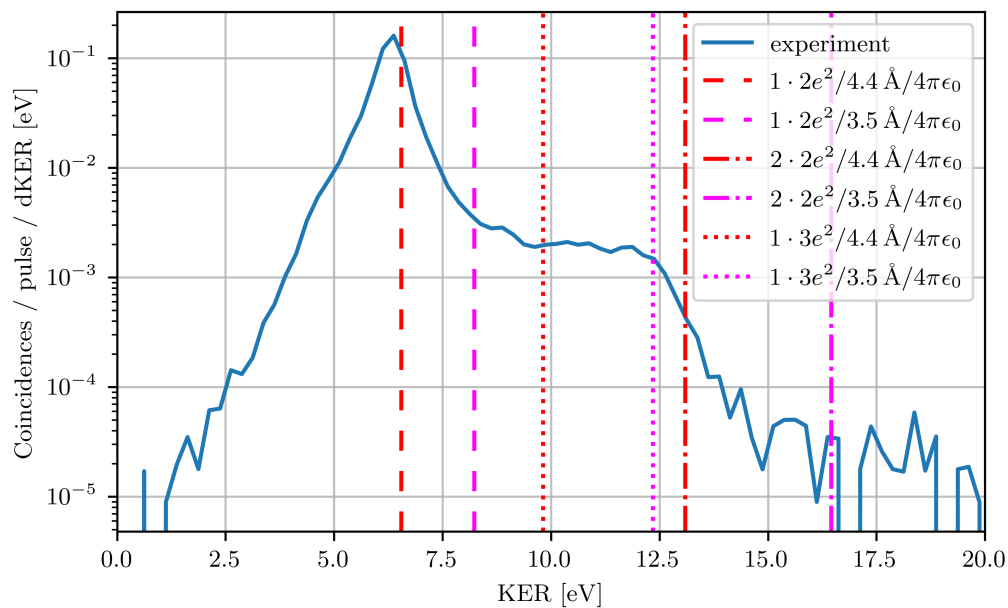

Figure 5.4.3: Distribution of KER in the ^{129}Xe^{1+} / ^{129}Xe^{2+} channel. The vertical lines mark the expected values given by the Coulomb potential of the respective charge product and distance.

Figure 5.4.4: Distribution of KER in the $^{129}Xe^{1+}$ / $^{129}Xe^{3+}$ channel. The vertical lines mark the expected values given by the Coulomb potential of the respective charge product and distance.

Figure 5.4.5: Distribution of KER in the $^{129}Xe^{2+}$ / $^{129}Xe^{2+}$ channel. The vertical lines mark the expected values given by the Coulomb potential of the respective charge product and distance.
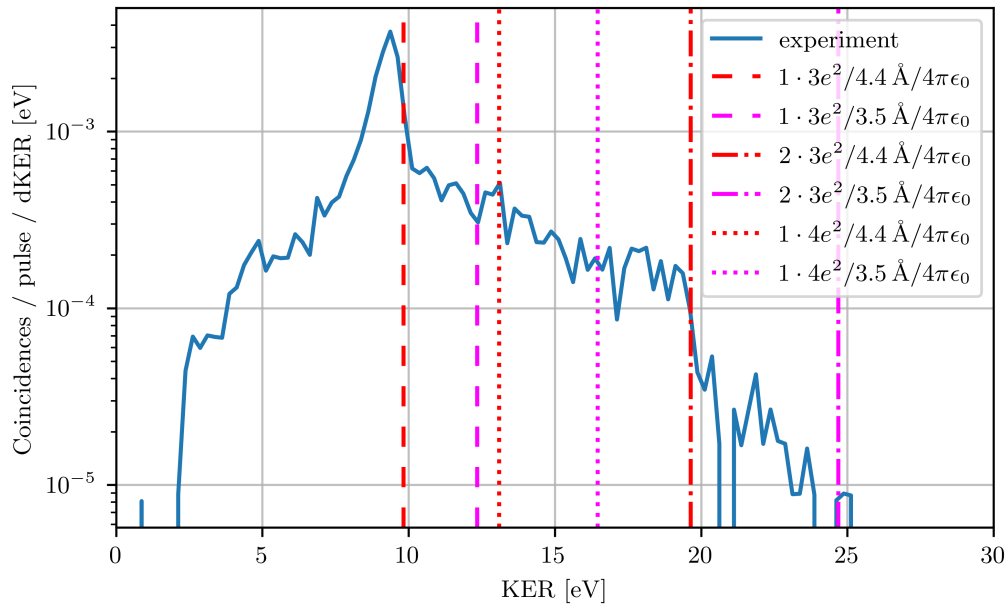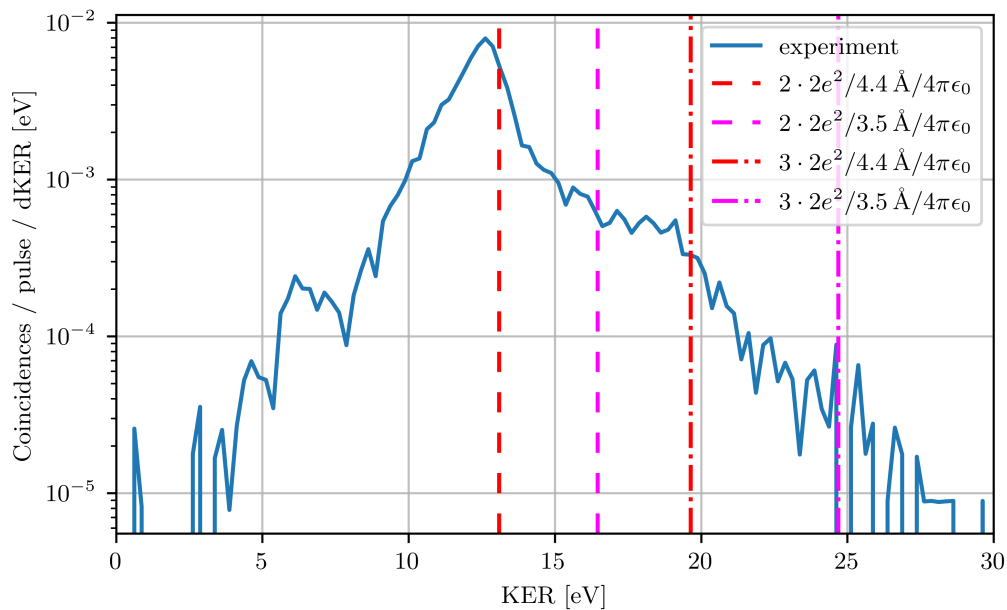
5.5 Correlated Exchange of Electron and Photon between three Atoms by Electron Transfer Mediated Decay

In this Section we look at the mechanism that leads to CE of a Xe_3 trimer into three singly charged Xe^{1+} ions. We observe in Figure 5.5.1 that the final kinetic energy matches what we expect from a triangular configuration with all sides as long as the inter-nuclear distance in dimers. Comparing the different simulation
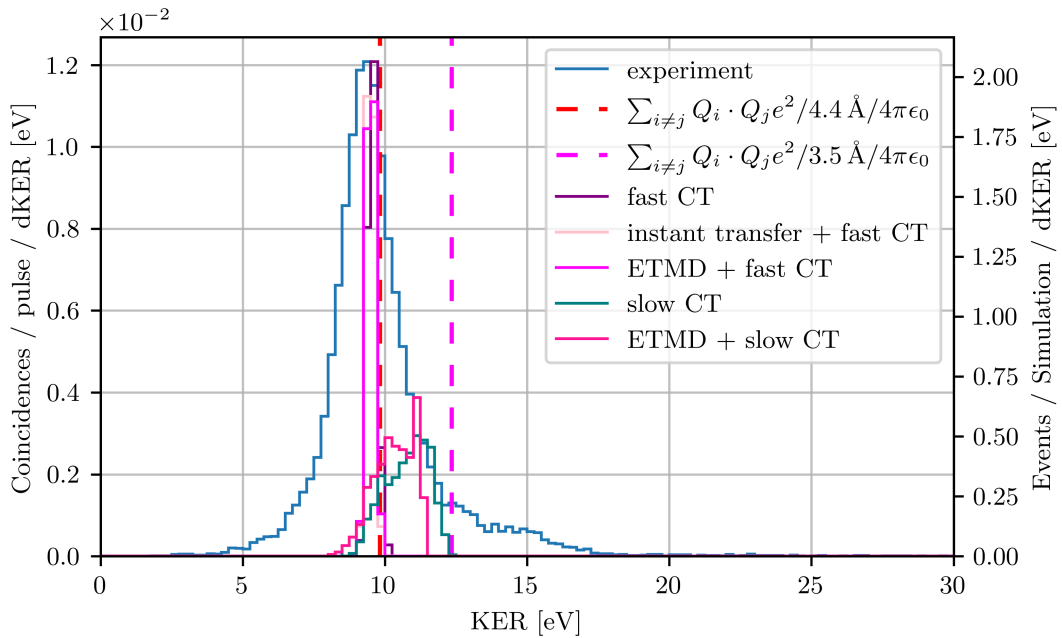
Figure 5.5.1: Distribution of KER in the $^{129}Xe^{1+}$ / $^{129}Xe^{1+}$ / $^{129}Xe^{1+}$ channel. The experimental data is shown in blue, the horizontal dashed lines represent the expected values by the Coulomb potential energy, the other curves show the resulting distributions from the different simulation scenarios.

scenarios with the experimental data, we can see that the slow CT with or without ETMD(3) both shift the distribution towards high KER. As that is not observed, the experimental KER tells us that we have to consider the relatively fast processes. It can be either the independent sequential CT from the two neutral Xe atoms to

a Xe^{3+} with the steps being

$$Xe \atop \quad \diagdown \atop Xe \diagup \quad Xe + \hbar\omega \longrightarrow \quad {Xe \atop \quad \diagdown \atop Xe \diagup} \quad Xe^{3+} + 3\,e^{-} \qquad \{5.5.1\}$$

$$\quad {Xe \atop \quad \diagdown \atop Xe \diagup} \quad Xe^{3+} \xrightarrow{\tau_{ct}} Xe^{2+*} + Xe^{1+} + Xe$$

$$\xrightarrow{\tau_{R}} Xe^{2+} + Xe^{1+} + Xe + \hbar\omega \qquad \{5.5.2\}$$

$$Xe^{2+*} + Xe^{1+} + Xe \xrightarrow[R < R_c]{\tau_{ct}} Xe^{1+*} + Xe^{1+} + Xe^{1+}$$

$$\xrightarrow{\tau_{R}} Xe^{1+} + Xe^{1+} + Xe^{1+} + \hbar\omega\,. \qquad \{5.5.3\}$$
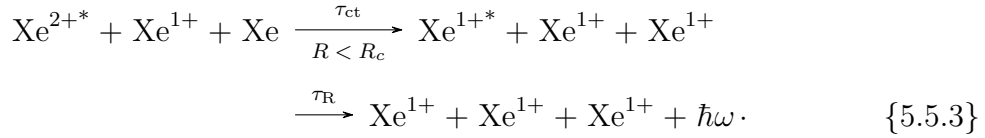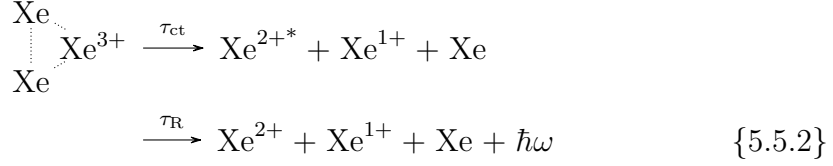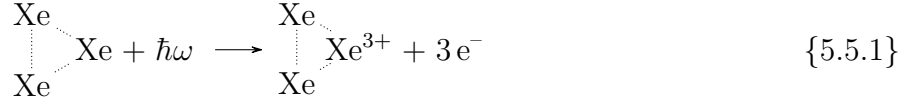
In this chain of reactions, the second charge transfer can only happen when the neutral is still close enough to the doubly-charged ion. Alternatively, it can be through the ETMD(3) process with a correlated step that combines CT from one of the neutrals with an ICD-like ionisation of the other neutral
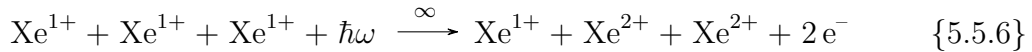
$$Xe \atop \quad \diagdown \atop Xe \diagup \quad Xe + \hbar\omega \longrightarrow \quad {Xe \atop \quad \diagdown \atop Xe \diagup} \quad Xe^{2+} + 2\,e^{-} \qquad \{5.5.4\}$$

$$\quad {Xe \atop \quad \diagdown \atop Xe \diagup} \quad Xe^{2+} \xrightarrow{\tau_{ETMD3}} Xe^{1+} + Xe^{1+} + Xe^{1+} + e^{-}_{ETMD3}\,. \qquad \{5.5.5\}$$
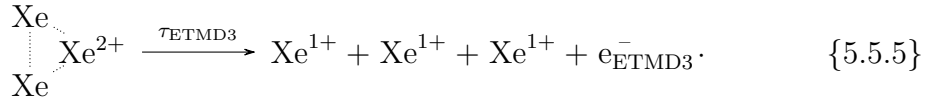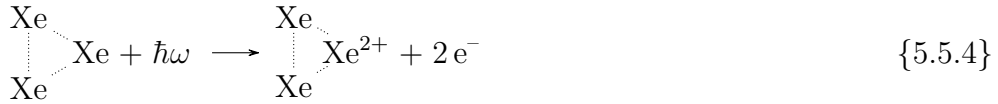
To find the time scale of either process, we look at the probe of the system with another photon and thereby the placement of two additional charges. The probed states are either with distributed charges

$$Xe^{1+} + Xe^{1+} + Xe^{1+} + \hbar\omega \xrightarrow{\infty} Xe^{1+} + Xe^{2+} + Xe^{2+} + 2\,e^{-} \qquad \{5.5.6\}$$

or in case the ions are already far apart without further charge distribution

$$Xe^{1+} + Xe^{1+} + Xe^{1+} + \hbar\omega \xrightarrow{\infty} Xe^{1+} + Xe^{1+} + Xe^{3+} + 2\,e^{-}\,. \qquad \{5.5.7\}$$
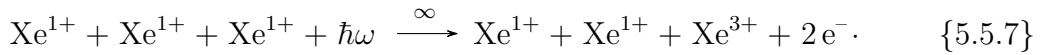
We see in Figure 5.5.2 the pump-probe signature of the dissociating Xe^{1+} / Xe^{1+} / Xe^{3+} system. At short delay, the channel is suppressed. With increasing delay, the event rate rises in a band of decreasing KER. That band converges to $10\,eV$,

the KER value that we observed in Xe^{1+} / Xe^{1+} / Xe^{1+}. In the corresponding

Figure 5.5.2: Xe^{1+} / Xe^{1+} / Xe^{3+} ETMD(3), note that we compare here with experimental data, that includes all isotopes. This reduces the resolution in the KER, but otherwise it would not be enough statistics to see delay dependence.

Figure 5.5.3 for the distributed Xe^{1+} / Xe^{2+} / Xe^{2+} channel, we do not see clear delay-dependent signatures in the measurement and in the simulation, we see events only around the KER for the equilibrium distance. As there is no signature of fragmentation, we can assume, that Xe^{1+} / Xe^{2+} / Xe^{2+} is only produced at very short delay, when the nuclei have not moved significantly.

Figure 5.5.3: Xe^{1+} / Xe^{2+} / Xe^{2+} ETMD(3), note that we compare here with experimental data, that includes all isotopes. This reduces the resolution in the KER, but otherwise it would not be enough statistics to see delay dependence.
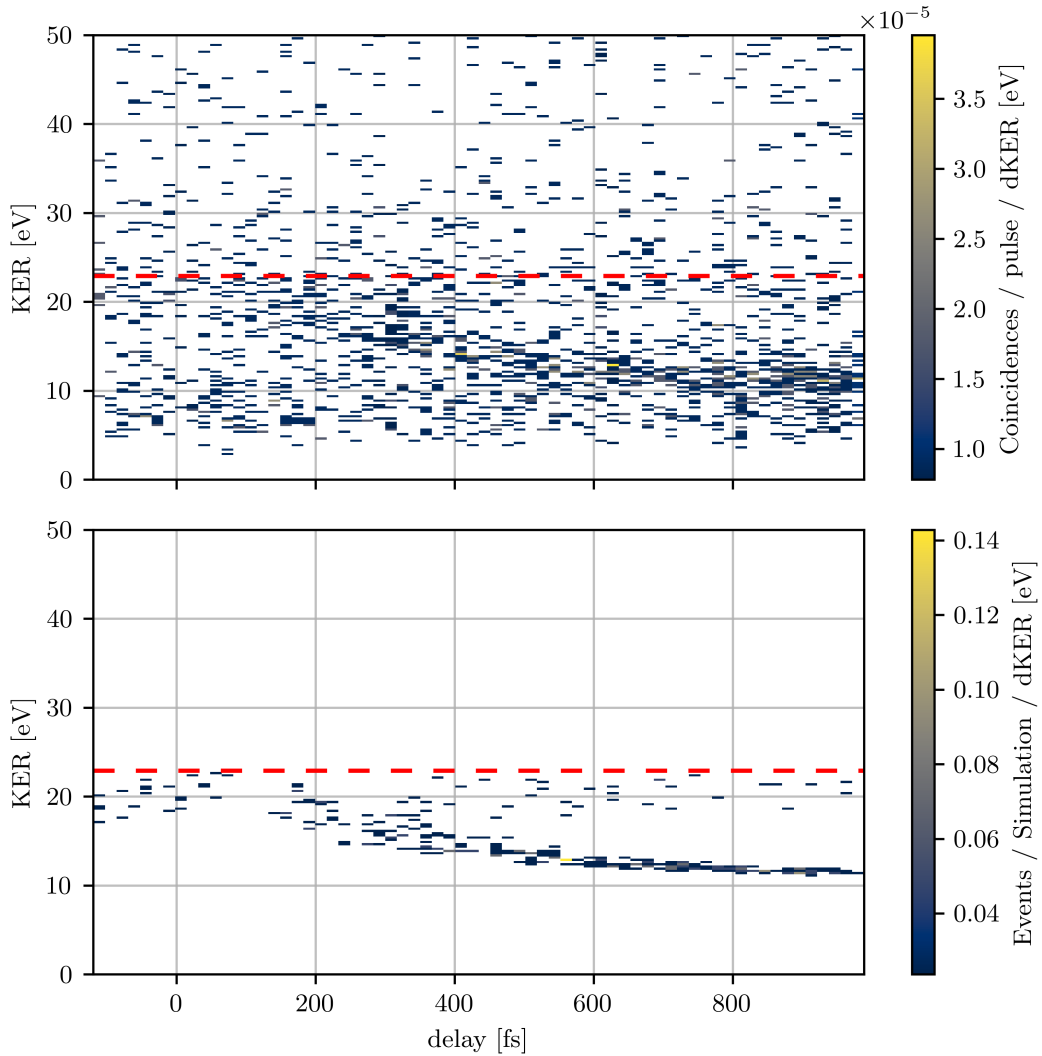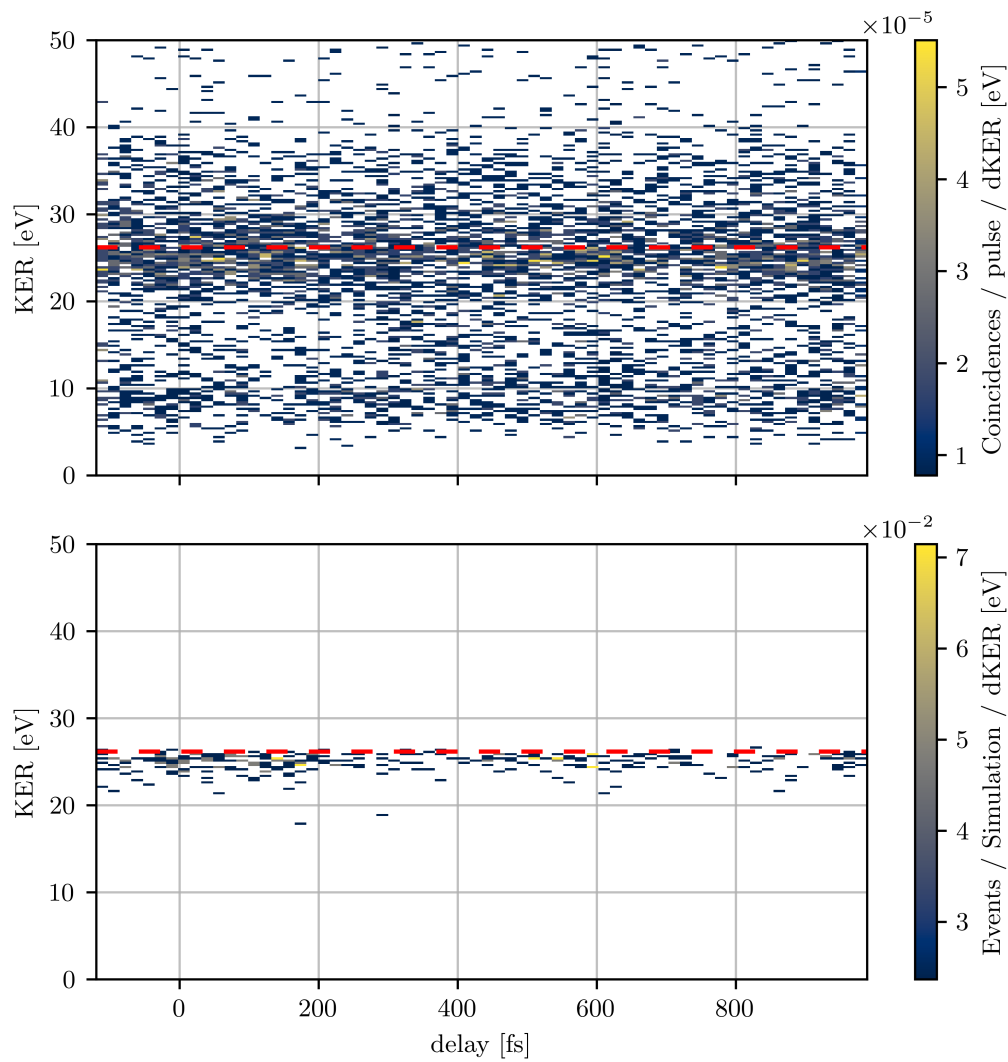
Figure 5.5.4: Xe^{1+} / Xe^{2+} / Xe^{2+} ETMD(3), note that we compare here with experimental data, that includes all isotopes. This reduces the resolution in the KER, but otherwise it would not be enough statistics to see delay dependence.
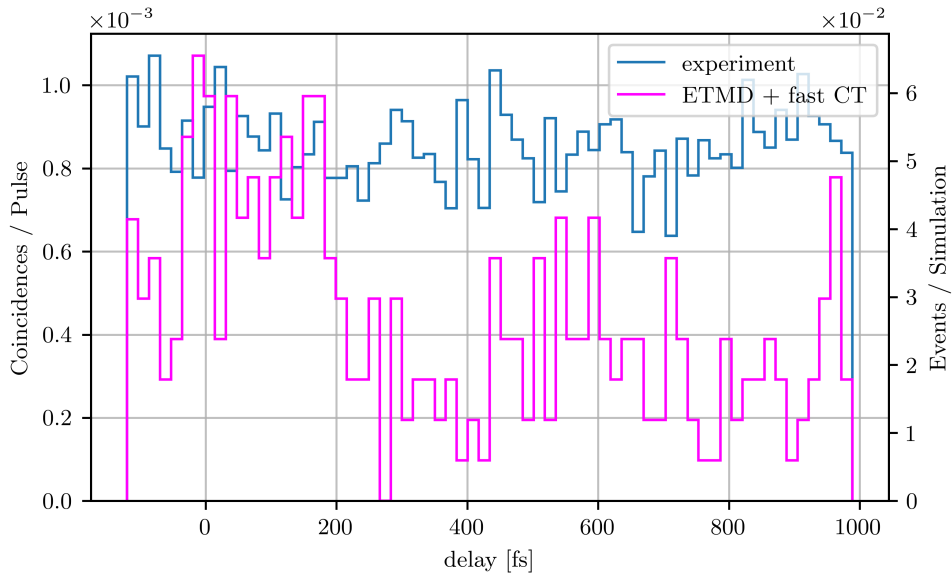
Indeed the simulation shows an increased rate for Xe^{1+} / Xe^{2+} / Xe^{2+} at zero delay, which is not evident in the experimental data. We can estimate the timescale for ETMD(3) from the experimental data with a fit like Equation (5.3.1) in Section 5.3.2. However the count rate for this channel is very low although we take all isotopes into account. In total there are less than 1500 events in the range with the delay-dependent signal from 8 eV to 25 eV across all delay values. Therefore we have to restrict the fit such that it takes the pulse length from the previous fit on the dimer signal (51.8 ± 3.4) fs, see Section 5.3. So we require that the fit uses a value within the range of 41.6 fs to 62 fs for the pulse length. Under this constrained fit, we get a value of $\tau_{\mathrm{ETMD3}} = (84 \pm 13)$ fs.

To distinguish if we observed CT or ETMD(3), we can look at the distribution of energy among the three ions, the Dalitz plot Figure 5.5.6. In that representation of energy sharing we see a clear peak in the centre. The centre point corresponds to exactly equal sharing of kinetic energy between the three ions. The measurement is distributed around this point. That tells us that there can not be much time between the point where the second and the third ion is charged. Otherwise, the first and second ion would gather momentum that the third would not be

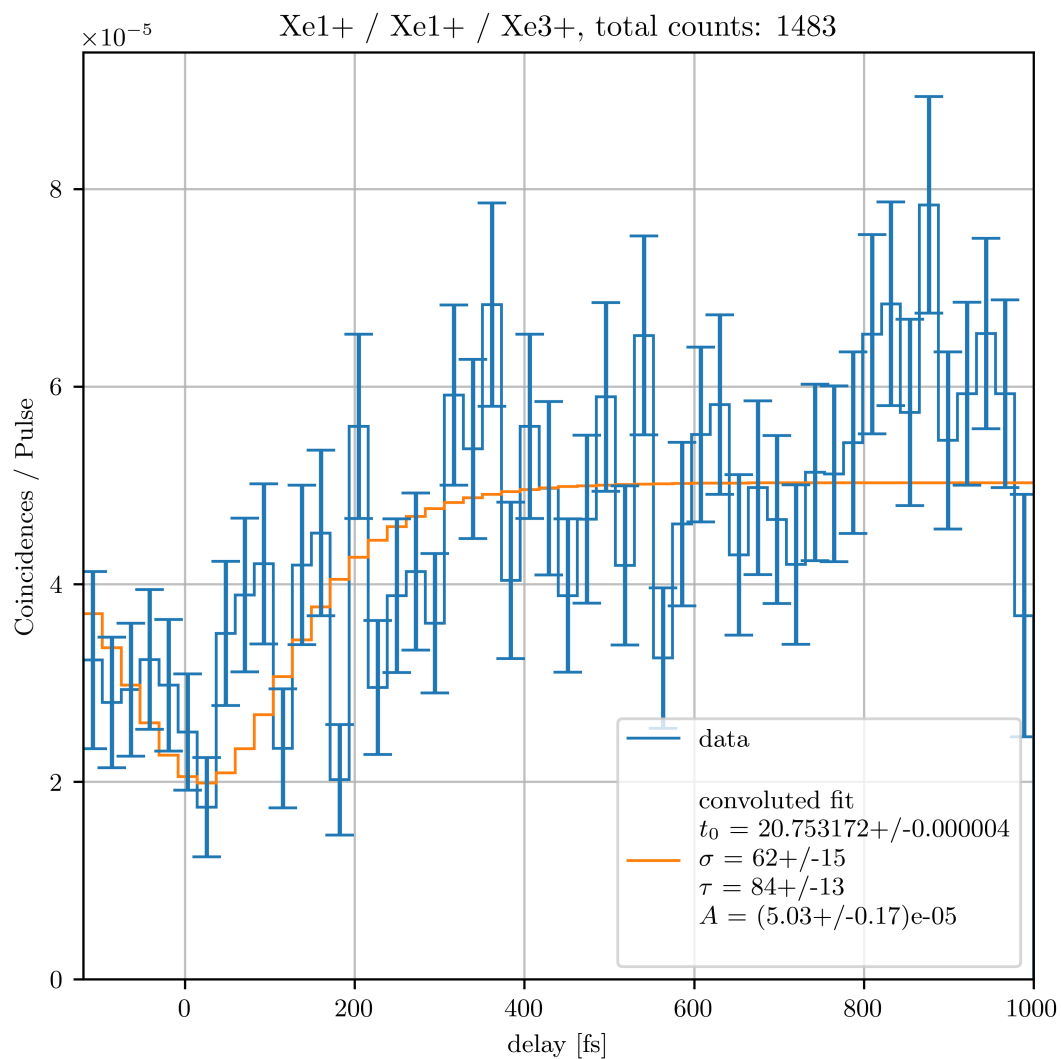Figure 5.5.5: Fit of Equation (5.3.1) of the event rate of the Xe^{1+} / Xe^{1+} / Xe^{3+} channel. We do not consider different isotopes, as the event rate integrates over all energies and we do not lose anything by reduced momentum or energy resolution.
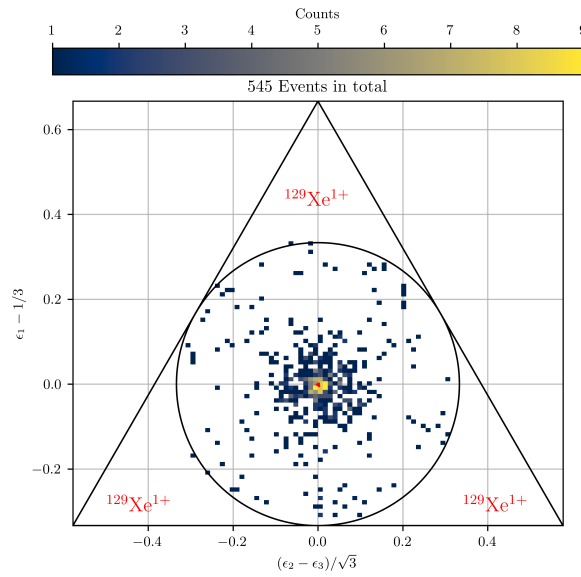
Figure 5.5.6: Dalitz plot of the experimental data from the $^{129}\text{Xe}^{1+}$ / $^{129}\text{Xe}^{1+}$ / $^{129}\text{Xe}^{1+}$ channel. For explanation of the Dalitz plot, see Section 3.2.2.

able to get afterwards. When we compare the measurement to the results from the fast CT and ETMD(3) simulations in Figures 5.5.7 to 5.5.9, this gives us a strong indication for the ETMD(3) process. The Dalitz plot of the CT produces a very pronounced star structure. This arises as the CE between two ions starts immediately after the first CT, but the CE between the third ion and the other two starts only when the second CT happend. At that point those two other ions are already further away and the Coulomb potential is reduced. When we compare the two ETMD(3) scenarios, the fast one produces an energy sharing that is too close to the centre. The slower scenario seems to reproduce the experimental data better although the KER distribution in Figure 5.5.1 was better reproduced by the fast ETMD(3) process.

As it is hard to judge the 2D-Histograms even qualitatively, we reduce the dimensionality by a change to spherical coordinates around the centre of the Dalitz plot and integrate over the angular part. The result is shown in Figure 5.5.10. In this representation we get zero when the energy is shared equally between all 3 particles and we will get 1/3 when either one particle gets zero energy and the others each 1/2 or when one particle gets the maximum of 2/3 of the total energy and the others each get 1/6. So this metric measures the distance to an equal

Figure 5.5.7: Dalitz plot of the the $^{129}Xe^{1+}$ / $^{129}Xe^{1+}$ / $^{129}Xe^{1+}$ channel from the
fast CT simulation scenario. For explanation of the Dalitz plot, see Section 3.2.2.

Figure 5.5.8: Dalitz plot of the the $^{129}Xe^{1+}$ / $^{129}Xe^{1+}$ / $^{129}Xe^{1+}$ channel from the
fast ETMD(3) + CT simulation scenario. For explanation of the Dalitz plot, see
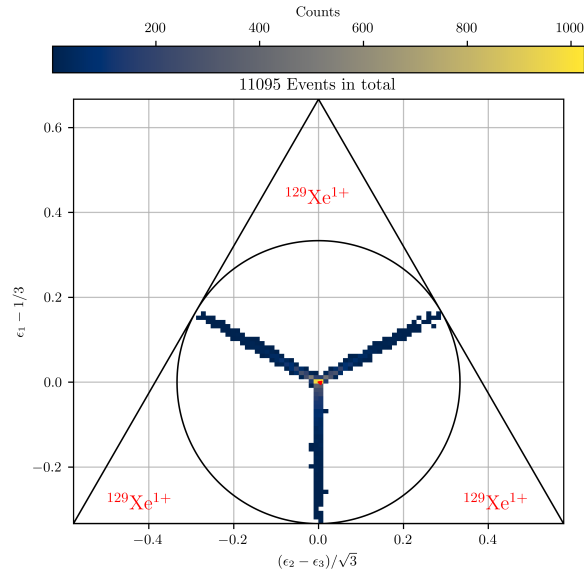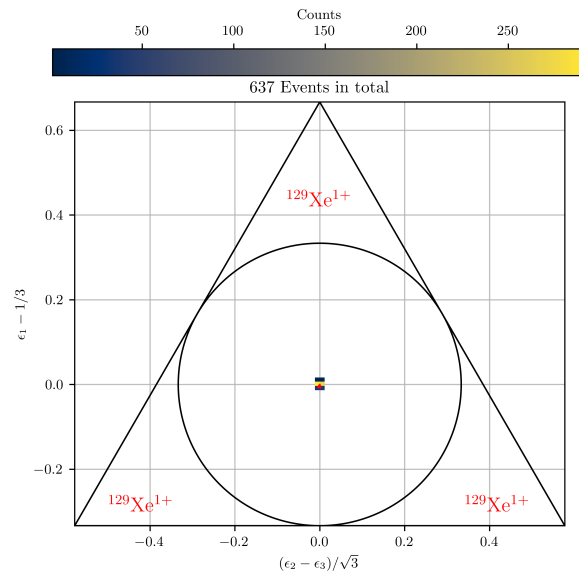Section 3.2.2.
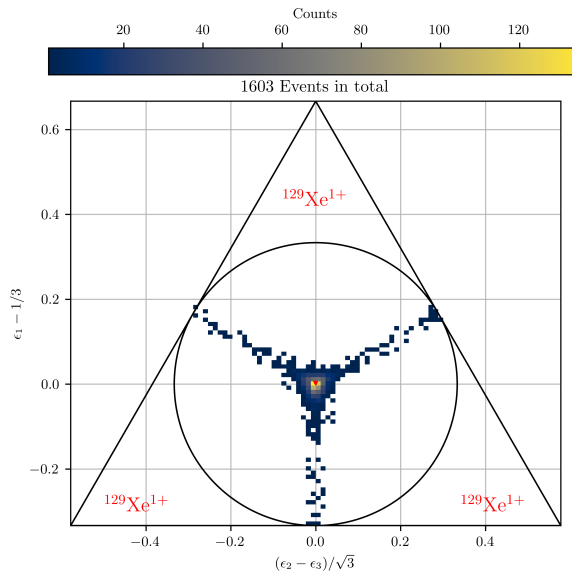
Figure 5.5.9: Dalitz plot of the the $^{129}\text{Xe}^{1+}$ / $^{129}\text{Xe}^{1+}$ / $^{129}\text{Xe}^{1+}$ channel from the slow ETMD(3) + CT simulation scenario. For explanation of the Dalitz plot, see Section 3.2.2.

distribution of energy. It can be calculated directly by

$$\kappa = \left| (\epsilon_2 - \epsilon_3)/\sqrt{3} + i \cdot \epsilon_1 \right|. \tag{5.5.1}$$

Figure 5.5.10a shows the distribution of κ for the experimental data. It features a broad peak in the range from 0.0 to 0.12, a smaller peak around 0.3 and a noisy plateau in between. The simulated data in Figure 5.5.10b for the fast ETMD(3) shows a sharp peak at zero without any events at higher values. It clearly overestimates the symmetry of energy distribution. The slow ETMD(3) shows a broader peak together with a noisy tail towards higher values in Figure 5.5.10c. In the simulations without ETMD(3), the resulting distribution of κ seems exponential for fast CT, see Figure 5.5.10d, and uniform for the slow CT, see Figure 5.5.10d. Comparing those distributions, it seems that the simulated scenario of a slow ETMD(3) agrees best with the experimental data from the perspective of the relative energy distribution. However, in the distribution of the absolute KER in Figure 5.5.2, the faster ETMD(3) scenario described the measured energy better. Probably, one would need to find a scenario in between those.

116

(a) Experiment

(b) Fast ETMD + CT

(c) Slow ETMD + CT

(d) Only fast CT

(e) Only slow CT

Figure 5.5.10: Distribution of the energy sharing asymmetry metric for $^{129}\text{Xe}^{1+}$ / $^{129}\text{Xe}^{1+}$ / $^{129}\text{Xe}^{1+}$ in comparison with the experimental data and different simulated scenarios.
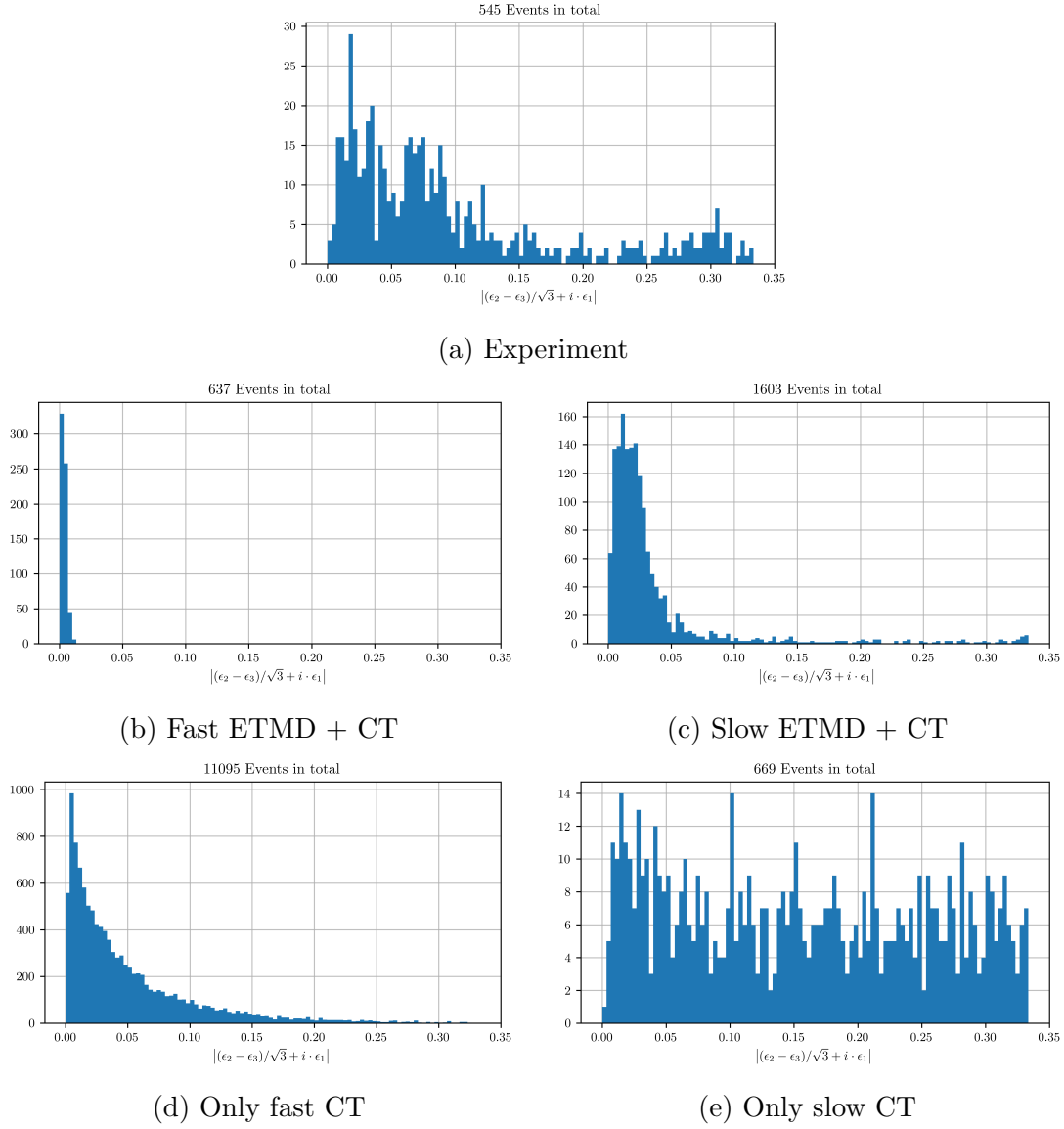
117

Chapter 6

Summary

This thesis presented results of an experiment on the dynamics of processes that distribute charge or energy from a local excitation on a Xe^{*n+} ion to neighbouring atoms in a dimer or trimer of Xe. The Xe clusters were ionised using the Free electron LASer in Hamburg 2 (FLASH2) at a photon energy of $100\,eV$ and the charged fragment's momenta were measured by a REeaction MIcroscope (REMI). The FLASH2 reaction microscope (FlashRemi) endstation provided the capability to measure also with a split beam such that one part can be delayed in time. This allowed a pump-probe measurement that tracks the development of the cluster during the dissociation. In the course of the Xe experiment, the pump-probe capability of the endstation was enabled by development of several procedures to measure and correct for spatial deviations of the focus when scanning the delay mirror. This procedure was further developed in the following beamtimes to allow the calibration more efficiently, using less beamtime.

Summarising the coincident event rates from Xe⋯Xe dimers for reaction channels of total charge of $+3$ and those with a total charge of $+2$ shows, that the higher charge of $+3$ is significantly enhanced in dimers compared to monomers. The ratio of those event rates changes from $1:2$ in monomers to $2:1$ in dimers. This suggests that efficient non-local auto-ionising processes appear starting from the dimer on in small clusters in addition to the double Auger-Meitner Decay (AMD) which can produce Xe^{3+} after absorption of a single photon. In the fragments of Xe_2, the processes' signatures of a slow Charge Transfer (CT) and of Frustrated Ionisation (FI) emerge. In the time-resolved probe of the Xe^{1+} / Xe^{2+} into Xe^{1+} / Xe^{4+}, we could show, that this asymmetric charge distribution

is strongly suppressed at short time delays between pump and probe pulse. The time constant belonging to this suppression was determined to $(186 \pm 6)\,\mathrm{fs}$ for dimers. From the available calculated potential energy curves of $Xe\text{-}Xe^{2+}$ from Liu, Kolorenč and Gokhberg [17], we expected to see Radiative Charge Transfer (RCT), CT or collective Interatomic Coulombic Decay (cICD), depending on the intermediate state the Xe^{2+} after single AMD. Of these processes, only cICD could explain of the third charge in the dimer. However, we could not provide sufficient evidence for the process due to limited resolution in the electron energy and low event rates after correlating the electrons with the Xe^{1+} / Xe^{2+} ion coincidence. Other possible mechanisms, that could explain the third charge are two particle Electron Transfer Mediated Decay (ETMD(2)) or double Interatomic Coulombic Decay (dICD) from the 4d vacancy in $Xe\text{-}Xe^{+}$. Another way is the Knock Off ionisation (KO) process, similar to the single-photon double ionisation process. The initial photoelectron or a following single AMD electron can collide with the neutral Xe while leaving the cluster and ionise the Xe neighbour.

Analysis of the relative energy share in the fragmentation of a Xe_3 into Xe^{1+} / Xe^{1+} / Xe^{1+} shows, that all three ions come out with similar amount of kinetic energy. This indicates a transfer process, where both secondary ionisations occur at the same time. That kind of behaviour is inherent to the three particle Electron Transfer Mediated Decay (ETMD(3)) process, where CT and Interatomic Coulombic Decay (ICD) happen at the same time between an accepting positive ion, an electron donating atom and an third atom, that is ionized by a virtual photon. By probing the system into Xe^{1+} / Xe^{1+} / Xe^{3+}, we find suppression of the channel for delays shorter than $(84 \pm 13)\,\mathrm{fs}$.

The interpretation of experimental data is supported by Monte Carlo simulations of the pump-probe process. The agreement of relations between Kinetic Energy Release (KER) to pump-probe delay and the energy sharing in trimers between experiment and simulation is satisfying on a qualitative level and help to strengthen our interpretations. Further simulations helped with identification of calibration parameters in the analysis of the momentum data. This was important for the analysis, as it allowed to confidently aggregate several measurements and the vast amount of combinations between isotopes and charge states in the ion fragmentation channels.

Outlook In order to resolve the open question on the specific processes that lead to the increased average charge in dimers, further measurements would be helpful. Since the experiment, it became routinely available to perform scans over the photon energy at the FlashRemi endstation. Although this is not feasible to do at the same time as scanning pump-probe delays, a scan in the photon energy dimension at zero delay and at a single long delay can complement the data set with information that can greatly help to identify specific fragmentation channels. Another way to use this, is to actively search for population of excited states, that decay in a certain way, such as the $5s^{-1}$ state, which is expected to decay by CT. Furthermore it would be very helpful to measure more electron data with optimized settings on the spectrometer, again together with either delay or photon energy scans. We expect to find marker lines in the electron energy spectrum for the different relaxation processes. And additionally, when sufficient electron data is collected to examine the angular correlation between the ion fragmentation axis and the electron momenta, one could estimate the amount of triple ionisation by KO processes. The collected statistics could also be used more efficiently in the future, when the selection of isotopes through their momentum sum is considered appropriately. A moderate increase in the momentum resolution could already help to correctly identify a larger fraction of isotope combinations in dimers and trimers. Alternatively, usage of a different isotope composition might help in the same way. From theory side, it might be promising to further investigate the decay chain of $Xe\text{---}Xe^{+*}$ into triply charged Xe^{1+} / Xe^{2+} fragments. Especially due to the cICD process from the doubly excited $5s^{-2}$ $Xe\text{---}Xe^{2+}$ state. Most importantly, it would be helpful to identify the expected energy of the cICD electron. It might well be, that it is hidden behind the event rate of the direct photoelectron at $100\,\text{eV}$ photon energy.

Appendix A

Momentum Calibration Metrics

This Appendix shows the histograms that are used as optimisation metrics in the momentum calibration model of Section 3.3.5.
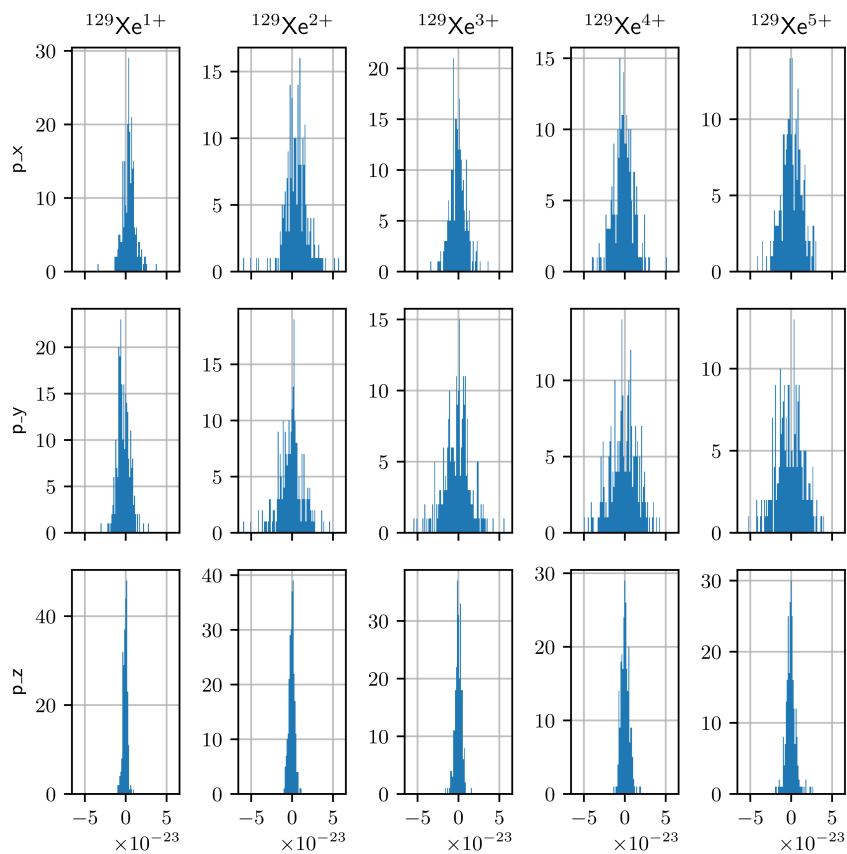
Figure A.1: The monomer ion momenta should all be around zero. Therefore we score the deviation from zero for all momentum components.
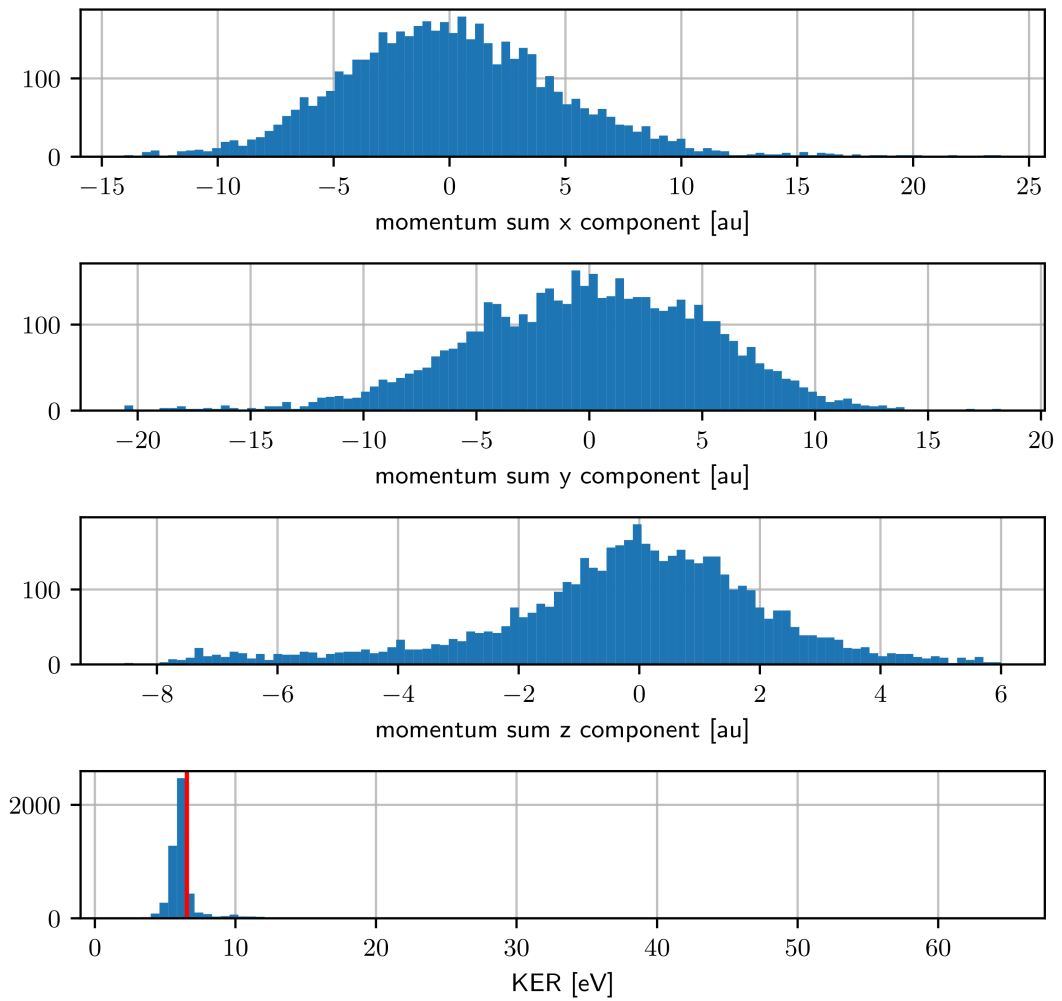
Figure A.2: The momentum sum is evaluated to calculate the target temperature and a penalty score is calculated by the distance between the median momentum sum and 0 for each component.
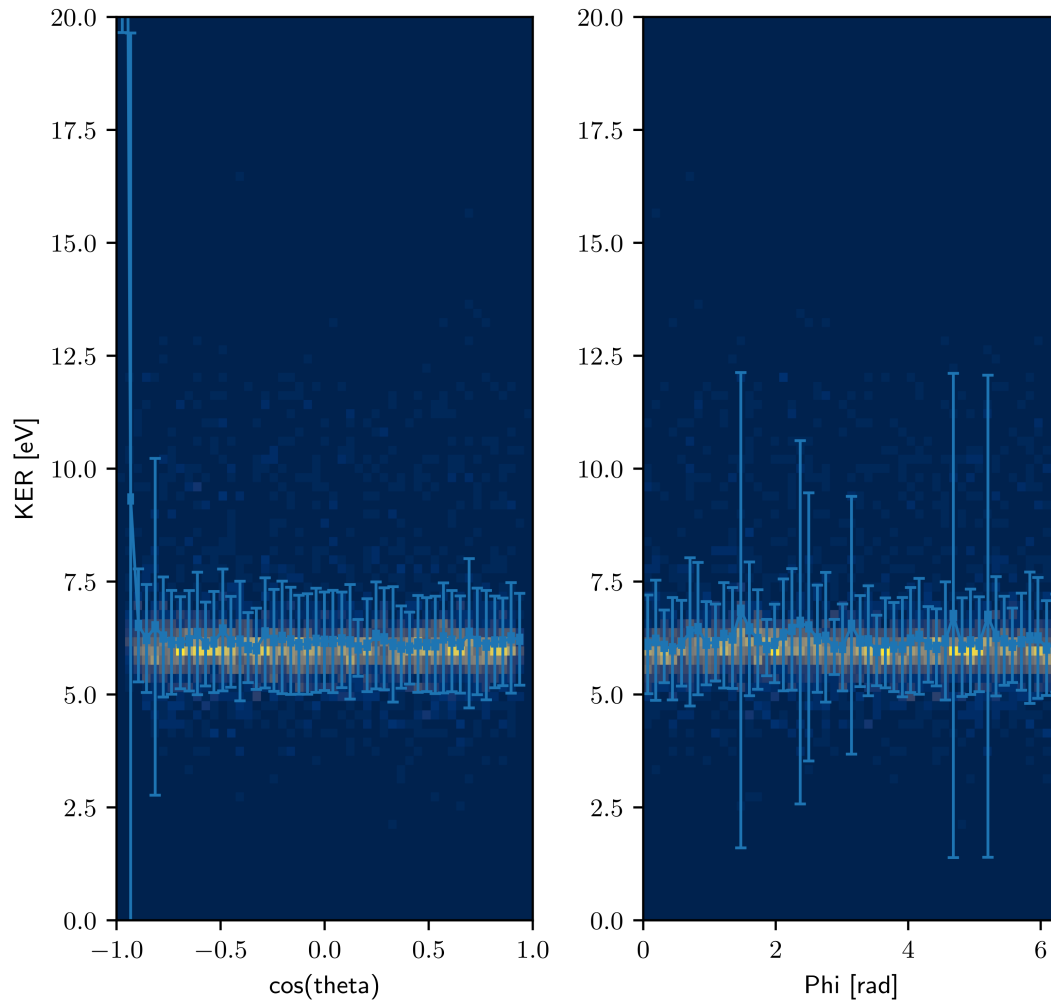
Figure A.3: The calculated distribution of the KER is required to be as constant with respect to the two spherical angles as possible. The corresponding penalty score is calculated by the variance of the mean KER for each bin and the average width of the KER distribution.
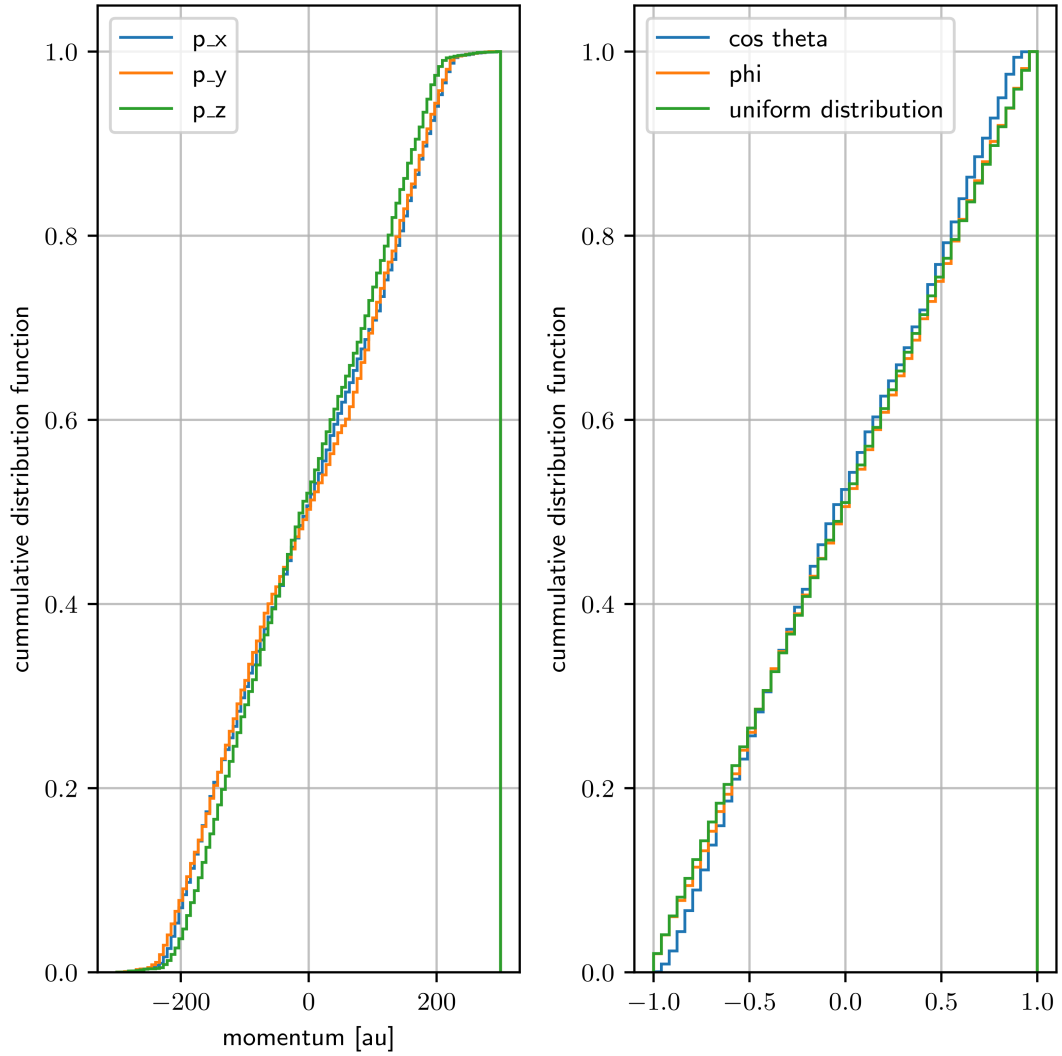
Figure A.4: Left: The comulative distribution of events is compared between the different momentum components. They should be equally distributed, so the score is chosen as the sum of absolute differences between the curves. Right: The azimuthal angle distribution and the cosine of the polar angle should be distributed uniformly, so we score the absolute distance to the uniform distribution.
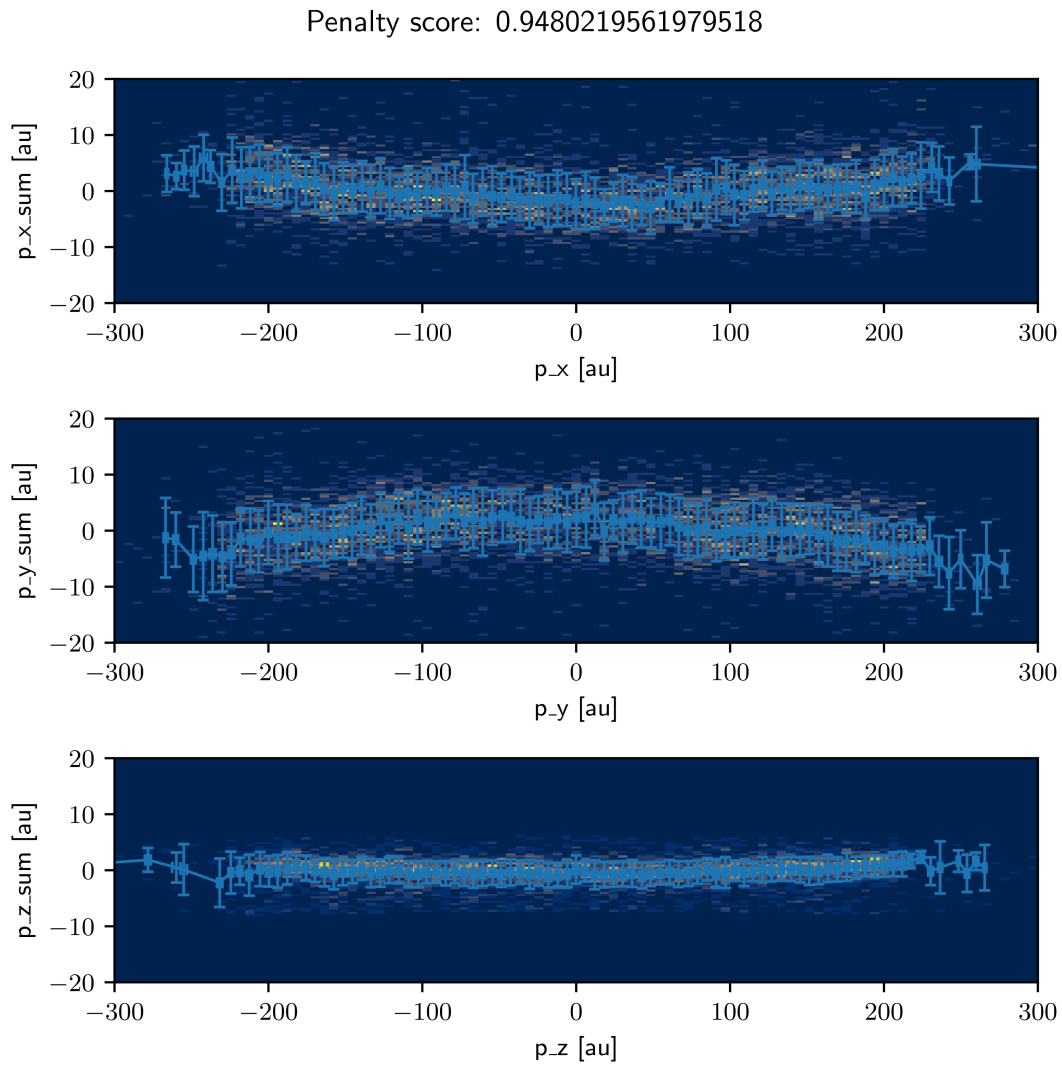
Figure A.5: The momentum sum for coincident events should not vary with the momentum magnitude along the same component. We score here the variation of the average values of the different bins.
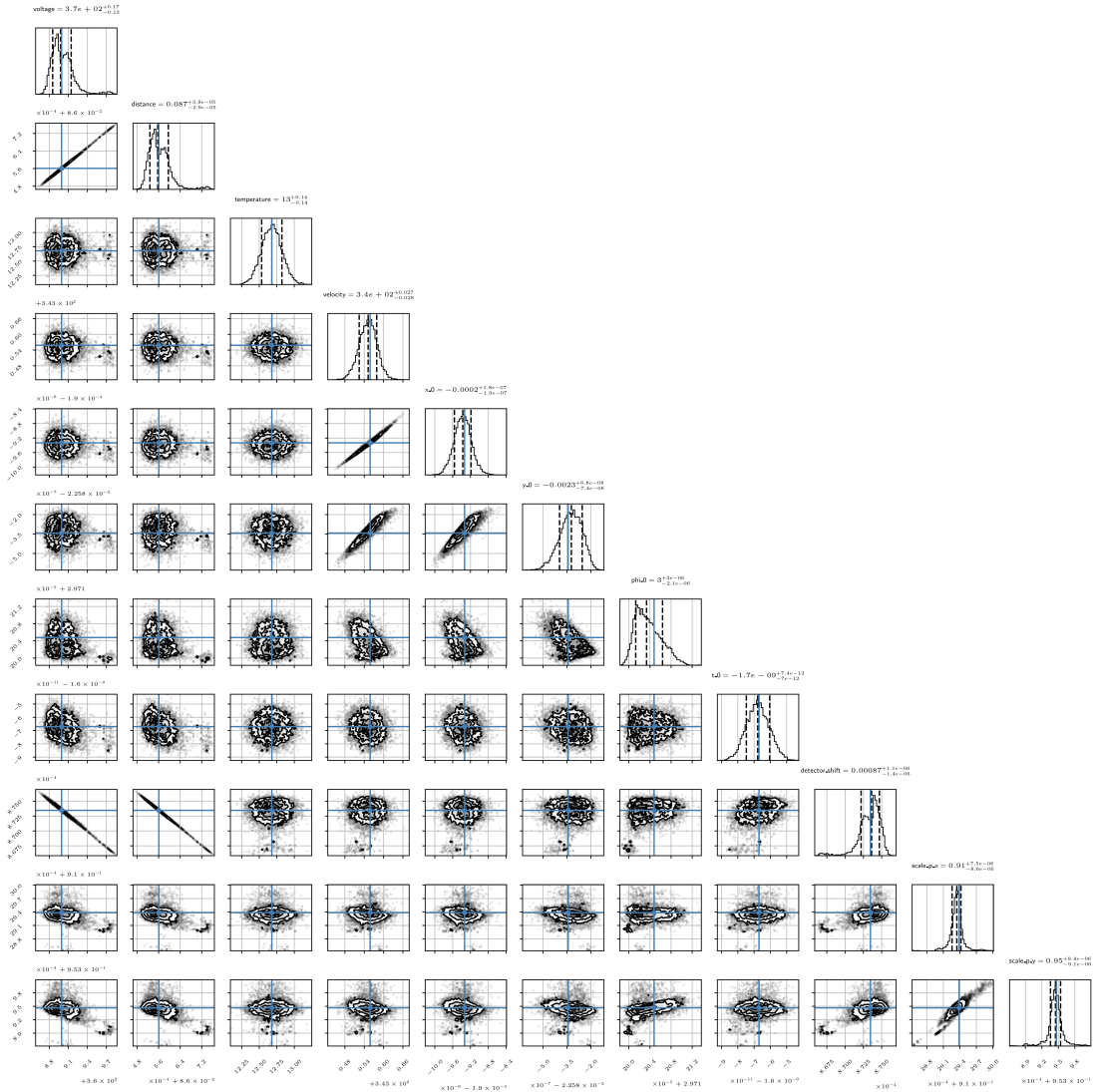
Figure A.6: This figure shows the full pairwise correlation matrix in the posterior distribution. The columns and rows are from top/left to bottom/right: Voltage U, distance d, target temperature T, jet velocity v_{jet}, the detector offset variables x_0, y_0, φ_0, t_0, the homogeneity detector shift correction δ and the position scaling parameters s_x and s_y. Several variables are strongly connected to each other, others are independent. However, all of them end up with narrow distributions. The Figure is zoomable in the electronic version.

Appendix B

Bibliography

B.1   References for Chapter 1 – Introduction

[1]   John Clark Sutherland. „Synchrotron Radiation Probes of Biological Structure and Dynamics". In: *BioScience* 31.8 (Sept. 1981), pp. 587–592. DOI: 10.2307/1308221 (cit. on p. 1).

[2]   C. T. Prewitt, P. Coppens, J. C. Phillips and L. W. Finger. „New Opportunities in Synchrotron X-ray Crystallography". In: *Science* 238.4825 (Oct. 1987), pp. 312–319. DOI: 10.1126/science.238.4825.312 (cit. on p. 1).

[3]   Marc Adrian, Jacques Dubochet, Jean Lepault and Alasdair W. McDowall. „Cryo-electron microscopy of viruses". In: *Nature* 308.5954 (Mar. 1984), pp. 32–36. DOI: 10.1038/308032a0 (cit. on p. 1).

[4]   Xing Zhang et al. „Near-atomic resolution using electron cryomicroscopy and single-particle reconstruction". In: *Proceedings of the National Academy of Sciences* 105.6 (Feb. 2008), pp. 1867–1872. DOI: 10.1073/pnas.0711623105 (cit. on p. 1).

[5]   C. Bostedt et al. „Ultrafast X-Ray Scattering of Xenon Nanoparticles: Imaging Transient States of Matter". In: *Physical Review Letters* 108.9 (Feb. 2012), p. 093401. DOI: 10.1103/PhysRevLett.108.093401 (cit. on p. 1).

[6]   Ingo Barke et al. „The 3D-architecture of individual free silver nanoparticles captured by X-ray scattering". In: *Nature Communications* 6.1 (Feb. 2015), p. 6187. DOI: 10.1038/ncomms7187 (cit. on p. 1).

[7]   Tomas Ekeberg et al. „Three-Dimensional Reconstruction of the Giant Mimivirus Particle with an X-Ray Free-Electron Laser". In: *Physical Review Letters* 114.9 (Mar. 2015), p. 098102. DOI: 10.1103/PhysRevLett.114.098102 (cit. on p. 1).

[8]   Henry N. Chapman, Carl Caleman and Nicusor Timneanu. „Diffraction before destruction". In: *Philosophical Transactions of the Royal Society B: Biological Sciences* 369.1647 (July 2014), p. 20130313. DOI: `10.1098/rstb.2013.0313` (cit. on p. 2).

[9]   Lise Meitner. „Über Die β-Strahl-Spektra und ihren Zusammenhang mit der γ-Strahlung". In: *Zeitschrift für Physik* 11.1 (Dec. 1922), pp. 35–54. DOI: `10.1007/BF01328399` (cit. on p. 2).

[10]   Pierre Auger. „Sur l'effet photoélectrique composé". In: *Journal de Physique et le Radium* 6.6 (1925), pp. 205–208. DOI: `10.1051/jphysrad:0192500606020500` (cit. on p. 2).

[11]   L. S. Cederbaum, J. Zobeley and F. Tarantelli. „Giant Intermolecular Decay and Fragmentation of Clusters". In: *Physical Review Letters* 79.24 (Dec. 1997), pp. 4778–4781. DOI: `10.1103/PhysRevLett.79.4778` (cit. on p. 2).

[12]   Lorenz S. Cederbaum. „Fragmentation of Molecules by Virtual Photons from Remote Neighbors". In: *Journal of Physical Chemistry Letters* 11.21 (Nov. 2020), pp. 8964–8969. DOI: `10.1021/acs.jpclett.0c02259` (cit. on p. 2).

[13]   Rainer Johnsen and Manfred A. Biondi. „Measurements of radiative charge-transfer reactions of doubly and singly charged rare-gas ions with rare-gas atoms at thermal energies". In: *Physical Review A* 18.3 (Sept. 1978), pp. 996–1003. DOI: `10.1103/PhysRevA.18.996` (cit. on p. 2).

[14]   K. Kreidi et al. „Relaxation processes following 1s photoionization and Auger decay in Ne2". In: *Physical Review A* 78.4 (Oct. 2008), p. 043422. DOI: `10.1103/PhysRevA.78.043422` (cit. on p. 2).

[15]   J Ullrich et al. „Recoil-ion and electron momentum spectroscopy: reaction-microscopes". In: *Reports on Progress in Physics* 66.9 (Sept. 2003), pp. 1463–1545. DOI: `10.1088/0034-4885/66/9/203` (cit. on pp. 2, 19).

[16]   Ch. Ellert et al. „Observing molecular dynamics with timed Coulomb explosion imaging". In: *Philosophical Transactions of the Royal Society of London. Series A: Mathematical, Physical and Engineering Sciences* 356.1736 (Feb. 1998). Ed. by J. P. Simons, pp. 329–344. DOI: `10.1098/rsta.1998.0168` (cit. on pp. 2, 24).

[17]   Liping Liu, Přemysl Kolorenč and Kirill Gokhberg. „Efficiency of core-level interatomic Coulombic decay in rare-gas dimers". In: *Physical Review A* 101.3 (Mar. 2020), p. 033402. DOI: `10.1103/PhysRevA.101.033402` (cit. on pp. 2, 15–17, 62, 119).

B.2   References for Chapter 2 – Electronic Decay and Transfer Processes in small Clusters

[17]   Liping Liu, Přemysl Kolorenč and Kirill Gokhberg. „Efficiency of core-level interatomic Coulombic decay in rare-gas dimers". In: *Physical Review A* 101.3 (Mar. 2020), p. 033402. DOI: 10.1103/PhysRevA.101.033402 (cit. on pp. 2, 15–17, 62, 119).

[18]   Till Jahnke et al. *Interatomic and intermolecular coulombic decay.* Oct. 2020. DOI: 10.1021/acs.chemrev.0c00106 (cit. on pp. 4, 5).

[19]   T. Havermeier et al. „Single Photon Double Ionization of the Helium Dimer". In: *Physical Review Letters* 104.15 (Apr. 2010), p. 153401. DOI: 10.1103/PhysRevLett.104.153401 (cit. on p. 12).

[20]   Deepthy Mootheril Thomas. „Electron impact ionization studies from atoms to complex molecules and clusters". PhD thesis. Heidelberg: Ruperto-Carola-University of Heidelberg, 2023. DOI: 10.11588/heidok.00033445 (cit. on p. 14).

[21]   A. Kramida, Yu. Ralchenko, J. Reader and NIST ASD Team. *NIST Atomic Spectra Database (ver. 5.10).* 2022. DOI: 10.18434/T4W30F. URL: https://physics.nist.gov/asd (cit. on p. 15).

B.3   References for Chapter 3 – Methods

[15]   J Ullrich et al. „Recoil-ion and electron momentum spectroscopy: reaction-microscopes". In: *Reports on Progress in Physics* 66.9 (Sept. 2003), pp. 1463–1545. DOI: 10.1088/0034-4885/66/9/203 (cit. on pp. 2, 19).

[16]   Ch. Ellert et al. „Observing molecular dynamics with timed Coulomb explosion imaging". In: *Philosophical Transactions of the Royal Society of London. Series A: Mathematical, Physical and Engineering Sciences* 356.1736 (Feb. 1998). Ed. by J. P. Simons, pp. 329–344. DOI: 10.1098/rsta.1998.0168 (cit. on pp. 2, 24).

[17]   Liping Liu, Přemysl Kolorenč and Kirill Gokhberg. „Efficiency of core-level interatomic Coulombic decay in rare-gas dimers". In: *Physical Review A* 101.3 (Mar. 2020), p. 033402. DOI: 10.1103/PhysRevA.101.033402 (cit. on pp. 2, 15–17, 62, 119).

[22]   Georg Schmid. „Two-Color Pump-Probe Experiments on Small Quantum Systems at the Free-Electron Laser in Hamburg". PhD thesis. Ruperto-Carola-University of Heidelberg, 2018. DOI: 10.11588/heidok.00024786 (cit. on pp. 20, 21, 27, 28, 34, 70–76, 78, 79, 105).

[23] Horst Schmidt-Böcking, Joachim Ullrich, Reinhard Dörner and Charles Lewis Cocke. „The COLTRIMS Reaction Microscope—The Spyhole into the Ultrafast Entangled Dynamics of Atomic and Molecular Systems". In: *Annalen der Physik* 533.9 (Sept. 2021), p. 2100134. DOI: 10.1002/andp.202100134 (cit. on p. 19).

[24] Florian Trost. „Time-resolved Fragmentation of Diiodomethane studied in an XUV Pump-Probe Experiment". PhD thesis. Ruperto-Carola-University of Heidelberg, 2023. DOI: 10.11588/heidok.00033303 (cit. on pp. 23, 29, 51).

[25] E. P. Kanter et al. „Role of excited electronic states in the interactions of fast (MeV) molecular ions with solids and gases". In: *Physical Review A* 20.3 (Sept. 1979), pp. 834–854. DOI: 10.1103/PhysRevA.20.834 (cit. on p. 24).

[26] U. Werner, K. Beckord, J. Becker, H.O. Folkerts and H.O. Lutz. „Ion-impact-induced fragmentation of water molecules". In: *Nuclear Instruments and Methods in Physics Research Section B: Beam Interactions with Materials and Atoms* 98.1-4 (May 1995), pp. 385–388. DOI: 10.1016/0168-583X(95)00152-2 (cit. on p. 24).

[27] Itamar Luzon, Ester Livshits, Krishnendu Gope, Roi Baer and Daniel Strasser. „Making Sense of Coulomb Explosion Imaging". In: *The Journal of Physical Chemistry Letters* 10.6 (Mar. 2019), pp. 1361–1367. DOI: 10.1021/acs.jpclett.9b00576 (cit. on p. 24).

[28] Kirsten Schnorr. „XUV Pump-Probe Experiments on Electron Rearrangement and Interatomic Coulombic Decay in Diatomic Molecules". PhD thesis. Ruperto-Carola-University of Heidelberg, 2014. DOI: 10.11588/heidok.00016294 (cit. on pp. 24–26, 28, 63, 75, 78).

[29] E. A. Gislason. „Series expansions for Franck-Condon factors. I. Linear potential and the reflection approximation". In: *The Journal of Chemical Physics* 58.9 (May 1973), pp. 3702–3707. DOI: 10.1063/1.1679721 (cit. on p. 25).

[30] Arne Senftleben. „Kinematically complete study on electron impact ionisation of aligned hydrogen molecules". PhD thesis. Ruperto-Carola-University of Heidelberg, 2009. DOI: 10.11588/heidok.00010015 (cit. on p. 28).

[31] J Adamczewski-Musch et al. *Go4: GSI Object Oriented On-line Off-line system.* Jan. 2017. URL: http://go4.gsi.de (cit. on p. 28).

[32] Rene Brun and Fons Rademakers. „ROOT — An object oriented data analysis framework". In: *Nuclear Instruments and Methods in Physics Research Section A: Accelerators, Spectrometers, Detectors and Associated Equipment* 389.1-2 (Apr. 1997), pp. 81–86. DOI: 10.1016/S0168-9002(97)00048-X (cit. on p. 28).

[33] Ruslan Kuprieiev et al. „DVC: Data Version Control - Git for Data & Models“. In: (Sept. 2023). DOI: 10.5281/ZENODO.8325439 (cit. on p. 28).

[34] Pauli Virtanen et al. „SciPy 1.0: fundamental algorithms for scientific computing in Python“. In: *Nature Methods* 17.3 (Mar. 2020), pp. 261–272. DOI: 10.1038/s41592-019-0686-2 (cit. on p. 28).

[35] John D. Hunter. „Matplotlib: A 2D Graphics Environment“. In: *Computing in Science & Engineering* 9.3 (2007), pp. 90–95. DOI: 10.1109/MCSE.2007.55 (cit. on p. 28).

[36] Charles R. Harris et al. „Array programming with NumPy“. In: *Nature* 585.7825 (Sept. 2020), pp. 357–362. DOI: 10.1038/s41586-020-2649-2 (cit. on p. 28).

[37] The pandas development team. *pandas-dev/pandas: Pandas.* June 2023. DOI: 10.5281/ZENODO.8092754 (cit. on p. 28).

[38] Stephan Hoyer and Joe Hamman. „xarray: N-D labeled Arrays and Datasets in Python“. In: *Journal of Open Research Software* 5.1 (Apr. 2017), p. 10. DOI: 10.5334/jors.148 (cit. on p. 28).

[39] Jim Pivarski et al. *Awkward Array.* Aug. 2023. DOI: 10.5281/ZENODO.8256267 (cit. on p. 28).

[40] Jim Pivarski et al. *Uproot.* Aug. 2023. DOI: 10.5281/ZENODO.8239801 (cit. on p. 28).

[41] Dask Development Team. *Dask: Library for dynamic task scheduling.* 2016. URL: https://dask.org (cit. on p. 28).

[42] Michael Waskom. „seaborn: statistical data visualization“. In: *Journal of Open Source Software* 6.60 (Apr. 2021), p. 3021. DOI: 10.21105/joss.03021 (cit. on p. 28).

[43] Elias Abboud. „Viviani's Theorem and Its Extension“. In: *The College Mathematics Journal* 41.3 (May 2010), pp. 203–211. DOI: 10.4169/074683410X488683 (cit. on p. 30).

[44] M Schulz, D Fischer, T Ferger, R Moshammer and J Ullrich. „Four-particle Dalitz plots to visualize atomic break-up processes“. In: *Journal of Physics B: Atomic, Molecular and Optical Physics* 40.15 (Aug. 2007), pp. 3091–3099. DOI: 10.1088/0953-4075/40/15/009 (cit. on p. 30).

[45] Ulrich Galster, Frank Baumgartner, Ulrich Müller, Hanspeter Helm and Martin Jungen. „Experimental and quantum-chemical studies on the three-particle fragmentation of neutral triatomic hydrogen“. In: *Physical Review A* 72.6 (Dec. 2005), p. 062506. DOI: 10.1103/PhysRevA.72.062506 (cit. on p. 31).

[46]   M. Fushitani et al. „Multielectron-Ion Coincidence Spectroscopy of Xe in Extreme Ultraviolet Laser Fields: Nonlinear Multiple Ionization via Double Core-Hole States". In: *Physical Review Letters* 124.19 (May 2020), p. 193201. DOI: 10.1103/PhysRevLett.124.193201 (cit. on p. 32).

[47]   J. E. Sansonetti and W. C. Martin. „Handbook of basic atomic spectroscopic data". In: *Journal of Physical and Chemical Reference Data* 34.4 (2005), pp. 1559–2259. DOI: 10.1063/1.1800011 (cit. on p. 42).

[48]   Daniel Foreman-Mackey, David W. Hogg, Dustin Lang and Jonathan Goodman. „emcee: The MCMC Hammer". In: *Publications of the Astronomical Society of the Pacific* 125.925 (Mar. 2013), pp. 306–312. DOI: 10.1086/670067 (cit. on p. 53).

[49]   Joe G Greener. „Differentiable simulation to develop molecular dynamics force fields for disordered proteins". In: *bioRxiv* (Aug. 2023). DOI: 10.1101/2023.08.29.555352 (cit. on p. 62).

[50]   Petr Slavìček et al. „State-of-the-art correlated *ab initio* potential energy curves for heavy rare gas dimers: Ar_2, Kr_2, and Xe_2". In: *The Journal of Chemical Physics* 119.4 (July 2003), pp. 2102–2119. DOI: 10.1063/1.1582838 (cit. on p. 62).

[51]   Jacqueline Fedyk. „On the theory of double ICD and applications of ICD". PhD thesis. Heidelberg: Ruperto-Carola-University of Heidelberg, 2023. DOI: 10.11588/heidok.00033377 (cit. on p. 68).

[52]   Meng Han et al. „Observation of Nuclear Wave-Packet Interference in Ultrafast Interatomic Energy Transfer". In: *Physical Review Letters* 130.25 (June 2023), p. 253202. DOI: 10.1103/PhysRevLett.130.253202 (cit. on p. 68).

B.4   References for Chapter 4 – The Reaction Microscope Beamline at FLASH2

[22]   Georg Schmid. „Two-Color Pump-Probe Experiments on Small Quantum Systems at the Free-Electron Laser in Hamburg". PhD thesis. Ruperto-Carola-University of Heidelberg, 2018. DOI: 10.11588/heidok.00024786 (cit. on pp. 20, 21, 27, 28, 34, 70–76, 78, 79, 105).

[28]   Kirsten Schnorr. „XUV Pump-Probe Experiments on Electron Rearrangement and Interatomic Coulombic Decay in Diatomic Molecules". PhD thesis. Ruperto-Carola-University of Heidelberg, 2014. DOI: 10.11588/heidok.00016294 (cit. on pp. 24–26, 28, 63, 75, 78).

[53]   Georg Schmid et al. „Reaction microscope endstation at FLASH2". In: *Journal of Synchrotron Radiation* 26.3 (May 2019), pp. 854–867. DOI: 10.1107/S1600577519002236 (cit. on pp. 69, 75, 78).

[54] Severin Meister et al. „Atomic, Molecular and Cluster Science with the Reaction Microscope Endstation at FLASH2". In: *Applied Sciences* 10.8 (Apr. 2020), p. 2953. DOI: `10.3390/app10082953` (cit. on p. 69).

[55] B. Faatz et al. „Simultaneous operation of two soft x-ray free-electron lasers driven by one linear accelerator". In: *New Journal of Physics* 18.6 (June 2016). DOI: `10.1088/1367-2630/18/6/062002` (cit. on p. 69).

[56] J. Rönsch-Schulenburg et al. „Experience with Multi-Beam and Multi-Beamline FEL-Operation". In: *Journal of Physics: Conference Series*. Vol. 874. 1. Institute of Physics Publishing, July 2017. DOI: `10.1088/1742-6596/874/1/012023` (cit. on pp. 69, 70).

[57] J.J. Yeh and I. Lindau. „Atomic subshell photoionization cross sections and asymmetry parameters: $1 \leq Z \leq 103$". In: *Atomic Data and Nuclear Data Tables* 32.1 (Jan. 1985), pp. 1–155. DOI: `10.1016/0092-640X(85)90016-6` (cit. on p. 76).

[58] Eldon L. Knuth. „Dimer-formation rate coefficients from measurements of terminal dimer concentrations in free-jet expansions". In: *The Journal of Chemical Physics* 66.8 (Apr. 1977), pp. 3515–3525. DOI: `10.1063/1.434438` (cit. on p. 77).

[59] D. R. Miller. „Free Jet Sources". In: *Atomic and Molecular Beam Methods*. Vol. 1. Oxford Univ. Press, 1988, pp. 14–53 (cit. on p. 78).

[60] P. M. Dehmer and J. L. Dehmer. „Photoelectron spectrum of Xe_2 and potential energy curves for Xe_2+". In: *The Journal of Chemical Physics* 68.8 (1977), pp. 3462–3470. DOI: `10.1063/1.436254` (cit. on p. 78).

[61] I.S Gilmore and M.P Seah. „Ion detection efficiency in SIMS:" in: *International Journal of Mass Spectrometry* 202.1-3 (Oct. 2000), pp. 217–229. DOI: `10.1016/S1387-3806(00)00245-1` (cit. on p. 81).

B.5 References for Chapter 5 – Results

[22] Georg Schmid. „Two-Color Pump-Probe Experiments on Small Quantum Systems at the Free-Electron Laser in Hamburg". PhD thesis. Ruperto-Carola-University of Heidelberg, 2018. DOI: `10.11588/heidok.00024786` (cit. on pp. 20, 21, 27, 28, 34, 70–76, 78, 79, 105).

[62] E. C. M. Chen, J. G. Dojahn and W. E. Wentworth. „Characterization of Homonuclear Diatomic Ions by Semiempirical Morse Potential Energy Curves. 2. The Rare Gas Positive Ions". In: *The Journal of Physical Chemistry A* 101.17 (Apr. 1997), pp. 3088–3101. DOI: `10.1021/jp9638954` (cit. on p. 82).

[63] Robert Hellmann, Benjamin Jäger and Eckard Bich. „State-of-the-art ab initio potential energy curve for the xenon atom pair and related spectroscopic and thermophysical properties". In: *Journal of Chemical Physics* 147.3 (July 2017). DOI: `10.1063/1.4994267` (cit. on p. 82).

[64] L O Werme, T Bergmark and K Siegbahn. „The High Resolution L2,3 MM and M4,5 NN Auger Spectra from Krypton and M4,5 NN and N4,5 OO Auger Spectra from Xenon". In: *Physica Scripta* 6.2-3 (Aug. 1972), pp. 141–150. DOI: `10.1088/0031-8949/6/2-3/008` (cit. on p. 103).

[65] Thomas Pflüger. „Electron impact ionization studies of small rare gas clusters". PhD thesis. Ruperto-Carola-University of Heidelberg, 2012. DOI: `10.11588/heidok.00013325` (cit. on p. 103).

[66] Georg Schmid et al. „Tracing charge transfer in argon dimers by XUV-pump IR-probe experiments at FLASH". In: *The Journal of Chemical Physics* 151.8 (Aug. 2019), p. 084314. DOI: `10.1063/1.5116234` (cit. on p. 104).

[67] Mathias Arbeiter and Thomas Fennel. „Rare-gas clusters in intense VUV, XUV and soft x-ray pulses: signatures of the transition from nanoplasma-driven cluster expansion to Coulomb explosion in ion and electron spectra". In: *New Journal of Physics* 13.5 (May 2011), p. 053022. DOI: `10.1088/1367-2630/13/5/053022` (cit. on p. 104).

B.6 References for Chapter 6 – Summary

[17] Liping Liu, Přemysl Kolorenč and Kirill Gokhberg. „Efficiency of core-level interatomic Coulombic decay in rare-gas dimers". In: *Physical Review A* 101.3 (Mar. 2020), p. 033402. DOI: `10.1103/PhysRevA.101.033402` (cit. on pp. 2, 15–17, 62, 119).

B.7 Coauthored Journal Publications

[53] Georg Schmid et al. „Reaction microscope endstation at FLASH2". In: *Journal of Synchrotron Radiation* 26.3 (May 2019), pp. 854–867. DOI: 10.1107/S1600577519002236 (cit. on pp. 69, 75, 78).

[54] Severin Meister et al. „Atomic, Molecular and Cluster Science with the Reaction Microscope Endstation at FLASH2". In: *Applied Sciences* 10.8 (Apr. 2020), p. 2953. DOI: 10.3390/app10082953 (cit. on p. 69).

[68] D Fischer et al. „Ion-Lithium Collision Dynamics Studied with a Laser-Cooled In-Ring Target". In: *Phys. Rev. Lett.* 109.11 (Sept. 2012), p. 113202. DOI: 10.1103/PhysRevLett.109.113202.

[69] M D Śpiewanowski et al. „Target electron ionization in $Li^{2+}-Li$ collisions: A multi-electron perspective". In: *Journal of Physics: Conference Series* 601.1 (Apr. 2015), p. 012010. DOI: 10.1088/1742-6596/601/1/012010.

[70] R. Hubele et al. „Electron and recoil ion momentum imaging with a magneto-optically trapped target". In: *Review of Scientific Instruments* 86.3 (Mar. 2015). DOI: 10.1063/1.4914040.

[71] S. Augustin et al. „Signatures of autoionization in the angular electron distribution in two-photon double ionization of Ar". In: *Physical Review A* 98.3 (Sept. 2018), p. 033408. DOI: 10.1103/PhysRevA.98.033408.

[72] Georg Schmid et al. „Terahertz-Field-Induced Time Shifts in Atomic Photoemission". In: *Physical Review Letters* 122.7 (Feb. 2019), p. 073001. DOI: 10.1103/PhysRevLett.122.073001.

[73] Georg Schmid et al. „Tracing charge transfer in argon dimers by XUV-pump IR-probe experiments at FLASH". In: *The Journal of Chemical Physics* 151.8 (Aug. 2019). DOI: 10.1063/1.5116234.

[74] Elisa Appi et al. „A synchronized VUV light source based on high-order harmonic generation at FLASH". In: *Scientific Reports* 10.1 (Apr. 2020), p. 6867. DOI: 10.1038/s41598-020-63019-2.

[75] Severin Meister et al. „Photoelectron spectroscopy of laser-dressed atomic helium". In: *Physical Review A* 102.6 (Dec. 2020), p. 062809. DOI: 10.1103/PhysRevA.102.062809.

[76] Severin Meister et al. „Linear dichroism in few-photon ionization of laser-dressed helium". In: *The European Physical Journal D* 75.7 (July 2021), p. 205. DOI: 10.1140/epjd/s10053-021-00218-0.

[77] F. Schotsch et al. „TrapREMI: A reaction microscope inside an electrostatic ion beam trap". In: *Review of Scientific Instruments* 92.12 (Dec. 2021). DOI: 10.1063/5.0065454.

[78]   E. Appi et al. „Synchronized beamline at FLASH2 based on high-order harmonic generation for two-color dynamics studies". In: *Review of Scientific Instruments* 92.12 (Dec. 2021). DOI: 10.1063/5.0063225.

[79]   Michael Straub et al. „Differential Measurement of Electron Ejection after Two-Photon Two-Electron Excitation of Helium". In: *Physical Review Letters* 129.18 (Oct. 2022), p. 183204. DOI: 10.1103/PhysRevLett.129.183204.

[80]   Enliang Wang et al. „Ultrafast Roaming Mechanisms in Ethanol Probed by Intense Extreme Ultraviolet Free-Electron Laser Radiation: Electron Transfer versus Proton Transfer". In: *The Journal of Physical Chemistry Letters* 14.18 (May 2023), pp. 4372–4380. DOI: 10.1021/acs.jpclett.2c03764.

[81]   Kirsten Schnorr et al. „Direct tracking of ultrafast proton transfer in water dimers". In: *Science Advances* 9.28 (July 2023). DOI: 10.1126/sciadv.adg7864.

Appendix C

Acronyms

Auger-Meitner Decay (AMD) An autoionization process of electronically excited atoms. Discovered first by Lise Meitner and later independently by Piere Auger. 2, 4–7, 9, 12, 14, 15, 17, 82, 84, 89, 93, 96, 103, 104, 118, 119

Charge Transfer (CT) A process where an electron is transfered to another atom or ion. 3, 4, 7, 8, 14, 17, 62, 63, 65, 66, 68, 86–90, 94, 95, 98, 100, 101, 104, 108, 109, 112, 114–116, 118–120

collective Interatomic Coulombic Decay (cICD) 4, 9, 11, 17, 85, 93, 99, 103, 119, 120

Coulomb Explosion (CE) 7, 28, 46, 47, 104, 108, 114

Coulomb Explosion Imaging (CEI) 2, 19, 24–26

Delay Line Anode (DLA) Wire grid for detection of the position, where a charge cloud impinges. 19

double Interatomic Coulombic Decay (dICD) 4, 9, 10, 17, 119

exchange Interatomic Coulombic Decay (exICD) 9, 11, 12

FLASH2 reaction microscope (FlashRemi) Reaction microscope beamline at FLASH2. 2, 3, 70, 71, 74, 78, 118, 120, *see also* FLASH2 & REMI

Free Electron Laser (FEL) Light source based on coherent emission of synchrotron radiation from electrons. 1, 2, 18, 20, 21, 26, 27, 29, 34, 35, 39, 51, 56, 60, 70–72, 74, 75, 77, 87, 99

Free electron LASer in Hamburg (FLASH) An FEL in Hamburg based on a super conducting radio frequency cavity linear accelerator. 28, *see* FEL

Free electron LASer in Hamburg 1 (FLASH1) First FEL beamline in Hamburg, originally called FLASH. 69–71, *see* FEL & FLASH

Free electron LASer in Hamburg 2 (FLASH2) Second FEL beamline in Hamburg, uses same accelerator as in FLASH1. 69–71, 118, *see* FEL & FLASH

Frustrated Ionisation (FI) 85, 104, 105, 118

Full Width at Half Maximum (FWHM) 71

Förster Resonant Energy Transfer (FRET) 4, 8, 9

Grand unifiEd reactioN microscopE souRce Code (GENERiC) 28

GSI Object Oriented On-line Off-line system (Go4) 28

Interatomic Coulombic Decay (ICD) 2, 4, 9, 10, 14, 15, 63, 104, 109, 119

Kinetic Energy Release (KER) The total amount of energy from a reaction that is released to the kinetic energy of ionic fragments. 24–26, 29, 45, 59, 68, 80, 89–95, 97–101, 105–112, 114, 116, 119, 125

Knock Off ionisation (KO) 4, 12–14, 103, 119, 120

Leave One Out Cross Validation (LOOCV) 36

Lennard-Jones (LJ) 62, 63, 68

Markov Chain Monte Carlo (MCMC) 51

Micro Channel Plate (MCP) Semiconductor plate with a regular grid of charge multiplier tubes. 19, 23, 51, 60, 80, 81

Molecular Dynamics simulation (MD) 2, 40, 63

Open Area Ratio (OAR) The area ration between open channels and total geometric area of a MCP 80, *see* MCP

Over The Barrier Model (OTBM) 63

Radiative Charge Transfer (RCT) A process where an electron is transfered to another atom or ion while emitting a photon. 2, 4, 7–9, 17, 119

Radiative Decay (RD) 4–9, 104

REeaction MIcroscope (REMI) Measurement devcie for the vector momentum of charged reaction products. 2, 3, 18–20, 28, 32, 42, 62, 69–71, 74, 78, 81, 118

ROOT data analysis framework (ROOT) 28

Sequential Ionisation (SI) 14, 103

Shake Up photoionization (SU) An atom or molecule is ionised and additionally excited electronically by a single photon. 84

Supersonic Gas Jet (SGJ) A fast jet of cold gas. It is generated by adiabatic expansion of pressurized gas through a thin nozzle into a volume of very low pressure. 2, 18, 20, 21, 23, 44, 56, 59, 72, 75, 76, 78

three particle Electron Transfer Mediated Decay (ETMD(3)) A process where an electron is transfered to another atom or ion and at the same time ionizes a third atom. 3, 4, 13, 62, 63, 65, 66, 68, 85–87, 108–112, 114–116, 119

Time Of Flight (TOF) The amount of time that a fragment travels between a initial reaction and it's detection. 19, 21–23, 40, 42–47, 50, 51, 53–60, 70, 77, 78, 80, 81, 83

two particle Electron Transfer Mediated Decay (ETMD(2)) A process where an electron is transfered to another atom or ion and at the same time further ionises either atom. 4, 12, 17, 85, 103, 119